ISSN: 2227-6912
E-ISSN: 2790-0479

Azerbaijan Technical University

MACHINE SCIENCE

2
2023

International scientific-technical journal

MACHINE SCIENCE

MAŞINŞÜNASLIQ МАШИНОВЕДЕНИЕ

International scientific-technical journal
Beynəlxalq elmi-texniki jurnal
Международный научно-технический журнал

Number 2
2023

Founder: *Minister of Science and Education Republic of Azerbaijan*
Təsisçi: *Azərbaycan Respublikası Elm və Təhsil Nazirliyi*
Учредитель: *Министерство Науки и Образования Азербайджанской Республики*

The journal is included into the list confirmed by Higher Attestation Commission of the Azerbaijan Republic of editions for the publication of works of competitors for scientific degrees

Jurnal Azərbaycan Respublikası Ali Atestasiya Komissiyasının təsdiq etdiyi elmi dərəcə iddiaçılarının əsərlərinin çap edildiyi dövri elmi nəşrlərin siyahısına daxil edilmişdir.

Журнал входит в перечень, утвержденных ВАК Азербайджанской Республики, изданий для публикации трудов соискателей ученых степеней

Journal was founded according the order No1861 Ministry of Education of Azerbaijan Republic on the date 25.11.2011. Registration No 3521. Journal is published at least twice a year.

Jurnal Azərbaycan Respublikası Təhsil Nazirliyinin 25.11.2011-ci il tarixli 1861 saylı əmri əsasında təsis edilmişdir. Qeydiyyat No 3521. İldə ən azı iki nömrə nəşr edilir.

Учреждено приказом за №1861 от 25.11.2011 года Министерства образования Азербайджанской Республики. Регистрация № 3521. Ежегодно публикуется два номера.

It has been published since 2001. Published in 2001 - 2011 with a name "Mechanics-machine building"
2001-ci ildən nəşr edilir. 2001 – 2011-ci illərdə "Mexanika-maşınqayırma" adı ilə çap edilmişdir.
Издается с 2001 года. В 2001 – 2011 годах издано под названием «Механика-машиностроение»

The "MACHINE SCIENCE" journal is supported by Azerbaijan Technical University, which means there are no publication fees for authors.
"MAŞINŞÜNASLIQ" jurnalı Azərbaycan Texniki universiteti tərəfindən dəstəklənir və məqalələrin nəşri üçün müəlliflərdən hər hansı ödəniş tələb olunmur.
Журнал «МАШИНОВЕДЕНИЕ» поддерживается Азербайджанским Техническим Университетом, что означает, что с авторов не взимается плата за публикацию статей.

Editorial address: ***Redaksiyanın ünvanı:*** ***Адрес редакции:***	Baku, AZ1073, H.Javid ave., 25. AzTU Tel: (+994 12) 539 12 25 E-mail: msj@aztu.edu.az	© Machine Science, 2023 **ISSN:** 2227-6912 **E-ISSN:** 2790-0479

EDITORIAL COMMITTEE

Member of Editorial Board, prof. Rasim Alizade awarded by IFToMM General Assembly

The consultant professor at the Department "Machine design and industrial technologies" Rasim Alizade awarded in 16th World Congress of the International Federation for the Promotion of Mechanism and Machine Science, heled in Tokyo on November 8, 2023.

He awarded by IFToMM General Assembly in recognition of his substantial voluntary services, outstanding performance, and effective leadership for the good of whole Federation.

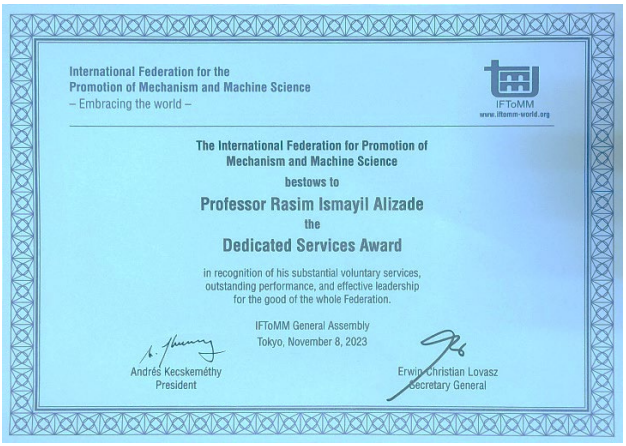

Rasim Ismayil Alizade is the Chairman of the Azerbaijan Committee of the International Federation for the development of science "Theory of Mechanisms and Machines" (AzC IFToMM at the Azerbaijan Technical University was approved by the IFToMM Assembly in 1995) and also member of Technical Committee for Linkages and Mechanical Controls of IFToMM. Prof. Alizade R. participated in the proceedings ща World Congresses "Theory of Mechanisms and Machines" (IFToMM), as well as in the proceedings of International Symposiums "Science of Mechanisms and Machines" (AzC IFToMM - 2010, 2013, 2017 - Azerbaijan-Turkey). "Four new Euclidean 6 Degree of Freedom parallel docking manipulators of spacecraft" and 2 new models "wheeled robot-rovers for Mars and Moon surfaces" designed by prof. Alizade R. have very great important in cosmic industry.

On behalf of the editorial board and the entire team of the international scientific and technical journal Machine Science, we congratulate Prof. Rasim Alizadeh, we wish him good health and success in his scientific activities!

MACHINE SCIENCE

ISSN: 2227-6912
E-ISSN: 2790-0479

2023, № 2 Pages 5 – 19

THE EFFECTS OF PARTICLE SIZE AND TEMPERATURE ON THE STABILITY AND LOCAL STRUCTURAL EVOLUTIONS OF AMORPHOUS BULK AND NANOPARTICLES OF THE $FeNI_3$ ALLOYS

Amdulla MEKHRABOV[1,2,a*], Ece A. IRMAK[3,b], M. Vedat AKDENİZ[3,c]

[1]Novel Materials and Nanotechnologies Institute, Azerbaijan Technical University, Baku, Azerbaijan
[2]Faculty of Metallurgy and Materials Science, Department of Metallurgy and Materials Technologies, Azerbaijan Technical University, Baku, Azerbaijan
[3]Novel Alloy Design and Development Laboratory (NOVALAB), Department of Metallurgical and Materials Engineering, Middle East Technical University, Ankara, Türkiye

E-mail: *[a]*emdulla.mehrabov@aztu.edu.az*

http://dx.doi.org/10.61413/CEAD8914

Abstract: The effects of particle size (2-6 nm) and temperature (300-1900 K) on the stability and local structural evolutions of amorphous bulk and nanoparticles of the $FeNi_3$ alloys have been studied by using classical molecular dynamics (MD) simulation method combined with embedded atom model (EAM) in Large-scale Atomic/Molecular Massively Parallel Simulator (LAMMPS). The nanoparticles were obtained from the unstable amorphous bulk $FeNi_3$ alloys. MD simulations have been performed for glassy $FeNi_3$ intermetallic alloy by making use of pairwise interatomic interaction potentials and electron densities calculated via EAM method. The formation and evolution of structures and their stability have been analyzed at a wide temperature range (300-1900 K) by calculating radial distribution functions (RDF), interatomic distances (ID), coordination numbers (CN), core-to-surface concentration profiles, as well as Voronoi analysis. According to the results, although some deviations in the structural properties occurred during the heat treatment, the amorphous nanoparticles exhibited the same crystal structure and local atomic configuration with its bulk counterpart at room temperature.

Keywords: *Fe-Ni, Amorphous, Bulk and Nanoparticles, Modelling and Simulations, Molecular dynamics, Embedded atom model*

Introduction.

There is a growing research interest on the modeling and simulation of the magnetic nanoalloys, since the unique and sometimes superior chemical and physical properties of the nanoalloys can be tuned and, consequently, new structural motifs can be created by varying the type of constituent elements, atomic and magnetic ordering, as well as size and shape of the nanoparticles for several promising research and application area [1]. For new generation magnetic nanoalloys, it is important to predict structure-property relations in advance because of the complexity increased by the various structural and geometrical forms in addition to the size-dependent structure [2, 3]. Among the magnetic nanoalloys, Fe-Ni based magnetic nanoalloys have promising usage area in the diversified engineering applications, such as radar absorbing materials in aerospace and stealth industry, catalyst, and biomedical applications, due to their superior mechanical, electrical, optical and magnetic properties with high surface area [4-9]. However, there is not enough study regarding these usage areas of the Fe-Ni nanoalloys because of the concern of the agglomeration, oxidation, and degradation; therefore, it is essential to predict and determine the thermally stable size and shape of the nanoparticles [9]. Computer simulation techniques have been widely used to investigate structural properties of the Fe-Ni based bulk and nanostructured alloys for a long time. Atomic and magnetic

ordering, order-disorder and ferromagnetic-paramagnetic transformation characteristics and also interrelation between atomic and magnetic ordering phenomena in binary $FeNi_3$ and ternary Ni_3(Fe, Me) (Me= W, Mo, Cr, Mn, Nb, etc.) bulk intermetallics have been widely investigated in terms of classical theory of ordering and electronic theory of binary and multicomponent alloys in ab-initio pseudopotential approximation [10-16]. Although the first principle calculations on the Fe-Ni based alloys have been used to predict the properties from atomistic level [17, 18], the molecular dynamics simulations with many-body potentials are mainly preferred because of its applicability to the large systems having more than hundreds of atoms. However, to acquire accurate and efficient results from the molecular dynamics simulations, inter-atomic potential energy functions have a crucial effect [19].

Therefore, in this study, stability and local structural evolutions in amorphous intermetallic $FeNi_3$ nanoparticles with 2-6 nm particle size have been modeled and simulated for wide temperature range (from room temperature up to 1900 K) by means of EAM-MD simulation methods in Large-scale Atomic/Molecular Massively Parallel Simulator (LAMMPS).

Methodology

2.1. Pairwise interatomic interaction potentials calculations

EAM method is based on the density functional theory and it considers many-body interaction through the electron density of the systems. Therefore, EAM gives more accurate results than the pairwise interaction models with reasonable computational time for Fe-based systems [20-22]. According to EAM model [20], the energy of the system which consists of N-atoms can be expressed as,

$$E = \sum_i F_i(\rho_i) + \frac{1}{2}\sum_{ij} V_{ij}(r_{ij}) \tag{1}$$

where V_{ij} represents the pairwise interatomic interaction potentials between atoms i and j separated by distance of r_{ij} (in Eq. (1), i and j, regardless of the different type of atoms, represent any atoms), and F_i stands for the embedding energy to embed an atom i into a local site with electron density $\bar{\rho}_i$ and $\bar{\rho}_i$ can be calculated by using

$$\bar{\rho}_i = \sum_{i \neq j} \rho(r_{ij}) \tag{2}$$

with $\rho(r_{ij})$ being the electron density at the site of atom i arising from atom j at a distance r_{ij} away.

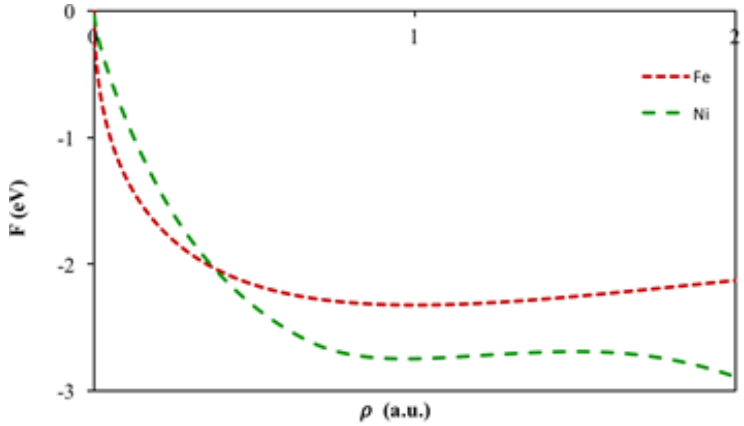

Figure 1. Embedding energy variation with electron density in $FeNi_3$ alloy

In this study, the EAM parameters that were determined in [20] have been used for calculations of the embedding energy variation with electron density and electron density dependence on interatomic separation distance in $FeNi_3$ alloy by means of LAMMPS program system, which are shown in Figs. 1 and 2, respectively.

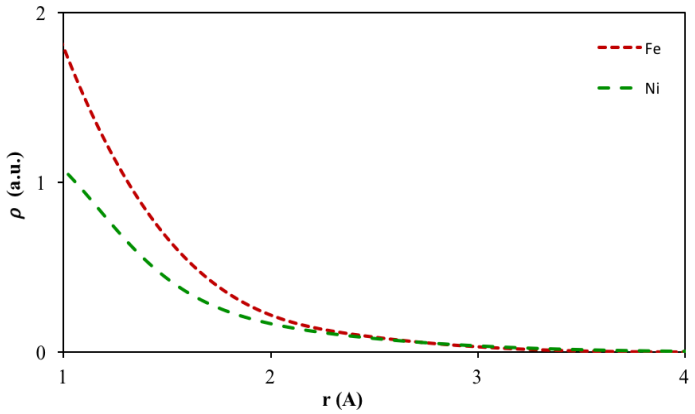

Figure. 2. Electron density dependence on interatomic separation distance in $FeNi_3$ alloy

Calculated pairwise interatomic interaction potentials variations with interatomic distance for Fe-Fe, Ni-Ni and Fe-Ni atomic pairs in FeNi alloy are presented in Fig. 3.

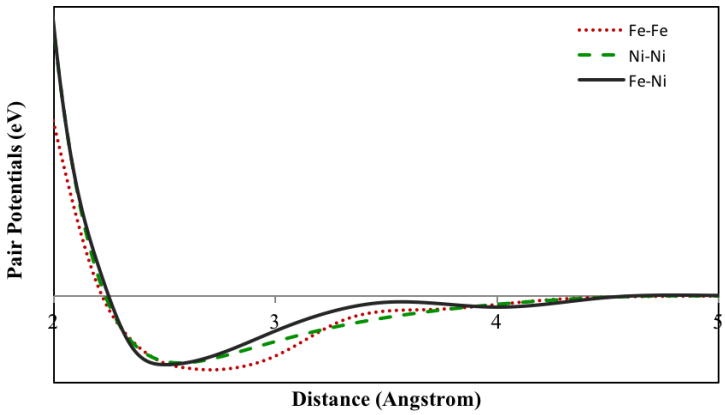

Figure 3. Pairwise interatomic interaction potentials variation with interatomic separation distance in $FeNi_3$ alloy

2.2. MD simulations of $FeNi_3$ nanoparticles

MD simulations have been performed by means of MedeA - LAMMPS molecular dynamics simulator program system, by using interatomic interaction potentials and electron densities calculated via EAM method. During solving the equation of motions of atoms in MD, Verlet algorithm was considered with Nose-Hoover thermostat and barostat. Among the ensembles typically used for molecular dynamics, namely the microcanonical (NVE), canonical (NVT) and isothermal–isobaric (NPT) ensembles, the NPT ensemble was applied in this study because it accurately describes experimental conditions by controlling temperature and pressure at the same time [23, 24].

$FeNi_3$ alloy is known to have a chemically ordered face-centered cubic (FCC) $L1_2$-type structure as shown in Fig 4.

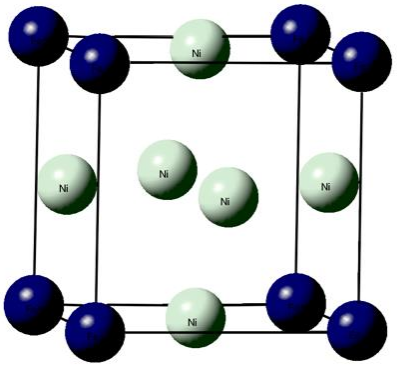

Figure 4. $AuCu_3$-type ordered ($L1_2$) FCC lattice of $FeNi_3$ alloys

The bulk form of $FeNi_3$ alloy, having 27436 atoms, was generated by repeating the $L1_2$ structured unit cell along [111] direction nineteen times. Firstly, the lattice parameter of $FeNi_3$ alloy was optimized and the alloy was relaxed at 0 K under the periodic boundary conditions. Then, the temperature was increased to 2600 K under 1 atm pressure directly with $5x10^5$ MD steps and the system waited for $5x10^4$ steps. 2600 K is higher than the melting temperature of alloy which was enough to homogenize the liquid structure. In order to obtain the amorphous bulk structure, the system was cooled down from 2600 K to 300 K by fast cooling ($2.3x10^{13}$ K/sec) and stabilized at room temperature. The time step was 1 fs and the motion of atoms was integrated by using Verlet algorithms. Non-periodic boundary condition was applied to simulate the amorphous bimetallic $FeNi_3$ NPs. Firstly, NPs was subtracted from the simulated amorphous bulk alloy, Fig. 5.

Then, the subtracted NPs was melted and equilibrated at 1900 K in order to remove local atomic configurations from the solid phase. Finally, the temperature of NPs was decreased to room temperature, gradually. To obtain accurate results from molecular dynamics simulations, the temperature of the amorphous NPs was decreased with the same cooling rate ($2x10^{12}$ K/sec) as bulk alloys and equilibrate the system at each stage by waiting for 10 nanoseconds. The simulations of the amorphous NPs were conducted for 2 nm, 4 nm and 6 nm diameters (the total number of atoms are 368, 2913 and 9784, respectively. The heat-treated amorphous $FeNi_3$ nanoparticles were illustrated by using VMD molecular graphics program.

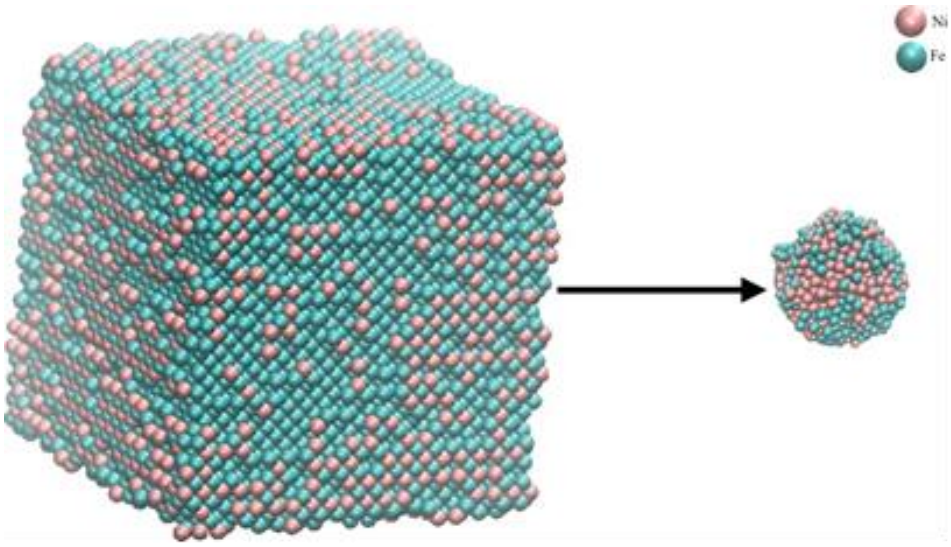

Figure 5. Extraction of NPs from bulk amorphous $FeNi_3$ alloy

Results and discussions

3.1. Radial distribution functions (RDF) for the bulk $FeNi_3$ alloy

Before the investigation of the structural evolution of the $FeNi_3$ bulk system, the lattice parameter was optimized. In this regard, crystal structures were generated with different lattice parameters (from 3 Å to 4 Å). Then, the systems were minimized by conjugate gradient method in MD, and the total energies of the crystal structures were calculated. Afterward, the crystal structure owing to the minimum total energy was obtained with the lattice parameter, a=3.46 Å. Then, the input file of the $FeNi_3$ bulk system was prepared according to the minimized lattice parameter, a=3.46 Å. The total energy change with respect to the various lattice parameters is shown in Figure 6.

To obtain the amorphous bulk structure, the system was cooled from 2600 K to 300 K by fast cooling with $2.3x10^{13}$ K/sec cooling rate. The volume changes during heating and fast cooling for the bulk $FeNi_3$ alloy is shown in Figure 7.

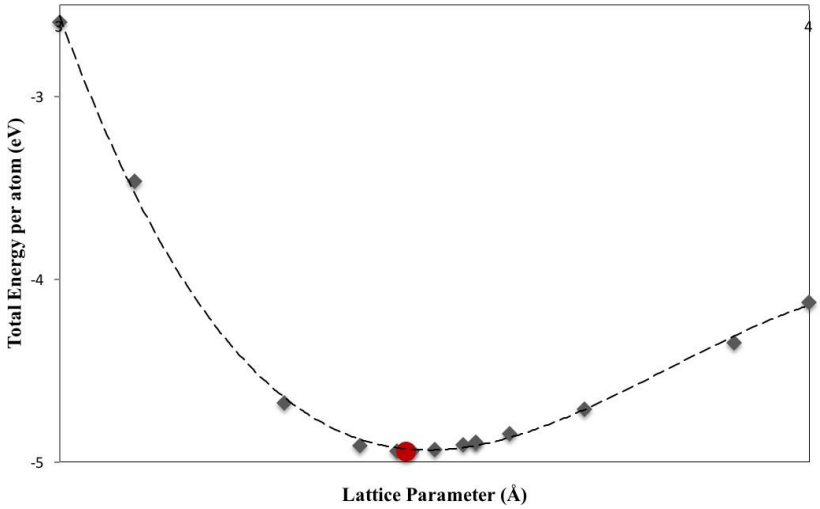

Figure 6. The total energy variation with lattice parameters of $FeNi_3$ alloy

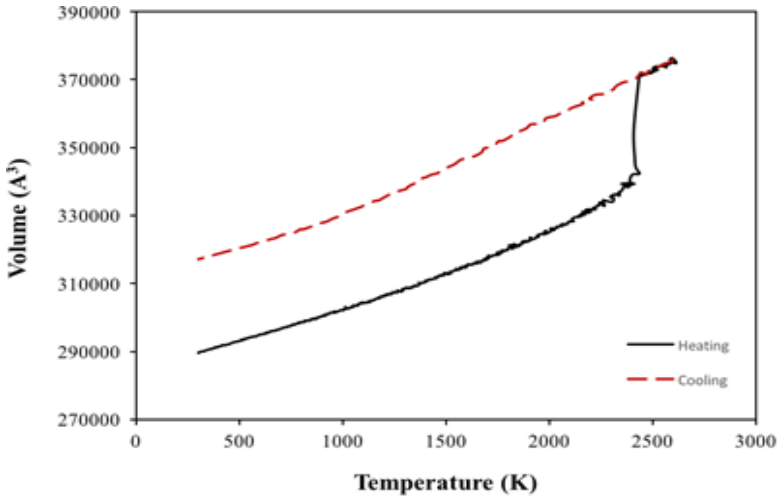

Figure 7. The volume change during heating and fast cooling processes of the $FeNi_3$ alloy

During the heating process, there was a sudden jump in the volume curve which is the sign of the melting. However, we did not observe any sudden change in the volume during fast cooling with $2.3x10^{13}$ K/sec rate, which indicated that no crystallization occurred and the amorphous structure was

preserved at room temperature. Also, this amorphous structure was proven by the RDFs which is illustrated in Figure 8.

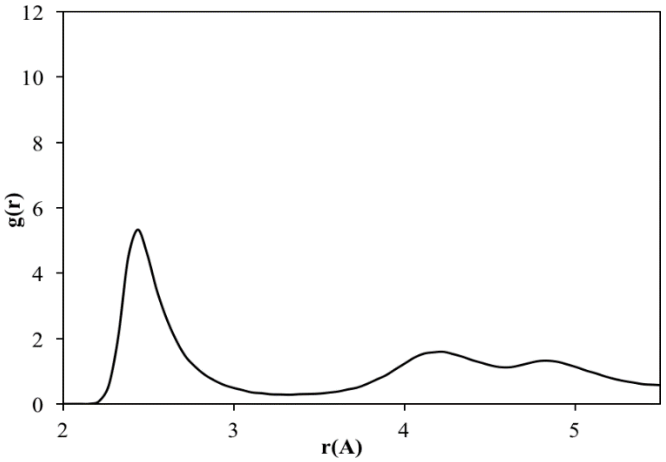

Figure 8. RDF of the $FeNi_3$ amorphous bulk alloy

The calculated partial coordination numbers and nearest-neighbor distances of the amorphous bulk $FeNi_3$ alloy are tabulated in Table 1. The total coordination number of the bulk amorphous $FeNi_3$ alloy obtained from the RDF was 13.2.

Table 1. The partial coordination numbers and nearest-neighbor distance of amorphous bulk $FeNi_3$ alloy

Amorphous bulk $FeNi_3$ alloy	N_{Fe-Fe}	N_{Fe-Ni}	N_{Ni-Ni}	d_{Fe-Fe}	d_{Fe-Ni}	d_{Ni-Ni}
(EAM-MD method)	4.3	9.0	10.2	2.5	2.4	2.4

3.2 RDF for the amorphous $FeNi_3$ NPs

RDF dependences on temperature for 2 nm, 4 nm and 6 nm amorphous nanoparticle are given in Figures 9 (a), (b) and (c), respectively. The nanoparticle with the diameter equal to 2 nm consists of 368 atoms in total, with 112 iron atoms and 256 nickel atoms. To determine the temperature effect on the structural evolution of the nanoparticles, the systems were cooled from 1900 K to 300 K by 200 K interval.

According to Figure 9 (a), we clearly observed that, at high temperatures, there was an absence of order between atoms, but the first peaks were always clear at high temperatures. As the temperature decreased, the first peak steepened and the structure between the first neighbors approached to the crystalline phase, even though the amorphous and disordered phase remained between the second and third neighbors of the atoms.

The nanoparticle having the diameter equal to 4 nm consists of 2913 atoms in total, with 761 iron atoms and 2152 nickel atoms. In Figure 9 (b), even though the first peaks were always observed during the cooling process, the disordered structure was mainly preserved until 900 K. After that point, the second and third peaks appeared, and at 300 K, mainly, a crystal structure was obtained.

It is evident that all the peaks at 300 K have a broadened shape but the first, second and third peaks located at the same positions as it was found for crystalline counterpart. This means the inner side of the amorphous 4 nm nanoparticle (until 3^{rd} nearest neighbor distance) mostly transformed to the crystal structure at room temperature although the remaining part preserved its disordered amorphous structure. Throughout the amorphous to the crystalline transition process, lattice

parameter decreased from 3.612 Å at 900 K and reached to 3.5 Å at 300 K that is the same value with the lattice parameter of the initially crystalline nanoparticle with 4 nm diameter.

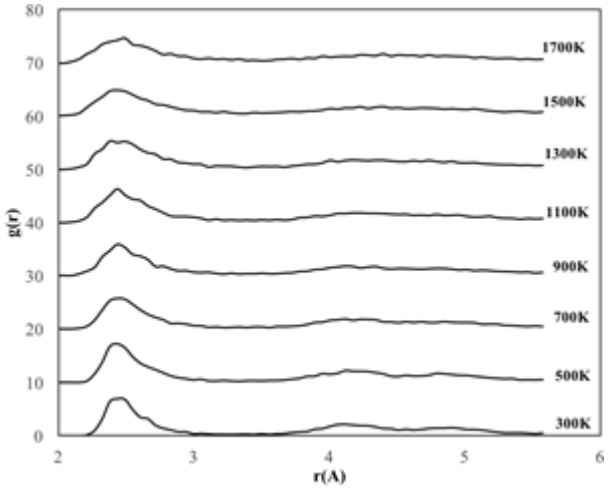

a)

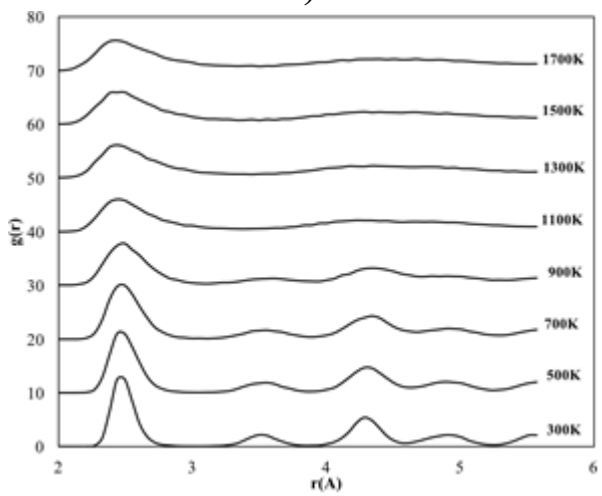

b)

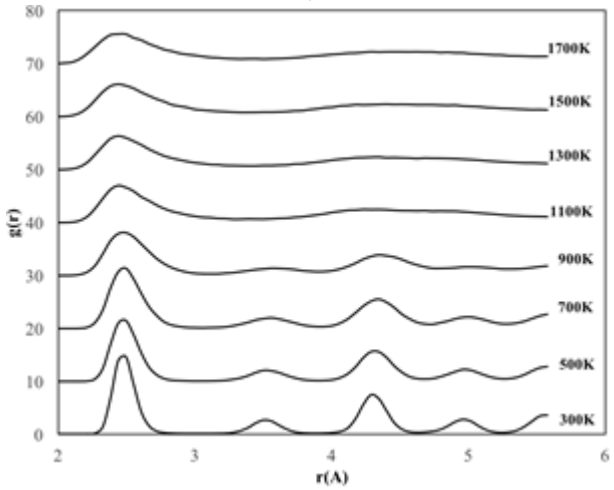

c)

Figure 9. RDF dependences on temperature for (a) 2 nm, (b) 4 nm and (c) 6 nm amorphous nanoparticles

The amorphous nanoparticle with 6 nm diameter includes 2450 Fe atoms and 7334 Ni atoms (9784 atoms in total). Like 4 nm amorphous nanoparticle, the peaks started to appear and the valley

between the peaks became deeper at 900 K, but the amorphous-to-crystalline transformation occurred in a faster and sharper way. At 300 K, the first and the second peak of the overall radial distribution of the initially amorphous 6 nm nanoparticle had almost the same height and width with the RDF of 6 nm crystalline nanoparticle, Figure 9 (c).

Although the other peaks were located in the same position, they had a broader shape compared to the peaks in the RDF of the initially crystalline nanoparticle with 6 nm. This means that the 6 nm nanoparticle, which owned amorphous phase at the beginning, completely transformed to the crystalline phase, even though the final structure has not been as compact as the structure of the initially crystalline nanoparticle with the 6 nm diameter at room temperature. Moreover, during the cooling process, the lattice parameter of the 6 nm particle changed from the 3.556 Å at 900 K, where crystallization started, to 3.5 Å at room temperature which is consistent with the lattice parameter of the initially crystalline nanoparticle and the value stated in the literature [25].

Overall, we observed clearly that, at high temperatures, there was an absence of an order for all initially amorphous nanoparticles. From the RDF graphs of the 2 nm nanoparticles, it has been seen that amorphous structure was preserved during the cooling process even at 300 K. On the other hand, in the RDF figures of the nanoparticles with 4 nm and 6 nm diameter, there was a transition from amorphous phase to the crystal structure at lower temperatures, and 300 K, the complete crystalline structure was obtained in 6 nm nanoparticle with 3.5 Å lattice constant. Although at 300 K, the lattice parameter of both 6 nm and 4 nm nanoparticles reached to 3.5 Å value, the variation in lattice constant of the nanoparticle with 4 nm diameter was higher than 6 nm diameter because of the size effect on the lattice parameter [26].

Moreover, the coordination number change of the 2 nm, 4 nm and 6 nm amorphous nanoparticles with respect to temperature is illustrated in Figure 10.

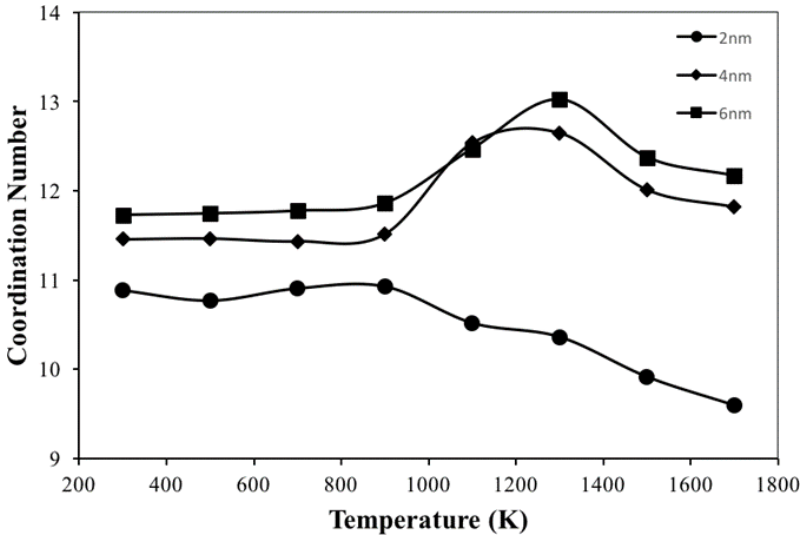

Figure 10. Coordination number change of the amorphous $FeNi_3$ nanoparticle with respect to temperature

According to Figure 10, the coordination number of the amorphous 2 nm particle continuously increased as the temperature approached 300 K, even though it pre- served its amorphous structure during the cooling process. On the other hand, the coordination number of the amorphous nanoparticle with 4 nm diameter reached its maximum value at 1300 K probably because of the sublimation. Then, it stayed at balance around 11 that is very close value with the completely crystalline 4 nm nanoparticle (10.9).

The 6 nm amorphous nanoparticle exhibited a similar trend with the 4 nm nanoparticle, but the coordination number of the 6 nm amorphous nanoparticle reached to 11.2 which is the same coordination value of the initially crystalline 6 nm nanoparticle. This means the initially amorphous nanoparticle with 6 nm diameter completed its crystalline transformation by obtaining same CN value with the initially crystalline nanoparticle.

3.3.Structural evolutions in amorphous $FeNi_3$ NPs

Core-to-surface concentration profiles are essential to observe the atomic movement during heat treatment. The change in the number of Fe and Ni atoms throughout the particles having 2 nm, 4 nm and 6 nm diameter are shown in the following figures. In Figure 11, it is seen that the random mixed atomic patterns of the 2 nm amorphous nanoparticle were preserved as the temperature decreased.

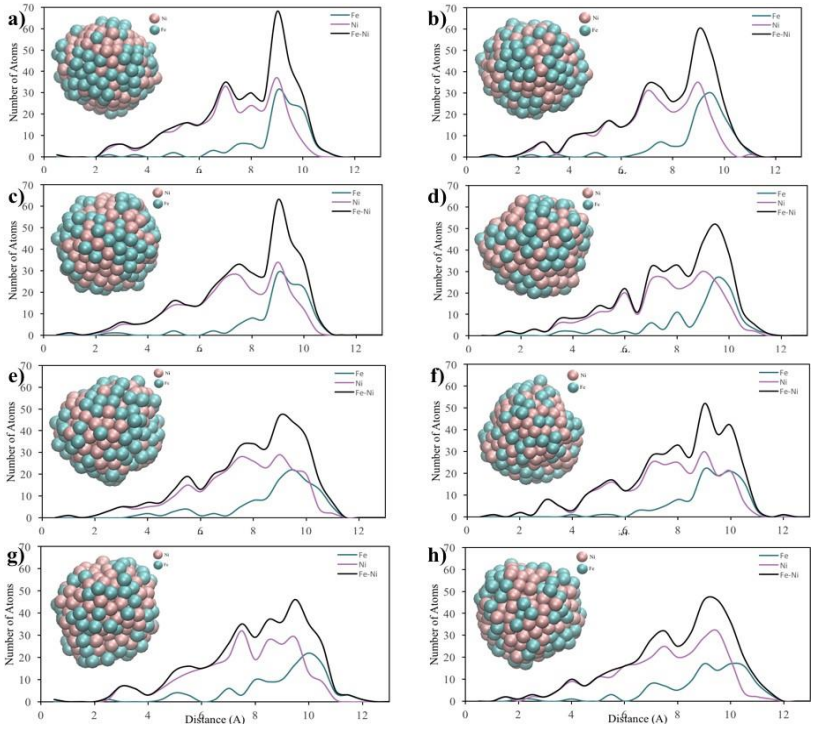

Figure 11. Core-to-surface concentration profiles of Fe and Ni atoms in the 2 nm amorphous nanoparticles at a) 300 K, b) 500 K, c) 700 K, d) 900 K, e) 1100 K, f) 1300 K, g) 1500 K and h) 1700 K

However, Fe atoms diffused from the core to surface, and the initial Fe atomic positions at the core side started to be filled with Ni atoms at lower temperatures. In the end, the main atomic distribution peak of the Fe atoms located at the surface, but Ni atoms spread throughout the particle. From the morphological point of view, it is known that amorphous nanomaterials have unstable structures compared to their crystalline counterparts, so during MD simulations, the shape and surface area of the particles changed to have more stable structures. For example, as the temperature decreased, the irregular shape of the amorphous 2 nm nanoparticle converted to the spherical shape.

According to Figure 12, the melted Fe atoms at the surface stayed during the cooling process and Ni atoms diffused towards the inside of the 4 nm amorphous particle.

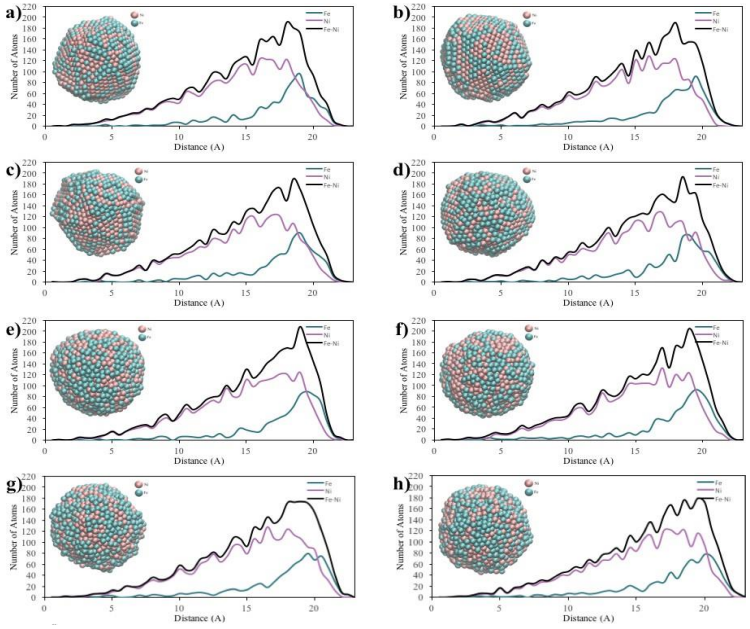

Figure 12. *Core-to-surface concentration profiles of Fe and Ni atoms in the 4 nm amorphous nanoparticles at a) 300 K, b) 500 K, c) 700 K, d) 900 K, e) 1100 K, f) 1300 K, g) 1500 K and h) 1700 K*

Although Ni atoms dominated the core and most of the Fe atoms were located at the surface, the random mixed pattern in the intermediate shell preserved at 300 K. For the 4 nm nanoparticle, it has been observed that the irregular shape of the particles transformed the spherical shape at the onset of the melting; afterward, they reached to a more stable sharp sphere.

In Figure 13, mainly mixed pattern of Fe and Ni atoms obtained at the end of the cooling process, but Ni atoms still dominated the core and melted Fe atoms stayed at the surface, similar to the 4 nm nanoparticle.

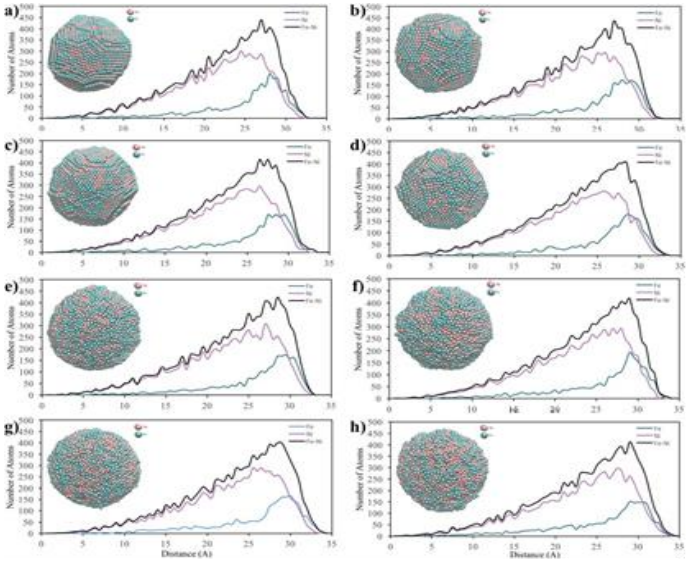

Figure 13. Core-to-surface concentration profiles of Fe and Ni atoms in the 6 nm amorphous nanoparticles at a) 300, K b) 500 K, c) 700 K, d) 900 K, e) 1100 K, f) 1300 K, g) 1500 K and h) 1700 K

Moreover, 6 nm nanoparticle also showed a similar trend with the 4 nm nanoparticle in terms of morphological transformation during the cooling process. With the decreasing temperature, the irregular shape of the 6 nm nanoparticles evaluated smoothly to the spherical shape while melting, and a shape of sharp-sphere was obtained at 300 K which means the 4 nm and 6 nm nanoparticles

had a capability of undergoing a transformation from their initial shapes to geometrically more stable shape.

As it has been explained in the Introduction Section, the difference between atomic sizes of the constituents leads to core-shell structure, in which small atoms are located in the core-side but the bigger ones form an outer shell that surrounds the core. Also, a large difference in the cohesive energy of the atoms causes segregation. In this sys- tem, Fe and Ni atoms have a similar radius and cohesive energy, such as Fe atoms have the 0.126 nm radius with 4.28 eV/atom cohesive energy and Nickel atoms own 0.125 nm radiuses with 4.44 eV/atom cohesive energy [27]. Therefore, the nanoparticles having equal to/larger than 4 nm diameter formed an ordered mixing pattern, rather than segregated or core-shell structure, as it has been expected. Although at room temperature, some Ni atoms stayed at the core side of the smaller particles, as the diameter of the particle size increased to 6 nm, the atomic pattern mainly trans- formed to the ordered mixing pattern and no segregation was observed.

3.4. Voronoi Analysis in crystalline $FeNi_3$ NPs

The Voronoi tessellations of the amorphous nanoparticles with 2 nm, 4 nm and 6 nm diameter at 1700 K and 300 K are shown in Figure 14.

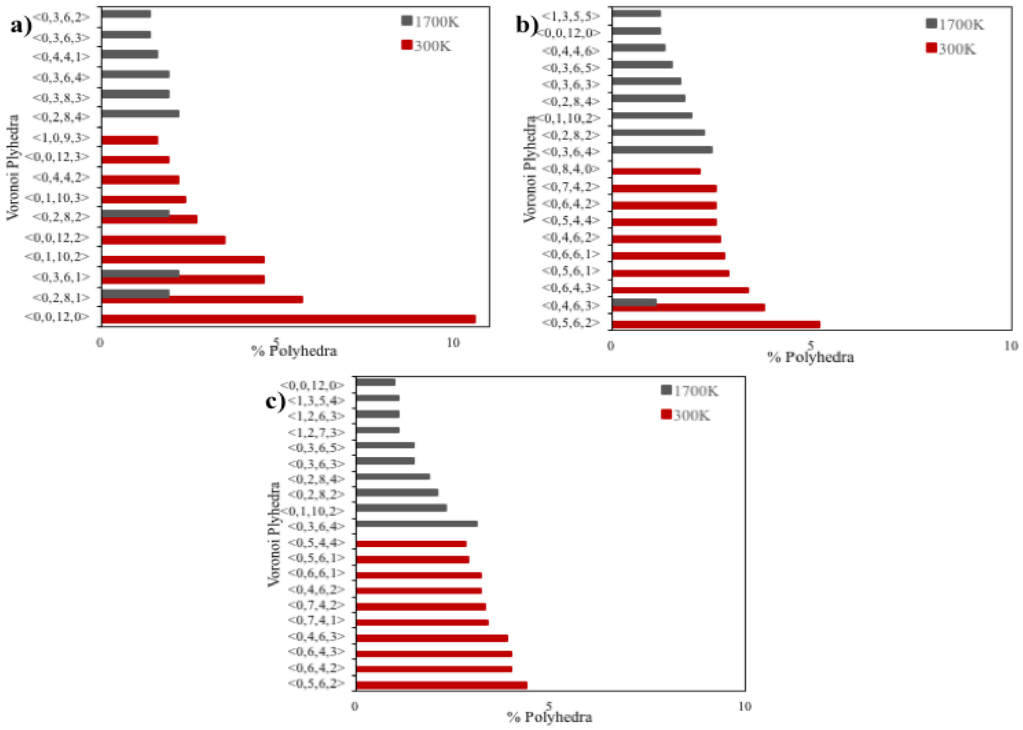

Figure 14. Voronoi analysis of amorphous $FeNi_3$ nanoparticle with a) 2 nm diameter b) 4 nm diameter c) 6 nm diameter

According to Figure 14 (a), none of the polyhedrons in 2 nm amorphous nanoparticle was found in the 2 nm crystalline nanoparticle. This means that amorphous nanoparticle with 2 nm diameter conserved its amorphous structure during the cooling process from 1700 K to 300 K. The vast majority of the Voronoi tessellation of the 2 nm amorphous nanoparticle belonged to <0,0,12,0> polyhedron which showed that the fully icosahedral structure and its deformed forms (<0,1,10,2>, <0,2,8,2>) covered the 2 nm nanoparticle. The other <0,2,8,1> and <0,3,6,1> polyhedral structures

correspond to deformed trigonal prism were also observed in both liquid and solid phase of the 2 nm amorphous nanoparticle.

Due to the fivefold symmetry below the critical sizes, the icosahedral polyhedrons are the stable form of the metallic nanoparticles [28]. However, from the previous studies, it has been shown that the stability of the icosahedral structure decreased when the total number of atoms increased in a nanoparticle [29]. In accordance with the literature, the icosahedral structure <0,0,12,0> disappeared and the trigonal faces decreased to lower than 50% as the size of the particles increased to 4 nm and 6 nm.

According to Figure 14 (b), the main polyhedrons like <0,5,6,2>, <0,6,4,2>, and <0,5,6,1> were found initially amorphous solid nanoparticles having 4 nm diameter. On the other hand, <0,4,6,3> polyhedron structure was observed in both the liquid and the solid phase of the 4 nm amorphous nanoparticle. This means that although 4 nm amorphous and crystalline nanoparticles had some common local atomic arrangement in the solid and liquid phases, the 4 nm nanoparticle with amorphous phase could not completely transformed to the crystalline structure at 300 K.

In Fe-centered Voronoi polyhedra of the 6 nm nanoparticles, Figure 14 (c), it has been observed that all of the local atomic configurations in solid phase were completely different from the liquid phase. Furthermore, most of the polyhedrons in the solid phase were common with the polyhedral shapes of the initially crystalline nanoparticle owing 6 nm diameter in solid phase, such as <0,6,4,2>, <0,5,6,2>, <0,7,4,1>, <0,7,4,2> and <0,5,6,1>. These polyhedrons correspond to the deformed truncated octahedron with its derivatives (tetradecohedron) having $m\bar{3}m$ symmetry. The truncated octahedron is one of the most stable FCC structure because of having the minimum energy for larger nanoparticles [29]. According to the common Voronoi polyhedrons in the 6 nm nanoparticle, it has been seen that the number of rectangular faces of the local polyhedra around Fe atom significantly increased to more than 50% which matched with the distorted FCC lattice structure. Therefore, we can say that the 6 nm amorphous nanoparticle generally transformed to the FCC crystalline lattice structure at 300 K.

Moreover, most of the polyhedron structures in the initially amorphous nanoparticle with 4 nm and 6 nm diameter were common at room temperature, but only a few of them are found in the 2 nm amorphous nanoparticle. This is because 2 nm nanoparticle preserved its amorphous structure throughout the cooling process but the others transformed to the crystalline structure partially or completely. Considering coordination number from the Voronoi analysis, CN of 2 nm amorphous nanoparticle mainly remained higher than 12 which is another proof for the disordered amorphous structure because the amorphous structures may have a more efficient atomic packing [30]. Also, the total coordination numbers of the 6 nm and 4 nm nanoparticles were between 12 and 13 atoms which is consistent with the coordination number of the FCC lattice structure. Therefore, we can conclude that the initial crystalline or amorphous structure did not affect significantly the final FCC structure of the 6 nm nanoparticle at 300 K.

Conclusions

Modeling and simulation study have been performed by means of EAM-MD method in order to investigate the effects of particle size (in 2-6 nm particle size range) and temperature (300-1900 K) on stability and local structural evolutions of equatomic $FeNi_3$ amorphous bulk/nanoalloys at liquid and amorphous solid state. $FeNi_3$ nanosystem was modeled by assuming that, systems with

more than 100 atoms have the same crystal structure as their bulk counterpart. The results of theoretical predictions can be summarized as follows:

1. The three dimensional (3D) atomic configuration of $FeNi_3$ NPs by means of Voronoi analysis reveals that, amorphous nanoparticle with 2 nm diameter conserved its amorphous structure during the cooling process from 1700 K to 300 K. The vast majority of the Voronoi tessellation of the 2 nm amorphous nanoparticle belonged to <0,0,12,0> polyhedron which showed that the fully icosahedral structure and its deformed forms (<0,1,10,2>, <0,2,8,2>) covered the 2 nm nanoparticle. The other <0,2,8,1> and <0,3,6,1> polyhedral structures correspond to deformed trigonal prism were also observed in both liquid and solid phase of the 2 nm amorphous nanoparticle. The main polyhedrons like <0,5,6,2>, <0,6,4,2>, and <0,5,6,1> were found initially amorphous solid nanoparticles having 4 nm diameter. On the other hand, <0,4,6,3> polyhedron structure was observed in both the liquid and the solid phase of the 4 nm amorphous nanoparticle. In Fe-centered Voronoi polyhedra of the 6 nm nanoparticles, it has been observed that all of the local atomic configurations in solid phase were completely different from the liquid phase. Furthermore, most of the polyhedrons in the solid phase were common with the polyhedral shapes of the initially crystalline nanoparticle owing 6 nm diameter in solid phase, such as <0,6,4,2>, <0,5,6,2>, <0,7,4,1>, <0,7,4,2> and <0,5,6,1>. The truncated octahedron is one of the most stable FCC structure because of having the minimum energy for larger nanoparticles and 6 nm amorphous nanoparticle generally transformed to the FCC crystalline lattice structure at 300 K.

2. At high temperatures, there was an absence of an order for all initially amorphous nanoparticles. RDF graphs of the 2 nm nanoparticles reveal that an amorphous structure was preserved during the cooling process even at 300 K. On the other hand, for nanoparticles with 4 nm and 6 nm diameter, there was a transition from amorphous phase to the crystal structure at lower temperatures and at 300 K the complete crystalline structure was obtained in 6 nm nanoparticle with 3.5 Å lattice constant. Although at 300 K, the lattice parameter of both 6 nm and 4 nm nanoparticles reached to 3.5 Å value, the variation in lattice constant of the nanoparticle with 4 nm diameter was higher than for 6 nm diameter because of the size effect on the lattice parameter.

3. Structural analysis on the base of core-to-surface concentration profiles indicated that, the random mixed atomic patterns of the 2 nm amorphous nanoparticle were preserved as the temperature decreased. However, Fe atoms diffused from the core to surface, and the initial Fe atomic positions at the core side started to be filled with Ni atoms at lower temperatures. At the end of cooling process, Fe atoms located at the surface, but Ni atoms spread throughout the particle. During the cooling process of the 4 nm amorphous NP, the melted Fe atoms stayed at the surface and Ni atoms diffused towards the inside of NP. For the 4 nm nanoparticle, it has been observed that the irregular shape of the particles transformed the spherical shape at the onset of the melting; afterward, they reached to a more stable sharp sphere. Although Ni atoms dominated the core and most of the Fe atoms were located at the surface, the random mixed pattern in the intermediate shell preserved at 300 K for 6 nm amorphous NP. Mainly mixed pattern of Fe and Ni atoms obtained at the end of the cooling process, but Ni atoms still dominated the core and melted Fe atoms stayed at the surface, similar to the 4 nm nanoparticle.

4. The coordination number (CN) of the amorphous 2 nm particle continuously increased as the temperature approached 300 K, even though it preserved its amorphous structure during the cooling process. On the other hand, the coordination number of the amorphous nanoparticle with 4 nm

diameter reached its maximum value at 1300 K probably because of the sublimation. Then, it stayed at balance around 11 that is very close value with the completely crystalline 4 nm nanoparticle (10.9). The 6 nm amorphous nanoparticle exhibited a similar trend with the 4 nm nanoparticle, but the coordination number of the 6 nm amorphous nanoparticle reached to 11.2 which is the same coordination value of the initially crystalline 6 nm nanoparticle. This means the initially amorphous nanoparticle with 6 nm diameter completed its crystalline transformation by obtaining same CN value with the initially crystalline nanoparticle.

REFERENCES

[1] Nanoalloys: From Fundamentals to Emergent Applications, ed. F. Calvo, 2-nd edition, 2020; 1-st edition, Elsevier Inc., 2013.

[2] Sh. Moussa, V. Abdelsayed, and M.S. El Shall, Chemical synthesis of metal nanoparticles and nanoalloys, In Nanoalloys, ed. F. Calvo, pp. 1–37, Elsevier Inc., 2013.

[3] Riccardo Ferrando, Julius Jellinek, and Roy L Johnston., Nanoalloys: From Theory to Applications of Alloy Clusters and Nanoparticles, Chem. Rev., 108 (2008) 845–910.

[4] Y. Yao, Ch. Zhang, Y. Fan and J. Zhan, Preparation and microwave absorbing property of porous FeNi powders, Adv. Powd. Tech. 27 (2016) 2285–2290.

[5] V. Solanki, O. I. Lebedev, Md. M. Seikh, N. K. Mahato, B. Raveau, A. K. Kundu, Synthesis and characterization of Co–Ni and Fe–Ni alloy nanoparticles, J. Magn. Magn. Mater. 420 (2016) 39–44.

[6] K. Yatsugi, T. Ishizaki, K. Akedo and M. Yamauchi, Composition-controlled synthesis of solid-solution Fe–Ni nanoalloys and their application in screen-printed magnetic films, J. Nanopart. Res. 21(3) (2019) 60.

[7] P. H. Zhou, L. J. Deng, J. L. Xie, D. F. Liang, L. Chen, and X. Q. Zhao, Nanocrystalline structure and particle size effect on microwave permeability of FeNi powders prepared by mechanical alloying, J. Magn. Magn. Mater. 292 (2005) 325–331.

[8] R. Koohkana, S. Sharafia, H. Shokrollahib and K. Janghorbanb, Preparation of nanocrystalline Fe–Ni powders by mechanical alloying used in soft magnetic composites, J. Magn. Magn. Mater. 320 (2008) 1089–1094.

[9] K. McNamara, S. A. M. Tofail, N. D. Thorat, J.Bauer, J. J. E. Mulvihill, Biomedical applications of nanoalloys, In Nanoalloys, 2-nd edition, ed. F. Calvo, pp. 381-432, Elsevier Inc., 2020.

[10] Z. A. Matysina. A. O. Mekhrabov, Z. M. Babaev, and et al., Impurities in Ni_3Fe Alloys, Phys. Stat. Sol. (b) 138 (1986) 399-406.

[11] A. O. Mekhrabov, Pseudopotential Calculations of Short-Range Atomic Order Characteristics of 3-component Ni_3(Fe, Me) Alloys, Fiz. Metal. Metalloved. 62 (1986) 1023-1025.

[12] A. O. Mekhrabov, Z. M. Babaev, and et al., Pseudopotential Calculations of the Atomic Pair Interaction Energies and Kurnakov Temperature evaluation for Ni_3(Fe, Me) ternary Alloys, Fiz. Metal. Metalloved. 61 (1986) 1089-1093.

[13] Z. A. Matysina, A. O. Mekhrabov, and et al., Impurities in Ni_3Fe Magnetic Alloys, J. Phys. Chem. Sol. 48 (1987) 419-423.

[14] Z. A. Matysina, A. O. Mekhrabov and Z. M. Babaev, Ordering Temperatures and Order Parameters of Ni_3Fe Alloys with Mn and Cr Impurities, Fiz. Metal. Metalloved. 64 (1987) 202-205.

[15] Z. M. Babaev, A. Z. Menshikov, A. O. Mekhrabov, E. S. Valiev, Atomic Ordering in Ni_3(Fe 1-x Mnx) Alloys, Fiz. Metal. Metalloved. 64 (1987) 762-766.

[16] A. O. Mekhrabov, Impurity Effect of Me= Cr, Nb, or Mn Third-Component Atoms on Hyperfine Interactions in Ordered Ni_3Fe Alloys, Hyperfine Interactions 59 (1990), 337-340.
[17] H. P. Cheng and D. E. Ellis., First-principles potentials in modeling structure and thermodynamics of Fe-Ni alloys, Phys. Rev. B 39(17) (1989) 12469–12483.
[18] Y. Mishin, M. J. Mehl, and D. A. Papaconstantopoulos, Phase stability in the Fe-Ni system: Investigation by first-principles calculations and atomistic simulations, Acta Mater. 53(15) (2005) 4029–4041.
[19] T. Halicioglu and C. W. Bauschlicher Jr., Physics of Microclusters, Reports on Progress in Physics 51(6) (1988) 883.
[20] G. Bonny, R. C. Pasianot and L. Malerba, Fe–Ni many-body potential for metallurgical applications, Model. Simul. Mater. Sci. Eng. 17 (2009) 025010.
[21] M. V. Akdeniz and A. O. Mekhrabov, Size dependent stability and surface energy of amorphous FePt nanoalloy, J. of All. Comp. 788 (2019) 787-798.
[22] M. Yalcin, A. O. Mekhrabov and M. V. Akdeniz, Effects of Nanoparticle Geometry and Temperature on the Structural Evolutions in FeCo Nanoalloys, Acta Phys. Pol. A 125(2), (2014) 600-602.
[23] E. Furio, A molecular dynamics primer, Technical report, International School for Advanced Studies (SISSA-ISAS), Trieste, Italy, 1997.
[24] M. E. Tuckerman, J. Alejandre, R. López-Rendón, A. L. Jochim and G. J. Martyna, A Liouville-operator derived measure-preserving integrator for molecular dynamics simulations in the isothermal-isobaric ensemble, J. Phys. A: Mathematical and General, 39(19) (2006) 5629–5651.
[25] I. Chicinas, V. Pop, O. Isnard, J. M. Le Breton and J. Juraszek. Synthesis and magnetic properties of Ni_3Fe intermetallic compound obtained by mechanical alloying. Journal of Alloys and Compounds, 352(1-2):34–40, 2003
[26] W. H. Qi, B. Y. Huang, M. P. Wang, Z. M. Yin, and J. Li. Molecular dynamic simulation of the size- and shape-dependent lattice parameter of small Platinum nanoparticles. Journal of Nanoparticle Research, 11(3):575–580, 2009
[27] P. H. T. Philipsen and E. J. Baerends, Cohesive energy of 3d transition metals: Density functional theory atomic and bulk calculations, Physical Review B, 54(8):5326–5333, 1996.
[28] M. Hanbücken, P. Müller and R.B. Wehrspohn, Mechanical Stress on the Nanoscale: Simulation, Material Systems and Characterization Techniques. Wiley, 2011.
[29] S. Ali, V. S. Myasnichenko and E. C. Neyts, Size-dependent strain and surface energies of gold nanoclusters, Phys. Chem. Chem. Phys., 18(2):792–800, 2016.
[30] D. Bazin, I. Fechete, F. C. Garin, Giovanni Barcaro, F. R. Negreiros, L. Sementa and A. Fortunelli, Reactivity and catalysis by nanoalloys, In Nanoalloys, ed. F. Calvo, pp. 283–344, Elsevier Inc., 2013.

Received: 15.05.2023
Accepted: 30.10.2023

MACHINE SCIENCE
ISSN: 2227-6912
E-ISSN: 2790-0479
2023, № 2 Pages 20 – 27

FUNCTION GENERATION OF A WATT II TYPE PLANAR MECHANISM WITH PRISMATIC OUTPUT USING DECOMPOSITION AND CORRECTION METHOD

Gökhan KIPER

Mechanical Engineering Department, İzmir Institute of Technology, İzmir, Türkiye

E-mail: *gokhankiper@iyte.edu*

http://dx.doi.org/10.61413/SVMW4749

Abstract: The method of decomposition is a useful method for function generation with multi-loop mechanisms. The recently introduced correction methods applied together with the method of decomposition allows the designer to cancel out the errors in the first loop of a two-loop mechanism with the errors in the second loop. In this study, the decomposition and correction method is applied for a Watt II type planar six-link mechanism with prismatic output. Five design parameters are defined for each loop resulting in ten design parameters in total. The design parameters are determined analytically. The generation error is decreased by adjusting free parameters such as the limits of the some joint angles and parameters due to the decomposition of the function to be generated, while considering several constraints such as link lengths ratios and ranges of the joint variables. The success of the method is illustrated with a numerical example.

Keywords: *Function generation, decomposition and correction method, planar Watt II mechanism with prismatic output.*

Introduction.

Recently Kiper et al. [1] have introduced a new kinematic synthesis method for function generating multi-loop mechanisms based on decomposition and correction methods. For a two-loop mechanism, the decomposition method decomposes a function y = f(x) into two as w = g(x) and y = h(w) = h(g(x)) = f(x) [2]. The loops of a two-loop mechanism are to be used to generate the decomposed functions w = g(x) and y = h(w). In general for mechanisms with more than two successive loops, the function to be generated, y = f(x), may be decomposed into as many functions as the number of loops. The three different correction methods introduced in [1] aim neutralizing the generation error of the first loop by matching the errors due to the second loop. The correction method can be generalized for mechanisms with more than two loops as well. Kiper et al. compare their methods with other function generation methods in the literature [3, 4] and demonstrate the superiority of their methods for generation with less errors.

In [1], a Watt II type planar six-link mechanism with revolute joints only is used for an application of the decomposition and correction methods. Via numerical examples it is demonstrated that in general correction methods #2 and #3 provide superior results compared to correction method #1. Correction method #3 requires making use of the derivative of the loop closure equations and hence it is a relatively more complex method to apply. Therefore we choose to use correction method #2 in this study to formulize the function generation of a Watt II type planar six-link mechanism which comprises six revolute joints and a prismatic joint. The prismatic joint is the output of the mechanism. Such mechanisms are quite common in applications, where the first loop is a crank-rocker type four-bar loop and the second loop is a slider-crank loop. Some deep drawing, blanking and knuckle-joint presses comprise such mechanisms. It is not a straightforward task to formulize the design of such mechanisms as a function generation synthesis problem and such formulizations are

kept out of scope of this paper.

The paper is organized as follows: The description of the Watt II type six-link planar mechanism with prismatic output and the formulation for function generation is presented in Section 2. The correction method is explained in Section 3. A numerical example is given in Sections 4. Section 5 concludes the paper.

The Mechanism and Function Generation Problem Definition. The Watt II type planar six-link mechanism in this study is comprises two ternary and four binary links connected to each other by six revolute joints and a prismatic joint (Fig. 1). The I/O equation of a four-bar mechanism is not affected by the scale of the mechanism, and the four-bar loop A_0ABB_0 can be scaled independent from the slider-crank loop B_0CD, so we assume $|A_0B_0| = 1$. Once the synthesis task is done, the designer can scale the four-bar loop A_0ABB_0 with any desired scale ratio.

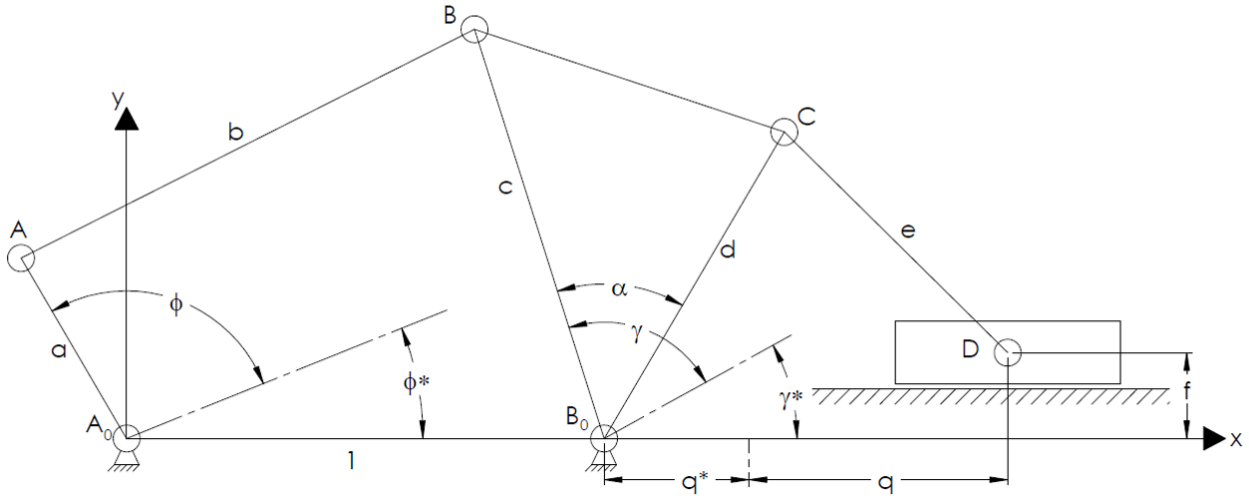

Figure 1. Kinematic diagram of a Watt II mechanism

The origin of the coordinate frame is at A_0 and the x-axis is along A_0B_0. The link lengths of the mechanism for design are $|A_0A| = a$, $|AB| = b$, $|B_0B| = c$, $\uparrow BB_0C = \alpha$, $|B_0C| = d$, $|CD| = e$ and the distance of point D to the x-axis is f. In Fig. 1, it is assumed that the slider displacement direction is along the x-axis, i.e. along A_0B_0. In general there might be a constant angle, say β, between the x-axis and the sliding direction of D. However, notice that the effect of the constant angles α and β to the I/O equation of the slider-crank loop is cumulative, therefore without loss of generality one may assume $\beta = 0$ as in Fig. 1. If the designer wishes to have a nonzero β after the synthesis computations are performed, it is possible to select and arbitrary angle β and modify angle $\uparrow BB_0C$ as $\alpha - \beta$ instead of α.

The input of the mechanism is angle ϕ and the output is the distance q. Angle γ is an intermediate variable to be used as the output of the four-bar loop and at the same time, the input of the slider-crank loop. In general the input angle can be measured from an inclined reference axis which makes an angle ϕ* with the x-axis. ϕ* can be used as a design parameters along with the link lengths. Similarly, angle γ may be measured from a reference axis which makes an angle γ* with the x-axis. Also, the distance q may be measured from a constant distance q* measured from B_0, which can be used as a design parameter.

$y = f(x)$ is to be generated for $x_0 \le x \le x_f$ using the six-link mechanism. The function $y = f(x)$ is decomposed into two as $w = g(x)$ and $y = h(w) = h(g(x)) = f(x)$. The intermediate function $g(\cdot)$ can

be selected arbitrarily. Initial and final values of w and y are computed as $w_0 = g(x_0)$, $w_f = g(x_f)$, $y_0 = f(x_0)$ and $y_f = f(x_f)$. Let $\Delta x = x_f - x_0$, $\Delta w = w_f - w_0$ and $\Delta y = y_f - y_0$. The function variables x, w, y are related with the mechanism variables ϕ, γ, q linearly as follows:

$$\frac{\phi-\phi_0}{\Delta\phi}=\frac{x-x_0}{\Delta x}\ ,\ \frac{\gamma-\gamma_0}{\Delta\gamma}=\frac{w-w_0}{\Delta w}\ ,\ \frac{q-q_0}{\Delta q}=\frac{y-y_0}{\Delta y} \tag{1}$$

where $\phi_0 \le \phi \le \phi_f$, $\gamma_0 \le \gamma \le \gamma_f$, $q_0 \le q \le q_f$ and $\Delta\phi = \phi_f - \phi_0$, $\Delta\gamma = \gamma_f - \gamma_0$, $\Delta q = q_f - q_0$. The limits of the mechanism variables can be chosen arbitrarily. For given desired values of the function variables x, w, y, the corresponding mechanism variables ϕ, γ, q can be determined from Eq. (1) as:

$$\phi=\frac{\Delta\phi}{\Delta x}(x-x_0)+\phi_0\ ,\ \gamma=\frac{\Delta\gamma}{\Delta w}(w-w_0)+\gamma_0\ ,\ \psi=\frac{\Delta\psi}{\Delta y}(y-y_0)+\psi_0 \tag{2}$$

Eq. (2) is used for determining the precision points for the interpolation approximation method. Conversely, x, w, y can be determined in terms of ϕ, γ and q as.

$$x=\frac{\Delta x}{\Delta\phi}(\phi-\phi_0)+x_0\ ,\ w=\frac{\Delta w}{\Delta\gamma}(\gamma-\gamma_0)+w_0\ ,\ y=\frac{\Delta y}{\Delta q}(q-q_0)+y_0 \tag{3}$$

Eq. (3) is used after the synthesis procedure for checking the error between the desired y(x) and the generated y(q).

Formulation of the Design Equations and the Correction Method.

In (Kiper et al., 2017), three correction methods are presented for function generation with two-loop mechanisms. Correction method #1 assumes zero variable references f*, g*, q*, etc., whereas correction method #2 assumes nonzero variable references. The precision points (points of zero error) for both loops are chosen to be common in these two correction methods. In correction method #3, the synthesis procedure for the first loop is the same as the other methods; however instead of equating the precision points of the two loops, the points which correspond to the extrema of the error in the first loop are used for the second loop. It is possible to use all three correction methods for the mechanism in Fig. 1, but for brevity only one correction method is used in this paper. As explained in Section 1, only correction method #2 is used in this paper.

The I/O equation for the four-bar loop A_0ABB_0 reads

$$\left|\overrightarrow{AB}\right|=\left|\overrightarrow{A_oB}-\overrightarrow{A_oA}\right| \Rightarrow b^2=\left(1+cc(\gamma+\gamma^*)-ac(\phi+\phi^*)\right)^2+\left(cs(\gamma+\gamma^*)-as(\phi+\phi^*)\right)^2$$

$$\Rightarrow -\frac{1+a^2-b^2+c^2}{2cc\gamma^*}+\frac{ac\phi^*}{cc\gamma^*}c\phi-\frac{as\phi^*}{cc\gamma^*}s\phi+\frac{ac(\phi^*-\gamma^*)}{c\gamma^*}c(\gamma-\phi)+\frac{as(\phi^*-\gamma^*)}{c\gamma^*}s(\gamma-\phi)+t\gamma^*s\gamma=c\gamma \tag{4}$$

where c, s and t are short for cosine, sine and tangent, respectively. Eq. (4) can be written in polynomial form for five precision points as

$$\sum_{j=1}^{6}P_jf_j(\mathbf{x}_i)-F(\mathbf{x}_i)=0 \ \text{ for i = 1, ..., 5} \tag{5}$$

where $\mathbf{x}_i = \{f_i, g_i\}$, $P_1 = -\dfrac{1+a^2-b^2+c^2}{2cc\gamma^*}$, $P_2 = \dfrac{ac\phi^*}{cc\gamma^*}$, $P_3 = \dfrac{as\phi^*}{cc\gamma^*}$, $P_4 = \dfrac{ac(\phi^*-\gamma^*)}{c\gamma^*}$, $P_5 = \dfrac{as(\phi^*-\gamma^*)}{c\gamma^*}$, $P_6 = t\gamma^*$, $f_1(\mathbf{x}_i) = 1$, $f_2(\mathbf{x}_i) = c\phi_i$, $f_3(\mathbf{x}_i) = -s\phi_i$, $f_4(\mathbf{x}_i) = c(\gamma_i - \phi_i)$, $f_5(\mathbf{x}_i) = s(\gamma_i - \phi_i)$, $f_6(\mathbf{x}_i) = s\gamma_i$ and $F(\mathbf{x}_i) = c\gamma_i$. There are five design parameters (a, b, c, f* and g*) in Eq. (5), so there should be five precision points: $\mathbf{x}_1$, $\mathbf{x}_2$, $\mathbf{x}_3$, $\mathbf{x}_4$ and $\mathbf{x}_5$. However there are six P_j's, hence they cannot be independent of each other. Indeed, $P_4(P_3 - P_2P_6) = P_5(P_2 + P_3P_6)$. The problem can be linearized by using a Lagrange's variable l. Let $P_6 = l$ and $P_j = m_j + n_j l$ for j = 1, 2, 3, 4, 5. Substituting into Eq. (5)

$$\begin{aligned}
&m_1 + n_1\lambda + (m_2 + n_2\lambda)c\phi_1 - (m_3 + n_3\lambda)s\phi_1 + (m_4 + n_4\lambda)c(\gamma_1 - \phi_1) + (m_5 + n_5\lambda)s(\gamma_1 - \phi_1) = c\gamma_1 - \lambda s\gamma_1 \\
&m_1 + n_1\lambda + (m_2 + n_2\lambda)c\phi_2 - (m_3 + n_3\lambda)s\phi_2 + (m_4 + n_4\lambda)c(\gamma_2 - \phi_2) + (m_5 + n_5\lambda)s(\gamma_2 - \phi_2) = c\gamma_2 - \lambda s\gamma_2 \\
&m_1 + n_1\lambda + (m_2 + n_2\lambda)c\phi_3 - (m_3 + n_3\lambda)s\phi_3 + (m_4 + n_4\lambda)c(\gamma_3 - \phi_3) + (m_5 + n_5\lambda)s(\gamma_3 - \phi_3) = c\gamma_3 - \lambda s\gamma_3 \\
&m_1 + n_1\lambda + (m_2 + n_2\lambda)c\phi_4 - (m_3 + n_3\lambda)s\phi_4 + (m_4 + n_4\lambda)c(\gamma_4 - \phi_4) + (m_5 + n_5\lambda)s(\gamma_4 - \phi_4) = c\gamma_4 - \lambda s\gamma_4 \\
&m_1 + n_1\lambda + (m_2 + n_2\lambda)c\phi_5 - (m_3 + n_3\lambda)s\phi_5 + (m_4 + n_4\lambda)c(\gamma_5 - \phi_5) + (m_5 + n_5\lambda)s(\gamma_5 - \phi_5) = c\gamma_5 - \lambda s\gamma_5
\end{aligned} \quad (6)$$

In order for Eqs. (6) to be satisfied for an arbitrary λ, the coefficients of λ and the rest of each equation should be equal to zero. In matrix form:

$$\begin{bmatrix} 1 & c\phi_1 & -s\phi_1 & c(\gamma_1-\phi_1) & s(\gamma_1-\phi_1) \\ 1 & c\phi_2 & -s\phi_2 & c(\gamma_2-\phi_2) & s(\gamma_2-\phi_2) \\ 1 & c\phi_3 & -s\phi_3 & c(\gamma_3-\phi_3) & s(\gamma_3-\phi_3) \\ 1 & c\phi_4 & -s\phi_4 & c(\gamma_4-\phi_4) & s(\gamma_4-\phi_4) \\ 1 & c\phi_5 & -s\phi_5 & c(\gamma_5-\phi_5) & s(\gamma_5-\phi_5) \end{bmatrix} \begin{bmatrix} m_1 \\ m_2 \\ m_3 \\ m_4 \\ m_5 \end{bmatrix} = \begin{bmatrix} c\gamma_1 \\ c\gamma_2 \\ c\gamma_3 \\ c\gamma_4 \\ c\gamma_5 \end{bmatrix} \text{ and } \begin{bmatrix} 1 & c\phi_1 & -s\phi_1 & c(\gamma_1-\phi_1) & s(\gamma_1-\phi_1) \\ 1 & c\phi_2 & -s\phi_2 & c(\gamma_2-\phi_2) & s(\gamma_2-\phi_2) \\ 1 & c\phi_3 & -s\phi_3 & c(\gamma_3-\phi_3) & s(\gamma_3-\phi_3) \\ 1 & c\phi_4 & -s\phi_4 & c(\gamma_4-\phi_4) & s(\gamma_4-\phi_4) \\ 1 & c\phi_5 & -s\phi_5 & c(\gamma_5-\phi_5) & s(\gamma_5-\phi_5) \end{bmatrix} \begin{bmatrix} n_1 \\ n_2 \\ n_3 \\ n_4 \\ n_5 \end{bmatrix} = \begin{bmatrix} -s\gamma_1 \\ -s\gamma_2 \\ -s\gamma_3 \\ -s\gamma_4 \\ -s\gamma_5 \end{bmatrix} \quad (7)$$

m_1, m_2, m_3, m_4, m_5, n_1, n_2, n_3, n_4 and n_5 are solved from Eqs.

Ошибка! Источник ссылки не найден. by matrix inversion. λ is solved from $P_4(P_3 - P_2P_6) = P_5(P_2 + P_3P_6)$:

$$\begin{aligned}
&P_4(P_3 - P_2P_6) - P_5(P_2 + P_3P_6) = (m_4 + n_4\lambda)\left[m_3 + n_3\lambda - \lambda(m_2 + n_2\lambda)\right] - (m_5 + n_5\lambda)\left[m_2 + n_2\lambda + \lambda(m_3 + n_3\lambda)\right] = 0 \\
&\Rightarrow \left\{\begin{aligned}&(n_3n_5 + n_2n_4)\lambda^3 + \left[m_5n_3 + m_4n_2 + n_5(m_3 + n_2) + n_4(m_2 - n_3)\right]\lambda^2 \\ &+ \left[m_5(m_3 + n_2) + m_2n_5 + m_4(m_2 - n_3) - m_3n_4\right]\lambda + m_2m_5 - m_3m_4\end{aligned}\right\} = 0
\end{aligned} \quad (8)$$

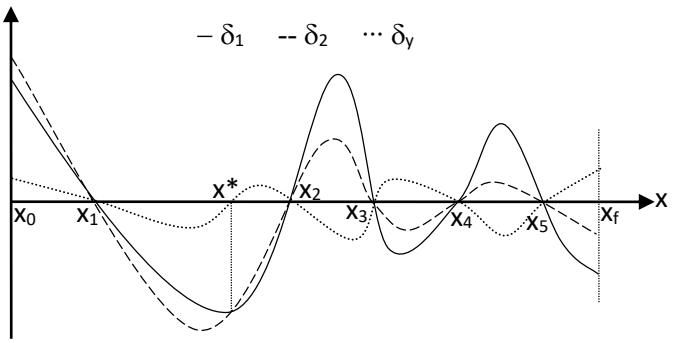

Figure 2. Error curves for the loops (δ_1 and δ_2) and function output (δ_y)

Eq. **Ошибка! Источник ссылки не найден.** is a cubic equation in λ and can be solved analytically. Either there are one real and two imaginary solutions or three real solutions. In case of multiple solutions either solution can be used. Then, $P_j = m_j + n_j\lambda$ are determined for j = 1, 2, 3, 4, 5.

Finally, the design parameters are computed as $\gamma^* = \tan^{-1} P_6$, $\phi^* = \text{atan2}(P_2, P_3)$, $a = \frac{P_4 c\gamma^*}{c(\phi^* - \gamma^*)}$, $c = \frac{ac\phi^*}{P_2 c\gamma^*}$ and $b = \sqrt{1 + a^2 + c^2 + 2cc\gamma^* P_1}$. $\gamma^* = \tan^{-1} P_6 + \pi$ is also possible. Once γ^* value is selected, ϕ^*, a, c and b are uniquely determined in terms of the P_j's, provided that b is real. a or c may be negative, in which case the limits of ϕ or γ should be increased by π. The resulting error variation is zero, that is $\delta_1 = w_{desired} - w_{generated1} = 0$, at least at five precision points (x_1, x_2, x_3, x_4 and x_5) if there is no branching problem, i.e. if $\delta_1 = 0$ at all precision points in the same assembly mode of the loop. The variation of the error curve δ_1 with respect to the function input x looks like the curve in Fig. 2.

In order to be able to compare the errors due to both loops, we assume that the outputs of both the four-bar and the slider-crank loops are link BB_0C and the output variable is γ. Hence we assume that slider displacement q is the input of the slider-crank loop and hence q is known as a linear function of the desired y values. The resulting γ as the output of the loop, and hence w values are obtained from the I/O equation of the slider-crank loop. Let $\delta_2 = w_{desired} - w_{generated2}$ as the error for given $y_{desired}(x)$ and the corresponding linearly related q values. For the dimensional synthesis of the slider-crank loop, the same precision points as the four-bar loop are used and δ_2 and δ_1 are forced to be approximately equal by changing the free variables such as the angle limits ϕ_0, ϕ_f, γ_0, γ_f. Changing linear variable limits q_0, q_f only affects the scale of the slider-crank loop, but has not effect on the amount of the generation error. The I/O equation for the slider-crank loop is given by

$$\begin{aligned}
&\left|\overrightarrow{CD}\right| = \left|\overrightarrow{B_oD} - \overrightarrow{B_oC}\right| \Rightarrow e^2 = \left[q^* + q - dc(\gamma + \gamma^* - \alpha)\right]^2 + \left[ds(\gamma + \gamma^* - \alpha) - f\right]^2 \\
&\Rightarrow q^{*2} + d^2 - e^2 + f^2 + 2q^*q + q^2 - 2d(q^* + q)c(\gamma + \gamma^* - \alpha) - 2dfs(\gamma + \gamma^* - \alpha) = 0 \qquad (7) \\
&\Rightarrow \left\{ \begin{array}{c} \frac{q^{*2} + d^2 - e^2 + f^2}{2dc(\gamma^* - \alpha)} + \frac{q^*}{dc(\gamma^* - \alpha)} q + \frac{1}{2dc(\gamma^* - \alpha)} q^2 + t(\gamma^* - \alpha) qs\gamma \\ + \left[q^* t(\gamma^* - \alpha) - f\right] s\gamma - \left[q^* + ft(\gamma^* - \alpha)\right] c\gamma \end{array} \right\} = qc\gamma
\end{aligned}$$

Eq. (7) can be written in polynomial form Eq. (5) for five precision points where $\mathbf{x}_i = \{\gamma_i, q_i\}$, $P_1 = \frac{q^{*2} + d^2 - e^2 + f^2}{2dc(\gamma^* - \alpha)}$, $P_2 = \frac{q^*}{dc(\gamma^* - \alpha)}$, $P_3 = \frac{1}{2dc(\gamma^* - \alpha)}$, $P_4 = t(\gamma^* - \alpha)$, $P_5 = q^* t(\gamma^* - \alpha) - f$, $P_6 = q^* + ft(\gamma^* - \alpha)$, $f_1(\mathbf{x}_i) = 1$, $f_2(\mathbf{x}_i) = q_i$, $f_3(\mathbf{x}_i) = q_i^2$, $f_4(\mathbf{x}_i) = q_i s\gamma_i$, $f_5(\mathbf{x}_i) = s\gamma_i$, $f_6(\mathbf{x}_i) = -c\gamma_i$ and $F(\mathbf{x}_i) = q_i c\gamma_i$. The five precision points are selected as a function of y_i, hence as a function of x_i for i = 1, …, 5, where x_i are the precision points used for the four-bar loop. There are six P_j's in terms of five design parameters: α, d, e, f and q*. P_j's are interrelated as $P_2(1 + P_4^2) - 2P_3(P_4P_5 + P_6) = 0$. Let $P_4 = \lambda$ and $P_j = m_j + n_j\lambda$ for j = 1, 2, 3, 5, 6. Substituting into Eq. (7):

$$\begin{aligned}
&m_1+n_1\lambda+(m_2+n_2\lambda)q_1+(m_3+n_3\lambda)q_1^{\,2}+(m_5+n_5\lambda)s\gamma_1-(m_6+n_6\lambda)c\gamma_1=q_1c\gamma_1-\lambda q_1s\gamma_1\\
&m_1+n_1\lambda+(m_2+n_2\lambda)q_2+(m_3+n_3\lambda)q_2^{\,2}+(m_5+n_5\lambda)s\gamma_2-(m_6+n_6\lambda)c\gamma_2=q_2c\gamma_2-\lambda q_2s\gamma_2\\
&m_1+n_1\lambda+(m_2+n_2\lambda)q_3+(m_3+n_3\lambda)q_3^{\,2}+(m_5+n_5\lambda)s\gamma_3-(m_6+n_6\lambda)c\gamma_3=q_3c\gamma_3-\lambda q_3s\gamma_3\\
&m_1+n_1\lambda+(m_2+n_2\lambda)q_4+(m_3+n_3\lambda)q_4^{\,2}+(m_5+n_5\lambda)s\gamma_4-(m_6+n_6\lambda)c\gamma_4=q_4c\gamma_4-\lambda q_4s\gamma_4\\
&m_1+n_1\lambda+(m_2+n_2\lambda)q_5+(m_3+n_3\lambda)q_5^{\,2}+(m_5+n_5\lambda)s\gamma_5-(m_6+n_6\lambda)c\gamma_5=q_5c\gamma_5-\lambda q_5s\gamma_5
\end{aligned} \tag{8}$$

Separating the coefficients of λ and the rest of each equation in Eqs. (8) and writing in mat-rix form:

$$\begin{bmatrix}1 & q_1 & q_1^{\,2} & s\gamma_1 & -c\gamma_1\\ 1 & q_2 & q_2^{\,2} & s\gamma_2 & -c\gamma_2\\ 1 & q_3 & q_3^{\,2} & s\gamma_3 & -c\gamma_3\\ 1 & q_4 & q_4^{\,2} & s\gamma_4 & -c\gamma_4\\ 1 & q_5 & q_5^{\,2} & s\gamma_5 & -c\gamma_5\end{bmatrix}\begin{bmatrix}m_1\\ m_2\\ m_3\\ m_5\\ m_6\end{bmatrix}=\begin{bmatrix}q_1c\gamma_1\\ q_2c\gamma_2\\ q_3c\gamma_3\\ q_4c\gamma_4\\ q_5c\gamma_5\end{bmatrix}\text{ and }\begin{bmatrix}1 & q_1 & q_1^{\,2} & s\gamma_1 & -c\gamma_1\\ 1 & q_2 & q_2^{\,2} & s\gamma_2 & -c\gamma_2\\ 1 & q_3 & q_3^{\,2} & s\gamma_3 & -c\gamma_3\\ 1 & q_4 & q_4^{\,2} & s\gamma_4 & -c\gamma_4\\ 1 & q_5 & q_5^{\,2} & s\gamma_5 & -c\gamma_5\end{bmatrix}\begin{bmatrix}n_1\\ n_2\\ n_3\\ n_5\\ n_6\end{bmatrix}=\begin{bmatrix}-q_1s\gamma_1\\ -q_2s\gamma_2\\ -q_3s\gamma_3\\ -q_4s\gamma_4\\ -q_5s\gamma_5\end{bmatrix} \tag{9}$$

After m_1, m_2, m_4, m_5, m_6, n_1, n_2, n_4, n_5 and n_6 are solved from Eqs. (9) by matrix inversion, λ is determined using $P_2\left(1+P_4^{\,2}\right)-2P_3\left(P_4P_5+P_6\right)=0$:

$$\begin{aligned}
&(m_2+n_2\lambda)(1+\lambda^2)-2(m_3+n_3\lambda)(\lambda(m_5+n_5\lambda)+m_6+n_6\lambda)=0\\
\Rightarrow\;&(n_2-2n_3n_5)\lambda^3+\left[m_2-2(m_3n_5+n_3(m_5+n_6))\right]\lambda^2+\left[n_2-2(n_3m_6+m_3(m_5+n_6))\right]\lambda+m_2-2m_3m_6=0
\end{aligned} \tag{10}$$

Eq. (10) can be analytically solved and results in either one or three real solutions for λ. Once λ is determined or selected, $P_3=\lambda$ and $P_j=m_j+n_j\lambda$ are determined for j = 1, 2, 4, 5, 6. Finally the design parameters are solved as $\alpha=\gamma^*-\tan^{-1}P_4$ or $\alpha=\gamma^*-\tan^{-1}P_4+\pi$, $d=1/\left(2c(\gamma^*-\alpha)P_3\right)$, $q^*=P_2/(2P_3)$, $f=q^*P_4-P_5$ and $e=\sqrt{q^{*2}+d^2+f^2-P_1/P_3}$. α is selected so that d is positive. e, f and q* are determined uniquely provided that e is real.

Representative δ_1 and δ_2 variations versus the function input x are illustrated in Fig. 2. As a result of the whole design process, the q output values of the 6-link mechanism result in corresponding $y_{generated}$ values as the output of the generated function. For given function input x, and hence corresponding mechanism input angle ϕ, the error variance $\delta_y = y_{desired} - y_{generated}$ is also depicted in Fig. 2. Definitely $\delta_y = 0$ at the precision points x_1, x_2 and x_3. There may be other points where $\delta_y = 0$ whenever δ_1 curve intersects δ_2, such as x* in Fig. 2.

The closer δ_1 and δ_2 curves, the lower are the δ_y values. In order to obtain lower δ_y error values the designer can adjust several freely selected parameters such as the limits ϕ_0, ϕ_f, γ_0, γ_f of the input joint variable ϕ and intermediate joint variable γ of the mechanism. Also, it is possible to adjust the intermediate function g(·) for most of the functions. When a software such as Microsoft Excel® is used for the computations, the designer can make use of spin buttons for varying the limits of the ϕ, γ and q and, if available, the intermediate function parameter(s) for g(·). By continuously changing the free parameters, the designer can immediately see the tendency of change in the error variations

δ_1, δ_2 and δ_y. At the same time, it is possible to monitor a proper norm of the error, such as the maximum error $|\delta_y|_{max}$ or rms error of δ_y and minimize it. Meanwhile, certain design considerations such as maximum link length to minimum link length ratio, transmission angles, etc. can be monitored.

Numerical Example

The formulations in Section 3 are implemented in Excel and a design environment is constructed which can be used for any arbitrary function. For the example in Fig. 3, the function to be generated is $y = x^2$ for $1 \le x \le 5$. The intermediate function is $g(x) = x^k$, where k is an adjustment parameter for the designer. The synthesis computations described in Section 3 are implemented in the Loop1 and Loop2 sheets. In the sheet shown in Fig. 3 the designer can adjust the joint variable limits ϕ_0, ϕ_f, γ_0, γ_f, q_0, q_f with spin buttons; the configuration of the loops (config1 and config2); and select the Lagrange variable values λ_1 and λ_2 for the two loops – each out of three possible solutions from their respective cubic equations. By these adjustments, error variation curves δ_1, δ_2 and δ_y are monitored simultaneously. Also the maximum error $|\delta_y|_{max}$ and the ratio of the longest link (better less than 10) to the shortest link is monitored. Also the joint variable ranges $\Delta\phi$ and $\Delta\gamma$ should not be too small (better more than 20°). Also the mechanism is drawn and its motion can be simulated with a spin button. A good result is obtained usually in less than in hour – in less time than running any numerical optimization algorithm.

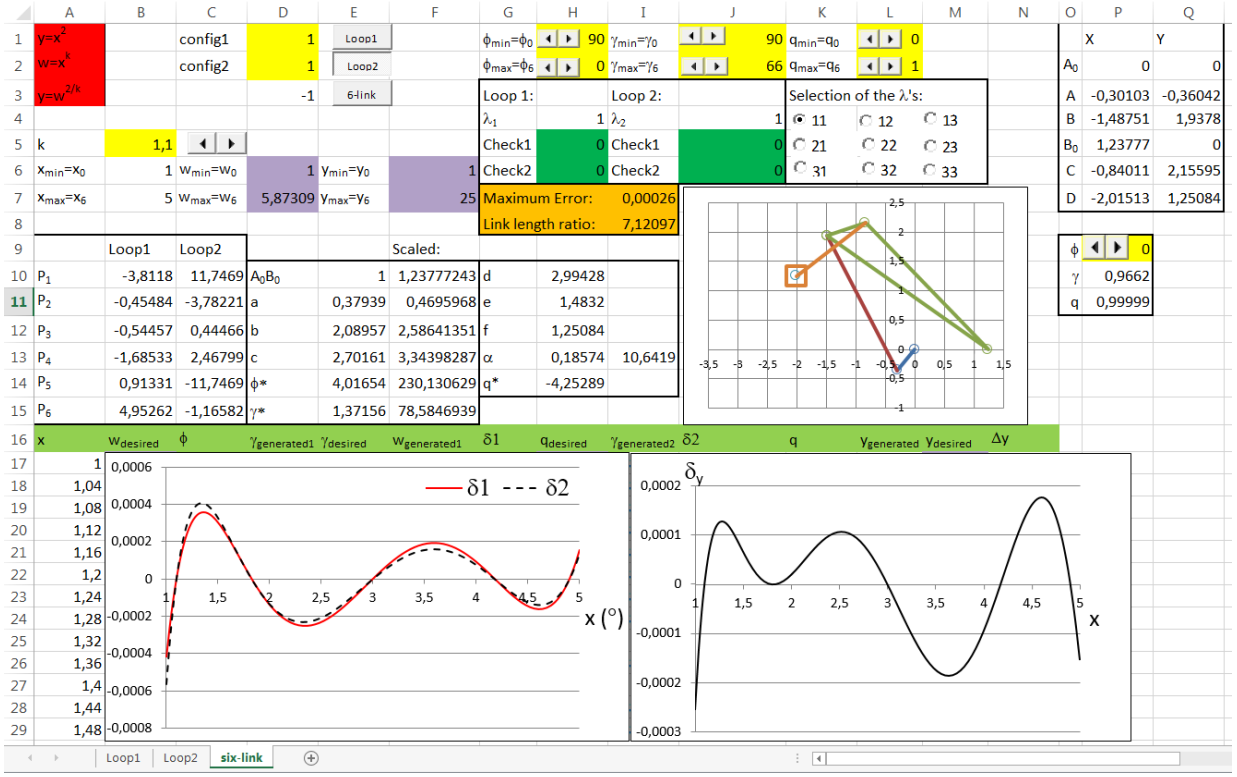

Figure 3. Excel design sheet

After several trials, a good result for the maximum error $|\delta_y|_{max} = 2.6 \times 10^{-4}$ is obtained for $|A_0B_0| = 1$, $|A_0A| = a = 0.379$, $|AB| = b = 2.090$, $|B_0B| = c = 2.702$, $\phi^* = 230.1°$, $\gamma^* = 78.6°$, $|B_0C| = d = 2.994$, $|CD| = e = 1.483$, $D_y = f = 1.251$, $\alpha = 10.6°$ and $q^* = -4.253$. The link lengths 1, a, b, c of the four-bar loop can be scaled arbitrarily. It is observed during the computations that the slider variable

q has no effect on the error variations. The designer can adjust $\Delta q = q_f - q_0$ in order to scale the slider-crank loop link lengths d, e, f. The slider direction can also be adjusted by modifying the angle α as described in Section 2.

Conclusions

In this paper, the method of decomposition and correction is applied for a Watt II type planar six-link mechanism with prismatic output. An analytical method for determining five design parameters for each loop, hence a total number of ten design parameters is presented. There are several free design parameters, such as the limits of the input and intermediate angles of the mechanism and the parameter or parameters that appear during the decomposition of the function to be generated. Also there may be multiple solutions due to the solution of the nonlinear equation in terms of Lagrange parameters. These free design parameters and options for the Lagrange parameters gives a great amount of flexibility to the designer in order to minimize the generation error while considering several constraints such as link lengths ratios and ranges of the joint variables. The method presented in the paper is illustrated with a numerical example. $y = x^2$ is generated for $1 \leq x \leq 5$ with a maximum error value of 2.6×10^{-4} for y. The generation precision is very good when compared to the other results in the literature.

Acknowledgments

The teachings of Prof. Dr. Tech. Sc. Rasim Alizade are gratefully acknowledged. Also Dr. Can Dede, Mr. Omar Maaroof, Ms. Merve Özkahya and Mr. Cevahir Karagöz are acknowledged for the discussions on the subject of this paper.

REFERENCES

[1] Kiper G., Dede M. İ. C., Maaroof O. W., Özkahya M. (2017). *Function generation with two loop mechanisms using decomposition and correction method.* Mech. Mach. Theory, 110:16-26.

[2] Kinzel E. C., Schmiedeler J. P., Pennock G. R. (2007). *Function generation with finitely separated precision points using geometric constraint programming.* ASME J. Mech. Des., 129:1185-1190.

[3] Alizade R. I., Aydazade K. P., Novruzbekov I. G. (1980). *Analysis and synthesis of planar mechanisms by using decomposition method, J*. Mechanics of Machines, The Academy of Sciences of the USSR, 57, 26-32.

[4] Hwang WM, Chen Y. J. (2010). *Defect-free synthesis of Stephenson-II function generators.* ASME J. Mech. Rob., 2(4): 041012.

[5] Sancibrian R. (2011). *Improved GRG method for the optimal synthesis of linkages in function generation problems.* Mech. Mach. Theory, 46(10): 1350-1375.

Received: 19.04.2023
Accepted: 15.10.2023

MACHINE SCIENCE
ISSN: 2227-6912
E-ISSN: 2790-0479
2023, № 2 Pages 28 - 39

EVALUATION OF THE ENERGY EFFICIENCY OF THE NEW MODEL OF SUCKER-ROD PUMPING UNIT

Beyali AHMEDOV[1,a*], Isa KHALILOV[1,b], Anar HAJIYEV[1,c]

[1]Department of Machine design and industrial technologies, Azerbaijan Technical University, Baku, Azerbaijan

*E-mail: *[a]ahmedov.beyali@mail.ru, [b]khalilov@aztu.edu.az, [c]anar_hajiyev_1991@mail.ru*

http://dx.doi.org/10.61413/DOVZ1701

Abstract: As is known, in world, oil production is carried out both in the sea and in oil fields on land. For the mechanized exploitation of oil fields on land, in most cases used different type of sucker-rod pumps. The main object of the study of the article is a new constructive solution of the pumping unit, the novelty of which is approved by the ownership certificates. The main factor characterizing the operation of pumping units is its quality indicators such as metal consumption, reliability, efficiency and energy consumption. When switching from a balanced sucker-rod pumping unit to an unbalanced the efficiency factor decreases from 0.834 to 0.65 and the operating power factor decreases from 0.605 to 0.312. In this case, power losses increase sharply not only in transmissions, but also in energy distribution networks. If the engine is not fully loaded or is not selected correctly, then these energy coefficients decrease even more. The selection of engine power is performed according to the worst conditions, i.e. the cyclic mode of operation of an unbalanced pumping unit. Despite this, it can be said that in almost all oil fields, the power of asynchronous motors is greatly exaggerated, which causes additional losses. In article proposed expressions for determining the optimal power of the electric motor were proposed, taking into account the efficiency factor of the balancing device during the balancing of the proposed new constructive solution of the beamless pumping unit with a combined, movable counter weights and rotary counter weights. This allows to prevent excess energy consumption and reduce energy costs. Which is very important in the era of globalization, when energy prices are rising sharply.

Keywords: *oil, pumping unit, efficiency, balancing, electric motor.*

Introduction.

Oil extraction has important influence for the economic development of many countries, including the Middle East, North Africa, some countries of the America and the CIS. In this regard, the development of technologies in the oil industry is of particular importance. Today, most oil wells are onshore and are equipped with rocking machines, also known as sucker-rod pumping unit. These pumps are equipped with individual drives and are installed in wells, connected to the drive through a flexible mechanical connection called a rod column [1, 2, 3].

Sucker-rod pumping unit have played a key role in oil operations since the 20th century, and are considered the most reliable and easily accessible maintenance equipment, according to experts [4]. These pumping systems incorporate a four-bar mechanism that converts the rotary motion of the motor into vertical motion of the rods and consist of several independent assembly units [5]. Considering that most onshore fields are in the late production stage, characterized by a decrease in well productivity and a decrease in crude oil prices on world markets, increasing the energy efficiency of mechanized oil production methods becomes especially relevant. The efficiency and reliability of these pumping systems play an important role in determining the net return on oil production while minimizing energy costs.

Formulation of the problem.

In many countries, the exploitation of oil wells on land is carried out directly with the help of rod well pumps. Statistics show that about 2/3 of active wells are operated by rod well pumps. To lift the oil from inside the well, to ensure the operation of the well pumps with a rod that is lowered into the well, a device called sucker-rod pumping unit, which are ground equipment, is used. The rod well pump and sucker-rod pump is the most widespread mechanized complex used in the artificial extraction of oil, distinguished by its simple operation, high reliability, and satisfactory productivity. Undoubtedly, the sucker-rod pumping unit is the leading point of this mechanized complex. It is the number of trips of the suspension point of the sucker-rod pumping unit, the length of the travel path, the power of the electric motor of the mechanical transmission, the number of transmissions, and the structural features that determine the effective operation and economic efficiency of the well. For this reason, in order to ensure the operation of onshore wells, serial production of pumping units with the most diverse designs is organized in many countries of the world.

At present, beam and beamless sucker-rod pumping unit are used for the mechanization of rod well pumps. Although in practice more beam sucker-rod pumping unit are used, these machines differ in that the cost is high and the weight is heavy due to the high metal capacity. This factor creates obstacles to its installation in harsh and unfavorable climatic conditions, as it causes serious requirements to be placed on the foundation built for the installation of the device [6, 7].

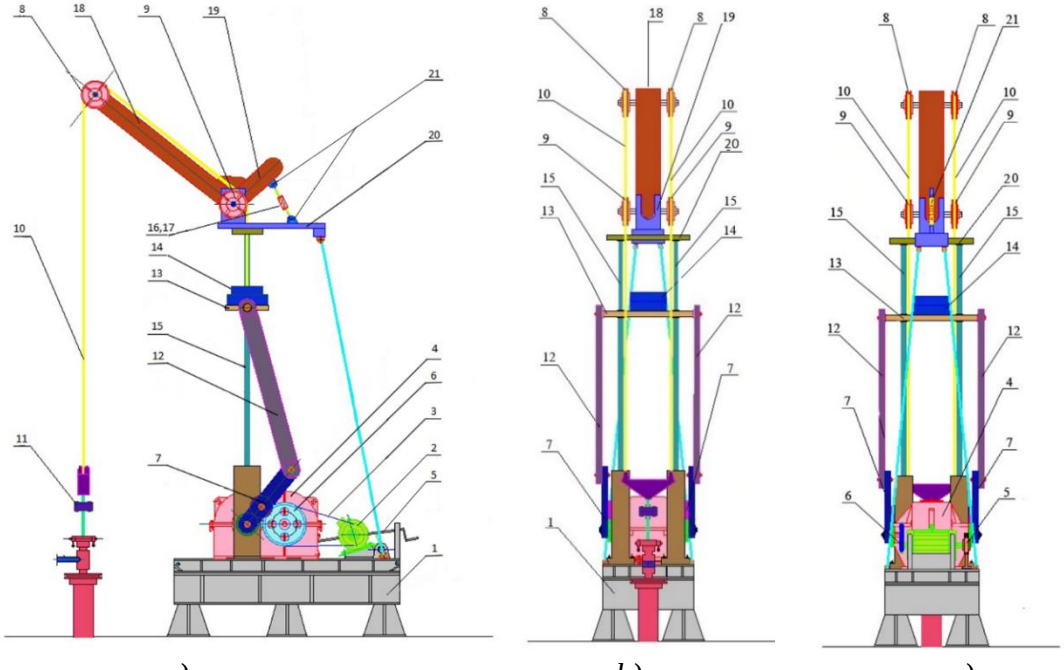

a) *b)* *c)*

Figure 1. New constructive solution of beamless pumping unit consisting of the slider-crank mechanism and the rope-block system:
a - side view; b - front view; c - rear view

One of the main solutions to these problems is to use beamless sucker-rod pumping units, which dispense with the balancer and balancer head, which make up most of the pumping units metal capacity. At the same time, it should be specially noted that, in comparison with beam pumping units, the regularities of movement of the rods suspension point and the dynamic forces affecting its construction in beamless pumping units are significantly different in a positive sense [8, 9]. Taking into account the above mentioned, at the department of “Mechatronics and machine design” of the Azerbaijan Technical University has lower metal capacity, compact overall dimensions, the regularity of movement of the suspension point is closer to the harmonic law, high reliability and low energy

consumption, the originality of the construction is approved by Eurasian Patent Organization [10] and the Intellectual Property Agency of the Republic of Azerbaijan [11] the construction of a new beam-less sucker-rod pumping unit consisting of a rope-block and crank-slide converter mechanism has been developed .

At Figure 1 shown the overview of the new constructive solution of the sucker-rod pumping unit [12]. The new constructive solution of the sucker-rod pumping unit consist from frame (1), three-phase short-circuited asynchronous motor (2), V-belt drive (3), rigidly connected two-flow three-stage reducer (4), on the drive shaft of which on one side mounted double-shaped brake (5) and on the other side V-belt pulley (6), and on the driven shaft of its installed two cranks (7); guide blocks (8, 9), ropes (10) connected to the rods suspension point (11). The converting mechanism, which consists of two slider-crank linkage (12), converts the rotational motion of the crank into the upstroke and downstroke movement of the rod suspension point. The mechanical transmission has counterweights whose weight can be adjusted (14), located on a movable cross beam (13), which is connected with hinge joint to the connecting-rod.

The guide blocks are surrounded by a flexible rope, one end of which is connected to the movable beam, and the other end is connected to the rods suspension point. In addition, the mechanical drive has a guide system consisting of two vertically located cylindrical tubes (15) and the movable beam. The mechanical transmission has articulated front (18) and rear (19) arms, which can be adjusted by using (16,17) screw tensioners, a fixed cross beam (20) rigidly connected to the guide tubes. The screw tensioner (21) is connected to the frame of the construction, as well as to the joints with the front and rear arms.

The converting mechanism is used on the pumping unit to ensure the upstroke and downstroke movement of the rods column. Currently, the four-link hinged slider-crank linkage mechanism is used in the converting mechanisms of the pinches. It is known that the purpose of kinematic analysis of each hinged mechanism is to determine the displacement, velocity and acceleration of its corresponding points [13, 14, 15].

The operation of sucker-rod pumping units meeting the set requirements under the given conditions is characterized by its quality indicators. The main quality indicators of modern sucker-rod pumps include the efficiency of the mechanical system that makes up it, as well as the energy consumption of its engine. These two quality indicators, which are closely related to each other, are the main factors that determine both productivity and economic efficiency of the sucker-rod pump [16].

At present, when determining the useful work coefficient of the mechanical transmission of the rod well pump, expressions built on the “sequential” scheme are used. At this time, it is assumed that the transfer of energy is carried out in one direction. The transmitted power is determined based on the power of the driving engine. In this case, the total losses are defined as the sum of the energy losses in each element of the transmission. The total useful work coefficient is determined as the product of the useful work coefficients of the separate pairs that make up the transmission [17].

As is known, the useful work coefficient of the mechanical transmission of the rod well pump depends on the ratio of the good work done during the cyclic movement of the rod column to the total work spent by the engine of the transmission. Let's consider the process of transferring energy from individual blocks to each other according to the adopted structural scheme [18, 19].

Some work must be done to raise the rods column between the actuator and the balancing device of a pumping unit equipped with a balanced device. During the upward movement of the rods column,

this energy is transferred from the balancing device to the actuator device, and during its downward movement from the actuator device to the balancing device [20, 21].

Successful competition in the market economy is possible only if the costs incurred in the production of the product are minimal. For the case studied, it is related to the cost of electricity during oil production through sucker-rod pumping unit. Recently, technological operations requiring additional energy costs have been applied due to the decrease in the flow rate of the wells, which leads to an increase in the cost of each ton of extracted oil. In this regard, one of the important issues is finding ways to apply energy saving techniques and technologies.

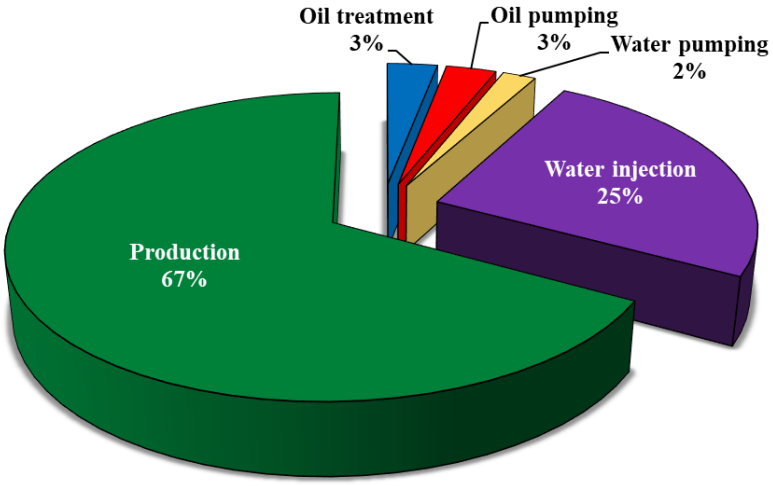

Figure 2. The structure of electricity costs for the whole complex of technological processes of oil production

According to statistical studies, a large part of the structure of electricity costs is spent on oil production (Figure 2). These costs are specific for each operated field, and are mainly determined by the dynamic level of wells producing oil and the structure of the pumping equipment fleet being operated.

Solution of the problem

The main energy in the electrical supply systems of the pumping units is consumed in the engine of the transmission mechanism. Asynchronous motors with a short-circuited rotor with a high starting torque with a maximum voltage of 380V, a power of 1.5...55 kW are used in the transmission of the sucker-rod pumps [22]. The synchronous rotation frequency of the electric motors used in the transmissions of these looms is 500, 750, 1000 and 1500 min^{-1}, the ratio of the starting torque to the nominal torque $M_i / M_n = 1.8...1.9$ and the ratio of the maximum torque to the nominal torque $M_{\max} / M_n = 2.1...2.8$ are within the limit.

Asynchronous motors work with a small operating rate. Because the required starting torque of the electric motor of the looms is 5...6 times higher than the torque in the fixed mode. Engine loading does not exceed 40%. Usually, these engines have small power factor $cos\varphi$ and efficiency.

The value of the power coefficient ($cos\varphi$) for asynchronous motors is 0.55...0.64, and it depends on both the shape coefficient of the load curve K_f and the power of the motor.

The operating mode of electric motors is long-term under a cyclically changing load. Therefore, to determine the power of an electric motor, it is enough to study one of its working cycles. In this case, one of the methods of equivalent torque, equivalent power, or equivalent current is used.

The equivalent or effective power P_e of the electric motor is determined by the following expression

$$P_{eff} = \sqrt{\frac{P_1^2 t_1 + P_2^2 t_2 + ... + P_n^2 t_n}{t_1 + t_2 + ... + t_n}} \quad (1)$$

where t_1, t_2 – interval times; P_1, P_2 - is the average value of the power in the interval.

According to the expression proposed by B.M. Plyush, the effective power is determined by the following expression

$$P_{eff} = \left(k_1 + k_2 G_{liquid} S\right) \frac{n}{\eta_{mex}} \quad (2)$$

where G_{liquid} - is the weight of the liquid column on the plunger; S - travel of the rods suspension point; n - the number of swings per minute of the rods suspension point; η_{mex} - efficiency factor of the transmission mechanism of the sucker-rod pumping unit; k_1 - is a constructive coefficient, depends on the type of pumping unit; k_2 -is the calculation coefficient.

The effective power of the engine is also determined by another expression:

$$P_{eff} = 1{,}7 \cdot k_0 \cdot k_a \cdot d^2 \cdot H \cdot S \cdot n \cdot 10^{-7} + P_s \quad (3)$$

where k_0 - the relative form factor of the torque loading curve on the motor shaft; $k_0 = \frac{k_f}{1{,}11}$; k_a - the correction factor that takes into account the deformation of rods and pipes; H - pump-setting depth; P_S - constant losses on the pumping unit.

Calculating the losses in the electric motor of the pumping unit is complicated because the load changes periodically in each oscillation cycle. Therefore, within this cycle, all the parameters of the electric motor, as well as the efficiency factor and the power factor, change. The graph of the change of the active power consumed by the electric motor during one cycle is shown in figure 3 [23].

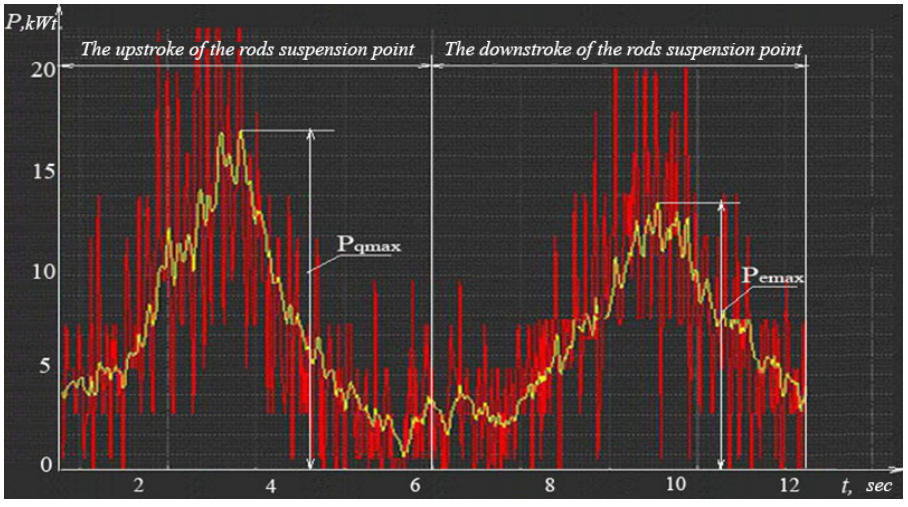

Figure 3. The graph of the change of the active power consumed by the electric motor of the pumping unit during one cycle

Even in ideally balanced pumping unit, the engine load schedule is uneven. For this reason, both efficiency factor and $cos\varphi$ of the asynchronous motor decrease in the direction opposite to the value corresponding to the constant load. At this time, the engine's efficiency factor drops below the nominal value even when the nominal and mean square powers (P_n and P_{kv}) are equal.

When the engine works under a periodically changing load, its efficiency factor and power factor depend on the shape coefficient K_f of the loading curve. If the balancing of the pumping unit is not enough, then the shape factor of the load curve K_f increases, which causes an additional decrease in the engine efficiency. Incomplete loading of the engine due to heating, i.e., the case of $P_{kv} < P_n$, further reduces its energetic characteristics.

According to the load characteristics of the given electric motor, the equivalent powers efficiency factor η_e and power coefficient $cos\varphi_e$ are determined. Then, based on these, the cyclic values of these coefficients are determined depending on the shape factor K_f of the loading curve.

The useful work coefficient of the electric motor of the transfer of the pumping unit in variable cyclic loading is determined by the following expression:

$$\eta_{md} = \frac{\eta_{en}}{\eta_{en} + (1-\eta_{en})K_f} \tag{4}$$

there η_{en} - Energy conversion efficiency, corresponding to the mean square electric power of the engine; is the shape factor of the loading curve.

The shape factor K_f of the loading curve is equal to the ratio of the mean square power P_{msq} to the mean power P_m during one cycle

$$K_f = \frac{P_{msq}}{P_m} = \frac{\sqrt{\frac{1}{T}\int_0^T P^2 dt}}{\frac{1}{T}\int_0^T P dt} \tag{5}$$

where *P* - is the power generated by the engine during time *t*; *T* - is the time of change of the load in one cycle, or the time of one complete cycle of the elbow of the pendulum machine.

If the balancing of the sucker-rod pumps is insufficient $K_f \geq 4$ and if it is underloaded $(K_{load} \leq 0.3)$ it causes a sharp increase in the loss of electrical energy. Therefore, one of the important issues during the operation of the sucker-rod pumping unit is to ensure the balancing of the engine load schedule and the correct selection of its power.

The graphs of the change of the energy conversion efficiency (η) and the power factor $(cos\varphi)$ on the motor shaft are called the operating characteristics of the pumping unit engine. The average values of the parameters during a cycle are called cyclic energy conversion efficiency (η_{ts}) and cyclic power factor $cos\varphi_{ts}$.

The operating power factor in cyclic loading is determined by the following expression:

$$\cos\varphi_{ts} = \cos\varphi_{en}\left(\frac{\eta_{en}}{K_f} - \eta_{en} + 1\right) \tag{6}$$

where $\cos\varphi_{en}$ - is the coefficient corresponding to the root mean square power at constant loading.

When switching from a balanced sucker-rod pumping unit to an unbalanced when the engine is fully utilized due to heat, the energy conversion efficiency decreases from 0.834 to 0.65 and $\cos\varphi_{ts}$ decreases from 0.605 to 0.312. In this case, power losses increase sharply not only in transmissions, but also in energy distribution networks. If the engine is not fully loaded or is not selected correctly, then these energy coefficients decrease even more.

The selection of engine power is performed according to the worst conditions, i.e. the cyclic mode of operation of an unbalanced pumping unit. For this case, the shape coefficient of the loading graph corresponds to $K_f = 3.94$.

Despite this, it can be said that in almost all oil fields, the power of asynchronous motors is greatly exaggerated, which causes additional losses.

The power consumed by the electric motor, that is, the power of the mechanical transmission of the rod well pump as a whole, depends on the efficiency factor in cyclic loading:

$$P_{\Sigma} = \frac{P_{eff}}{\eta_{ts}} \tag{7}$$

The efficiency factor of the electric motor of the transfer of the sucker-rod pumping unit in variable cyclic loading is determined by the following expression:

$$\eta_{ts} = \frac{P_m}{P_m + \Delta P} \tag{8}$$

where P_m - the mean power on the engine shaft during one cycle during; ΔP - is the average value of power loss in the engine during one cycle.

As mentioned, the energy efficiency of the electrical transmission is evaluated by its main characteristics, the energy efficiency and the power factor. However, the expressions proposed for their calculation are true when the work process does not change depending on time.

If the load changes significantly depending on time t, then the concepts of energy loss estimation in time period t should be used:

$$A = \int_0^t P(t)dt \tag{9}$$

and

$$\Delta A = \int_0^t \Delta P(t)dt \tag{10}$$

Cyclic energy efficiency is used as the main energy indicator during the cyclic operation of the mechanical transmission of the rod well pump in the time period t_{ts}

$$\eta_{ts} = \frac{A_{ts}}{A_{ts} + \Delta A_{ts}} = \frac{\int_0^{t_{ts}} P(t)dt}{\int_0^{t_{ts}} P(t)dt + \int_0^{t_{ts}} \Delta P(t)dt} \tag{11}$$

there A_{ts} and ΔA_{ts} are the usable power and power loss during one cycle, respectively.

Cyclic power factor

$$\cos\varphi_{ts} = \frac{A_{ak}}{A_{tot}} = \frac{\int_0^{t_{ts}} P_{ak}(t)dt}{\int_0^{t_{ts}} P_{tot}(t)dt} \tag{12}$$

there A_{ak} and A_{tot} - active and total energy spent during one cycle; P_{ak} and P_{tot} are the active and total power consumed during one cycle.

The power consumed by the engine of the pumping unit consists of the good work spent on lifting the liquid and the work spent on overcoming the power losses in the equipment.

The power consumed by the device during calculation with the specified method is determined by the following expression

$$P_M = P_{XG} + \Delta P_{KL} + \Delta P_{SM} + \Delta P_{SH} + \Delta P_{SNS} + \Delta P_{MD} + \Delta P_{RED} + \Delta P_{BL} + \Delta P_{EM} + \Delta P_{IS} \tag{13}$$

there P_{XG} - the usable power used to lift the liquid from the well; ΔP_{KL} - power loss in pump valves; ΔP_{SM} - power used to overcome mechanical friction on the rods; ΔP_{SH} - the power used to overcome the hydrodynamic friction on the rods; ΔP_{SNS} - the force used to overcome the friction of the plunger in the cylinder of the pump; ΔP_{MD} - power loss in the elements of the sucker-rod pumping unit; ΔP_{RED} - power loss in the reducer; ΔP_{BL} - power loss in belt transmission; ΔP_{EM} - power loss in the electric motor; ΔP_{IS} - is the power loss in the control system.

However, it is difficult to use the refined method in practice. Because it is necessary to know many parameters about the work of the pump suspended in the well, which cannot be measured and can only be calculated with certain errors and assumptions.

As we mentioned, the engines of the sucker-rod pumps work in a very complex variable mode. Power selection for variable loads is more complicated than power selection for steady operation. In addition, sucker-rod pumps differ from other mechanisms in that each type of pump requires not one, but several engines, which differ from each other based on the price of power, and in some cases, even the frequency of rotation. This is explained by the fact that each sucker-rod pumping unit has its own field of application.

The power of the motor that drives the well pump unit depends on many factors, first of all the good work done to lift the fluid from the formations per unit time.

This work can be defined simply as follows:

during the upward movement of the rods column

$$A_{up} = (G_{rod} + G_{liquid})S \tag{13}$$

during the downward movement of the rods column

$$A_{down} = -G_{rod}S \tag{14}$$

effective work (useful work) on the double movemen

$$A = A_{up} + A_{down} = (G_{rod} + G_{liquid})S - G_{rod}S = G_{liquid}S \tag{15}$$

The weight of the liquid column on the plunger of a well pump is proportional to the area of its plunger (the square of its diameter). Therefore, the power used to lift the liquid will be as follows

$$N = Hd^2nS \tag{16}$$

If both the efficiency factor of the device (η_Σ) and the coefficient (η_{en}), which takes into account the load characteristic of the electric motor, are known, then its power can be accurately determined in the following way

$$N_{or} = \frac{1}{\eta_\Sigma \eta_{en}} Hd^2 nS \tag{17}$$

The quantity $Hd^2 nS$ actually represents the hydraulic or positive force, i.e. the lifting of a liquid of volume *Q* to a height *H*.

The useful load can be defined by the following expression

$$N_{us} = 0{,}114 \cdot 10^{-3} QH \tag{18}$$

where *Q* - flowrate of well, m^3/day ; *H* - is the lifting height of the liquid, m .

When choosing an electric motor based on the maximum value of the tangential force, it will work in the half-load mode at small values of the efficiency factor and the power factor $(cos\varphi)$. The operating experience of lathes shows that if the electric motor is selected based on the average value of the tangential force, then the motor will overheat. Because it will be overloaded most of the time. During the incomplete charging period, it will not have time to cool down enough. Currently, various methods and expressions are used to determine the required power of the motor of the pumping units.

In order to rationally use the power of the engine and to create a normal thermal regime for it, the engine is usually selected based on the mean square tangential force:

$$N_{kv} = \frac{\omega r}{\eta} T_{kv} \tag{19}$$

where ω - is the angular velocity of the elbow; r - elbow radius; η - efficiency factor of the depth pump; T_{kv} - is the root mean square tangential force.

The operating experience of sucker-rod pumping units shows that the determination of engine power by the expression (20) is convenient for wells with a relatively small depth. D.V. Efremov's expression can be used to determine the power of the engine for wells with a large depth

$$N = 0{,}0409 \cdot \pi \cdot D_{pl}^2 \cdot S \cdot n \cdot \rho \cdot g \cdot H \cdot \left(\frac{1 - \eta_n \cdot \eta_{md}}{\eta_n \cdot \eta_{md}} + \eta_0 \right) \cdot k \tag{20}$$

Where D_{pl} - diameter of the plunger; S - travel of the rods suspension point; *n* - the number of departures; ρ - the density of the extracted liquid; H - liquid lifting height; η_n - efficiency factor of the depth pump; η_{md} - efficiency factor of the pumping unit; η_0 - pump efficiency; k - is a coefficient that takes into account the degree of balancing of the sucker-rod pumping unit.

In connection with the application of electric motors with a rotation frequency of 1500 min^{-1} in oil fields, an empirical statement was proposed to determine the required power of the electric motor for the transfer of pumping unit:

$$N = \left[\frac{0{,}02 n d_n^2 S}{(k - \varphi)\sqrt[3]{0{,}3 + \eta_0}} + \frac{0{,}1Q}{0{,}5 + \eta_0} \right] H \cdot \psi \tag{21}$$

where n - the number of movements of the balancer per minute; d_n - pump diameter; η_0 - pump efficiency; *k* - coefficient that takes into account the type of pumping unit; φ - the length function of

the rods column; Q - flowrate of well, m^3/day; H - liquid lifting height; ψ - is the nominal shift function of the selected electric motor.

If we accept the combined balancing method of the new pumping unit that we have studied, then the work done during one cycle, taking into account the efficiency factor of the balancing device:

during the upward movement of the rods column

$$A_{up} = \left(G_{rod} + G_{liquid}\right)\cdot S_g - G_{cw}\cdot S_{cw}\cdot \eta_{bl} - G_r \cdot S_r \tag{22}$$

during the downward movement of the rods column

$$A_{down} = -G_{rod}\cdot S_g + \frac{G_{ey}}{\eta_{bl}}\cdot S_{cw} + G_r \cdot S_r \tag{24}$$

Since the electric motor operates in a fixed operating mode and in the nominal sliding range, its average power can be determined as the ratio of the work done by the motor to time. Then, taking into account the efficiency factor of engine, we can determine the forces expended during the up and down movement of the rods suspension point as follows

$$\left.\begin{aligned} N_{up} &= \frac{\left(G_{rod} + G_{liquid}\right)\cdot \eta_{en}\cdot S_g - G_{cw}\cdot S_{cw}\cdot \eta_{bl} - G_r \cdot S_r}{\eta_{en}\cdot t_{up}} \\ N_{down} &= \frac{-G_{rod}\cdot S_g + \dfrac{G_{cw}}{\eta_{bl}} + G_r \cdot S_r}{\eta_{en}\cdot t_{down}} \end{aligned}\right\} \tag{25}$$

In order to determine the power of the electric motor of the balanced pumping unit $\left(N_{up} = N_{down}\right)$, let us add the right and left sides of the expression (25), then

$$N\cdot \eta_{en}\cdot\left(t_{up} + t_{down}\right) = \left(G_{rod} + G_{liquid}\right)\eta_{en}\cdot S_g + G_{rod}\cdot S_g - G_{cw}\cdot S_{ey}\left(\eta_{bl} + \frac{1}{\eta_{bl}}\right) - 2G_r S_r$$

Taking into account that $T = t_{up} + t_{down}$ and efficiency factor, after a series of simplifications, we can determine the required power of the electric motor of the transmission with the following expression

$$N = \frac{1}{\eta_{mex}\cdot\eta_{en}\cdot T}\left[\left(G_{rod} + G_{liquid}\right)\eta_{en} S_g + G_{rod} S_g - G_{cw} S_{cw}\left(\eta_{bl} + \frac{1}{\eta_{bl}}\right) - 2G_r S_r\right] \tag{26}$$

When we use balancing with a movable counterweight according to the proposed expression

$$N = \frac{1}{\eta_{mex}\cdot\eta_{en}\cdot T}\left[\left(G_{rod} + G_{liquid}\right)\eta_{en} S_g + G_{rod} S_g - G_{cw} S_{cw}\left(\eta_{bl} + \frac{1}{\eta_{bl}}\right)\right] \tag{27}$$

And during balancing with rotary counterweight, it will be as follows

$$N = \frac{1}{\eta_{mex}\cdot\eta_{en}\cdot T}\left[\left(G_{rod} + G_{liquid}\right)\eta_{en} S_g + G_{rod} S_g - 2G_r S_r\right] \tag{28}$$

where the S_g - travel of the suspension point of the bar; S_{cw} - travel of the movable counterweight; S_r travel of the rotor counterweight travel; η_{bl} - efficiency factor balancing device; η_{mex} - is the efficiency factor of the transmission mechanism of the pumping unit.

Results and conclusions.

As a result of the research carried out in the article, the following main conclusions and recommendations can be highlighted:

- one of the main shortcomings of mechanical transmissions of rod well pumps currently used in oil production is related to their high energy efficiency, and the main solutions to the problem is the design of new energy-saving beamless pumping units.

- the value of the equivalent or effective power of the motor of the pumping units depends on the influence of many factors, and even in an ideally balanced device, it is impossible to completely equalize the change in the power consumed by the electric motor during such a cycle.

- when switching from a balanced sucker-rod pumping unit to an unbalanced when the engine is fully utilized due to heat, the efficiency factor decreases from 0.834 to 0.65 and $cos\varphi_{ts}$ decreases from 0.605 to 0.312. In this case, power losses increase sharply not only in transmissions, but also in energy distribution networks. If the engine is not fully loaded or is not selected correctly, then these energy coefficients decrease even more. The selection of engine power is performed according to the worst conditions, i.e. the cyclic mode of operation of an unbalanced pumping unit. For this case, the shape coefficient of the loading graph corresponds to $K_f = 3.94$. Despite this, it can be said that in almost all oil fields, the power of asynchronous motors is greatly exaggerated, which causes additional losses.

- proposed expressions for determining the optimal power of the electric motor were proposed, taking into account the efficiency factor of the balancing device during the balancing of the proposed new constructive solution of the beamless pumping unit with a combined, movable counter weights and rotary counter weights. This allows to prevent excess energy consumption and reduce energy costs. Which is very important in the era of globalization, when energy prices are rising.

REFERENCES

[1]. Nguyen T. *Sucker Rod Pump.* In: Artificial Lift Methods. Petroleum Engineering. Springer, Cham. 2020. https://doi.org/10.1007/978-3-030-40720-9_5

[2]. Rutácio C., Elias K. *Sucker Rod Pumping: Design, Operation and Maintenance*. Independently Published, 2020, 430.

[3]. Galimullin M.L., Khabibullin M.Y. *Experience with Sucker-Rod Plunger Pumps and the Latest Technology for Repair of such Pumps.* Chem Petrol Eng 55, 896–901. 2020. https://doi.org/10.1007/s10556-020-00710-1

[4]. Stanghelle KU Evaluation of artificial lift methods on the Gyda field. Master's Thesis, University of Stavanger, Stavanger, Norway, 97 p, 2009.

[5]. Alva M, and Anthony A. *Non Conventional Sucker Rod Pumping for Slim Hole Wells.* Paper presented at the SPE Latin American and Caribbean Petroleum Engineering Conference, Buenos Aires, Argentina, 2021. https://doi.org/10.2118/69550-MS

[6]. Zakharov BS. *Special types of sucker-rod pumps.* Chem Petrol Eng 44, 2008, 217–223. https://doi.org/10.1007/s10556-008-9039-1

[7]. Podio A.L., Gomez J., and Mansure A.J. *"Laboratory Instrumented Sucker-Rod Pump."* Paper presented at the SPE Production and Operations Symposium, Oklahoma City, Oklahoma. 2001. https://doi.org/10.2118/67268-MS

[8]. Jinchao Xu,Wei Li, Siyuan Meng. *Kinematic and dynamic simulation analysis of modified conventional beam pumping unit.* Energy, 2022, Volume 15, Issue 15, https://doi.org/10.3390/en15155496

[9]. Sherif F, Abdelaziz K, Enamul H, Hashim N. *A comprehensive review of sucker rod pumps' components, diagnostics, mathematical models, and common failures and mitigations.* Journal of

Petroleum Exploration and Production Technology. 2021, 11, pp. 3815–3839. https://doi.org/10.1007/s13202-021-01270-7
[10]. Abdullaev A.I., Najafov A.M., Ahmedov B.B., Chelebi I.G., Hajiyev A.B., Abdullaev A.A. *Mechanical drive of sucker-rod pumping unit*. Eurasian patent for invention No. 039650. 2022.
[11]. Abdullaev A.I., Najafov A.M., Ahmedov B.B., Chelebi I.G., Abdullaev A.A., Hajiyev A.B. *Mechanical drive of sucker-rod pumping unit.* Azerbaijan Intellectual Property Agency patent for invention No. a2019 0162. 2021
[12]. Ahmedov B, Khalilov I, & Hajiyev A. *Ensuring the operational-technological characteristics of the new design solution of the sucker-rod pumping unit.* Technology Audit and Production Reserves, 2023, 3(1(71), 6–9. https://doi.org/10.15587/2706-5448.2023.284032
[13]. Ahmedov B. *Assessment of dynamic efforts taking into account of inertial and vibrating loads in deaxial pumping units.* J Petrol Explor Prod Technol. 2020, 10, 1401–1409. https://doi.org/10.1007/s13202-020-00836-1
[14]. Ahmedov B.B, Hajiyev A.B., Mustafayev V.S. *Estimation of the equality of the beamless sucker-rod oil pumping unit by the value of the consumption current.* Nafta-Gaz, 2021, 9, 571-578.
[15]. Isachenko I.N., Goldshtein E.I., Nalimov G.L. *Methods for monitoring the balance of a pumping machine based on measuring electrical parameters.* Oil Industry (Neftânoe hozâjstvo), 2002, № 1 pp. 60–61
[16]. Khakimyanov M.I. *Energy intensity in artificial lift of sucker rod pumping units.* Vestnik UGATU (scientific journal of Ufa State Aviation Technical University), vol. 18, no. 2 (63), pp. 54-60, 2014
[17]. Ahmedov B, Khalilov I, Hajiyev A. *Evaluation of the energy efficiency of the new constructive solution of sucker-rod pump (thesis).* 3rd Eurasian Energy and Sustainability Conference, November 24-25 2022, Baku, Azerbaijan Technical University.
[18]. Ivanovskii V.N. *Energy of oil production: the general optimization ways of energy consumption, Inzh. Prakt.*, 2011, no. 6, pp. 18–26.
[19]. Brunman V.E, Vataev A.S, Volkov A.N. et al. *Improving the energy efficiency of borehole pumps.* Russ. Engin. Res. 2017, 37, 579–580. https://doi.org/10.3103/S1068798X17070061
[20]. Brunman VE, Vataev AS, Volkov AN. et al.*Optimizing pump-drive operation to improve the energy-efficiency of oil extraction.* Russ. Engin. Res. 2017, 37, 479–484. https://doi.org/10.3103/S1068798X17060089
[21]. Egorov A.V., Ilyumdzhiev A.S. *Alternative application and modeling of valve electric drive for borehole pump installations.* Proceedings of Gubkin University, 2012, № 2 (267), 32-46
[22]. Ilyinsky N.F. *Electric Drive Basics.* Moscow, Publishing house MEI, 2003.
[23]. Sakaev A.F. *Systems and algorithms for energy-saving control of frequency-regulated electric drives of the sucker-rod pumping unit, Extended Abstract of Cand. Sci.* (Tech.) Dissertation, St. Petersburg: St. Petersburg Mining Univ. 2009.

Received: 16.01.2023
Accepted: 21.09.2023

MACHINE SCIENCE

ISSN: 2227-6912
E-ISSN: 2790-0479

2023, № 2 Pages 40 – 51

TOPOLOGICAL STRUCTURE OPTIMIZATION AND KINEMATIC PERFORMANCE IMPROVEMENT OF 3-RRR PLANAR PARALLEL MANIPULATOR

Ke XU[1,a*], Huiping SHEN[1,b], Jiaming DENG[1,c], Yunyu SHEN[2,d]

[1]School of Mechanical Engineering, Changzhou University, Changzhou, China
[2]Business Administration Department, University of Northeastern, Shenyang, China

E-mail: [a*]*1375928645@qq.com*, [b]*shp65@126.com*, [c]*czdydjm@126.com*, [d]*919304858@qq.com*

http://dx.doi.org/10.61413/GYUB1233

Abstract: The typical 3-RRR planar parallel manipulator with two translations and one rotation has extensive applications such as plane location and motion transfer. But it suffers two disadvantages. One is its analytical direct kinematics is difficult to be got and another is not input-output motion decoupled. This paper focuses on its topological structure optimization and resulting kinematic performance improvementt. First, the coupling degree of this manipulator is calculated being k=1. Second, based on structure coupling-reducing principle, its coupling-reduced manipulator with zero coupling degree is designed, which not only leads to be easy to get its analytic direct kinematic solutions, but also makes input-output motion partially decoupled. Moreover, based on workspace and singularity of this coupling-reduced manipulator, comprehensive comparison of two manipulators before and after coupling-reducing showed that the main performances of structure coupling-reduced manipulator are superior than that of the typical mechanism. The work shows that structure coupling-reducing is effective method for optimization of topology structure.

Keywords: *parallel mechanism, direct kinematics, structure coupling-reducing, performance analysis*

Introduction.

3-RRR planar parallel manipulator has potential value in practical application. It not only can be used in guiding, location and transmission of rigid body, but also can obtain more accurate motion trajectory than general multi-bar linkages do[1].

At present, many scholars have had much more investigation for 3-RRR planar parallel manipulator. In the aspect of the direct kinematics, the number of the maximum direct kinematics of 3-RRR manipulator is 6, which is proved by [2]. Oetomo *et.al* [3] set up three constraint equations and then got one eighth degree polynomial to solution by using the elimination method.

In the way of mechanism's performance investigation, Gosselin[4] conducted the optimization parameter design of 3-RRR manipulator. Wu *et.al* [5] made comparisons on the peculiarities of statics and dynamics between 4-RRR, 3-RRR and 2-RRR. Taking prismatic pair as actuated one, Cha *et.al* [6] measured the range of 3-RRR manipulator's nonsingular paths. Wei *et.al* [7] analyzed 8 kinds topology structure of 3-RRR manipulator, and analyzed this manipulator dexterity by taking conditioning performance of Jacobian matrix as index. The reachable workspace of the symmetric 3-RRR parallel manipulator was analyzed by Li *et.al* [8]. The Dexterous workspace of 3-RRR manipulator was obtained in [9, 10]. Gao *et. al* [11] systematically analyzed the relationship between branched chains' length and the workspace shape of 3-RRR manipulator.

Obviously, current studies on 3-RRR manipulator s focus primarily on workspace, singularity, dexterity and stiffness performance. However, accuracy analysis and design of the manipulator are difficult and motion control is comparatively complex, the reasons of which are that the analytical

solutions for this manipulator are not easy to get its direct kinematics, and further the manipulator does not possess input-output (*I-O*) motion decoupling.

Taking the two reasons stated above as target, this paper design firstly a novel kind of coupling-reduced mechanism(CRM) with low coupling degree, i.e., k=0, and motion-decoupling based on the structure coupling-reducing methodology. Not only are analytical solutions for direct kinematics obtained but also this manipulator has *I-O* decoupling, which accordingly leads to the precision design, motion planning and control of this manipulator be easy. Moreover, the workspace and singularity are analyzed. The work shows that the comprehensive performance of CRM is better than the typical manipulator 3-RRR. Therefore typical 3-RRR planar parallel manipulator could be replaced by the CRM.

3-RRR PM and Its Topological Optimization Design

Typical 3-RRR planar manipulator is shown in Fig. 1. The digitals, from 1 to 7, are denoted as different rods. The moving platform 1, an equilateral triangle, connects with the static platform 0 through three RRR branch chains. The static coordinate system *o-xy* and the moving coordinate system *o'-x'y'* are established on the static platform 0, moving platform 1 respectively.

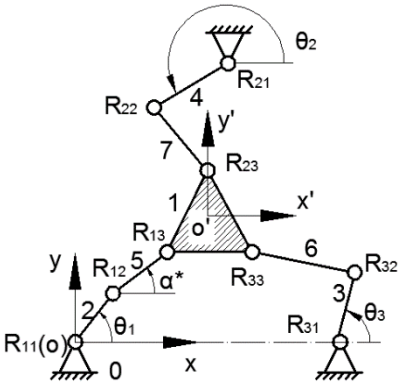

Figure 1. 3-RRR planar parallel mechanism

Length for each link of three branch chains are given as follows, respectively.

$R_{11}R_{12}=l_1$, $R_{12}R_{13}=l_2$, $R_{21}R_{22}=l_7$,

$R_{22}R_{23}=l_6$, $R_{31}R_{32}=l_5$, $R_{32}R_{33}=l_4$.

The side length of moving platform 1 is l_3, its attitude angle γ is anticlockwise direction of x axis to *x*', The input angle of three actuated pairs, R_{11}, R_{21}, R_{31}, is θ_1, θ_2, θ_3 respectively, as shown in the Fig.1.

A. Coupling Degree (κ) of 3-RRR Manipulator

According to the structure composition theory of parallel mechanisms based on the ordered single-open-chain (*SOC*) [12], this mechanism can be decomposed into following two *SOC*s. The restraint degree (Δ) of each SOC is listed as follows, respectively.

$$SOC_1\{-R_{11}-R_{12}-R_{13}-R_{33}-R_{32}-R_{31}-\}$$

$$\Delta_1=\sum_{i=1}^{6}f_i-I_1-\xi_{L_1}=6-2-3=1$$

$$SOC_2\{-R_{21}-R_{22}-R_{23}-\}$$

$$\Delta_2=\sum_{i=1}^{3}f_i-I_2-\xi_{L_2}=3-1-3=-1$$

k of the manipulator is calculated by

$$k = \frac{1}{2}\sum_{j=1}^{2}\left|\Delta_j\right| = \frac{1}{2}(|1|+|-1|) = 1$$

Here,

I_j -- the number of inputs in the j^{th} SOC_j,
f_i -- *DOF* of the i^{th} kinematic pairs,
ξ_{L_j} --the number of independent equations of j^{th},
Δ_j -- constraint degree of j^{th} SOC_j.

Since the coupling degree of this manipulator is k=1, its numerical solutions of direct kinematics could be obtained by solving a one –variable polynomial equation. That is, one virtual variable is needed to be assigned to SOC_1 so that direct kinematic equation containing the variable can be established easily. Then one-dimensional search method is utilized easily to obtain its numerical direct solutions for this manipulator. The calculation is complicated and time-consuming, which is not benefit for real-time controlling. It does not good for the accuracy design of this manipulator as well.

At the same time, since every output parameter (x, y, γ) of moving platform 1 is related to all of three input angles θ_1, θ_2, and θ_3, the manipulator does not possess I-O motion decoupling, which is also undesirable for path planning and motion controlling.

B. Topological Optimization Design of the Structure

In order to improve the two disadvantages stated above, we implement an optimization design for topological structure of this manipulator. Based on the coupling-reducing principle of mechanism topology [13], we combine two arbitrary pairs on the movable platform, such as R_{13} and R_{33} in the Fig. 1, into one multiple joint, and other conditions are not changed, which lead to a modified manipulator shown in the Fig. 2.

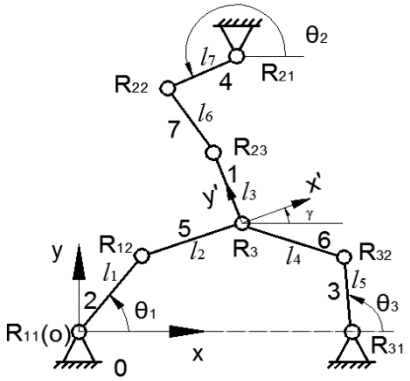

Figure 2. 3-dof coupling-reducing mechanism (CRM)

For the modified manipulator, moving platform 1 has degenerated from three-joint rod to two-joint rod, i.e., R_3R_{23}. Its topological analysis can be decomposed into following:

$$SOC_1\{-R_{11}-R_{12}-R_3-R_{32}-R_{31}-\}$$

$$\Delta_1 = \sum_{i=1}^{5} f_i - I_1 - \xi_{L_1} = 5-2-3 = 0$$

$$SOC_2\{-R_{21}-R_{22}-R_{23}-R_3-\}$$

$$\Delta_2 = \sum_{i=1}^{3} f_i - I_2 - \xi_{L_2} = 4-1-3 = 0$$

Therefore, $k = \frac{1}{2}\sum_{j=1}^{2}|\Delta_j| = \frac{1}{2}(|0|+|0|) = 0$

Kinematic Analysis of CRM

A. Direct Kinematics

The problem of the direct kinematics can be described as: with three known input angles θ_1, θ_2, and θ_3, it is required to solve the attitude angle γ and position (x, y) of revolute joint R_3 of the moving platform 1.

The static coordinate system *o-xy* is shown in Fig. 2, which is the same with it in Fig. 1. The moving coordinate system R_3-*x'y'* are established on R_3, *y'* axis that coincides with the line R_3R_{23}. *x'* axis is perpendicular to this line. The attitude angle γ of the moving platform 1 is taken from forward direction of *x'* axis to *x* as well. The coordinates R_{11}, R_{21}, R_{31} are not changed such that (0,0), (l_9,l_{10}), (l_8,0) , respectively. When input angles θ_1, θ_2 and θ_3 are given, the coordinates of joints R_{12}, R_{22}, and R_{32} are easily got.

- Solve the coordinates of R_3 by using the positions of R_{12} ,R_{32}

Based on $R_{12}R_3=l_2$, $R_{32}R_3=l_4$,

$$\begin{cases}(x_{R_3}-x_{R_{12}})^2+(y_{R_3}-y_{R_{12}})^2=l_2^2\\(x_{R_3}-x_{R_{32}})^2+(y_{R_3}-y_{R_{32}})^2=l_4^2\end{cases}$$

It is obtained

$$\begin{cases}x_{R_3}=\dfrac{-E\pm\sqrt{E^2-4DF}}{2D}\\y_{R_3}=\dfrac{C}{B}-\dfrac{A}{B}x_{R_3}\end{cases} \tag{1}$$

where

$$A=2(l_1\cos\theta_1-l_8-l_5\cos\theta_3),$$
$$B=2(l_1\sin\theta_1-l_5\sin\theta_3),$$
$$C=l_4^2-l_2^2+l_1^2-l_8^2-l_5^2-2l_5l_8\cos\theta_3,$$
$$D=A^2+B^2,$$
$$E=2l_1AB\sin\theta_1-2l_1B^2\cos\theta_1-2AC,$$
$$F=C^2+l_1^2B^2-2l_1BC\sin\theta_1-l_2^2B^2.$$

- Solve the coordinate of R_{23} by using the positions of R_{22}, R_3

Based on $R_{23}R_3=l_3$, $R_{22}R_{23}=l_6$

$$\begin{cases}(x_{R_3}-x_{R_{23}})^2+(y_{R_3}-y_{R_{23}})^2=l_3^2\\(x_{R_{23}}-x_{R_{22}})^2+(y_{R_{23}}-y_{R_{22}})^2=l_6^2\end{cases}$$

We have

$$\begin{cases}x_{R_{23}}=\dfrac{-e\pm\sqrt{e^2-4df}}{2d}\\y_{R_{23}}=\dfrac{c}{b}-\dfrac{a}{b}x_{R_{23}}\end{cases} \tag{2}$$

Here,

$$a = 2(x_{R_3} - l_9 - l_7 \cos\theta_2),$$

$$b = 2(y_{R_3} - l_{10} - l_7 \sin\theta_2),$$

$$c = l_6^2 - l_3^2 + x_{R_3}^2 + y_{R_3}^2 - l_9^2 - l_7^2 - l_{10}^2$$

$$-2l_{10}l_7 \sin\theta_2 - 2l_9 l_7 \cos\theta_2,$$

$$d = a^2 + b^2,$$

$$e = 2y_{R_3}ab - 2x_{R_3}b^2 - 2ac,$$

$$f = c^2 + (x_{R_3}^2 + y_{R_3}^2 - l_3^2)b^2 - 2y_{R_3}bc$$

Then, attitude angle γ is expressed as

$$\tan\gamma = (y_{R_{23}} - y_{R_3}) / (x_{R_{23}} - x_{R_3}) \tag{3}$$

According to Eq.(1), the position of the moving platform 1, i.e., (xR3, yR3), is confirmed by two input angles θ1, θ3. It is also known from Eq. (3) that attitude angle γ is confirmed by three input angles θ1, θ2, and θ3. Therefore, the CRM possess *I-O* partial motion decoupling property. Consequently, it is easier to conduct path planning and motion control of the CRM compared with the typical manipulator.

B. *Inverse Kinematics*

The problem of the inverse kinematics analysis is described as for given attitude angle γ and position (x, y) of joint R_3 of moving platform 1, it is required to solve three input angles θ_1, θ_2, θ_3.

In the moving coordinate system R_3-$x'y'$, the coordinate of R'_{23} is $(0, l_3)$. Through the coordinate system conversion between the static and moving coordinate one, the coordinate of R_3 is

$$\begin{bmatrix} x_{R_{23}} \\ y_{R_{23}} \end{bmatrix} = \begin{bmatrix} \cos\gamma & -\sin\gamma \\ \sin\gamma & \cos\gamma \end{bmatrix} \begin{bmatrix} 0 \\ l_3 \end{bmatrix} + \begin{bmatrix} x \\ y \end{bmatrix} = \begin{bmatrix} -l_3\sin\gamma + x \\ l_3\cos\gamma + y \end{bmatrix}$$

Based on $R_{12}R_3=l_2$, $R_{32}R_3=l_4$, $R_{22}R_{23}=l_6$, three constraint equations can be expressed as

$$(x_{R_{12}} - x_{R_3})^2 + (y_{R_{12}} - y_{R_3})^2 = l_2^2 \tag{4}$$

$$(x_{R_{22}} - x_{R_{23}})^2 + (y_{R_{22}} - y_{R_{23}})^2 = l_6^2 \tag{5}$$

$$(x_{R_{32}} - x_{R_3})^2 + (y_{R_{32}} - y_{R_3})^2 = l_4^2 \tag{6}$$

According to Eqs.(4)~(6), the inverse kinematic for the CRM can be expressed as

$$\theta_i = 2\arctan\frac{A_i \pm \sqrt{A_i^2 + B_i^2 - C_i^2}}{B_i - C_i},\ i=1, 2, 3 \tag{7}$$

Here,

$$A_1 = 2y_{R_3}l_1;\quad B_1 = 2x_{R_3}l_1,$$

$$C_1 = l_2^2 - l_1^2 - x_{R_3}^2 - y_{R_3}^2,$$

$$A_2 = 2y_{R_{23}}l_7 - 2l_{10}l_7,$$

$$B_2 = 2x_{R_{23}}l_7 - 2l_9 l_7,$$

$$C_2 = l_6^2 + 2x_{R_{23}}l_9 + 2y_{R_{23}}l_{10} - l_7^2 - l_9^2 - l_{10}^2 - x_{R_{23}}^2 - y_{R_{23}}^2,$$

$$A_3 = 2y_{R_3}l_5;\quad B_3 = 2x_{R_3}l_5 - 2l_8 l_5,$$

$$C_3 = l_4^2 + 2x_{R_3} l_8 - l_5^2 - l_8^2 - x_{R_3}^2 - y_{R_3}^2 .$$

C. Numerical Examples

As shown in Fig. 2, the structural parameters, based on *Ref.*[4], of the CRM are shown as follows.

$$l_1 = l_5 = l_7 = 400,\ l_8 = 600,\ l_2 = l_3 = l_4 = l_6 = 300,\qquad l_9 = 1054.1,\ l_{10} = 1045.4 \text{ (units: } mm\text{)}.$$

Three input angles θ_1, θ_2, and θ_3 are 60°, 240°, 70°, respectively. The substitution of the known parameters into Eqs.(1)~(3) gives two sets direct kinematics solutions shown in Tab 1.

Tab 1. Direct kinematics of the CRM

	x	y	γ
	4	4	-
	61.1	94.1	104.8544°
	4	4	-
I	61.1	94.1	20.0847°

It is easy to verify the correctness of these direct kinematics solutions by using the inverse kinematic Eq. (7). It is omitted for the limited space.

D. Workspace Analysis

- Reachable workspace

Reachable workspace is reachable area of a moving platform. It is one of main performance indexes to evaluate the kinematic performances of manipulator [8].

The CRM is derived from 3-RRR manipulator by combining two revolute joints R_{13} and R_{33}, and length of other links does not change at all. According to the structural parameters of [10], lengths of the CRM are as follows.

$$l_1 = l_5 = l_7 = 200,\ l_2 = l_4 = l_6 = 200,\ l_3 = 100\sqrt{3},\qquad l_8 = 300,\ l_9 = 150,\ l_{10} = 150\sqrt{3} \text{ (units: } mm\text{)}.$$

Through programming computation on MATLAB, the reachable workspace acreage of 3-RRR typical manipulator is $3.5868\times10^7 mm^2$, and its shape is shown in Fig.3 (*a*).The reachable workspace area of the CRM is $2.6095\times10^7\ mm^2$, and its shape is shown in Fig.3 (*b*).

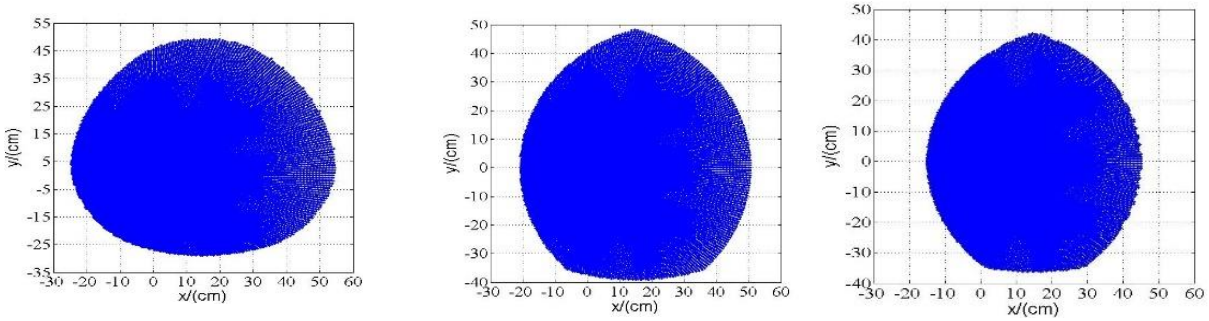

(a) Workspace of 3-RRR manipulator *(b) Workspace of the CRM (c) Workspace of the CRM with modifying a link length*

Figure 3. Reachable Workspace comparison between the CRM and typical mechanism

It is easy from the Fig.3 to find that the area of the CRM is 27.25% less than typical manipulator. However, reachable workspace of the CRM can be improved and became larger by means of increasing some link lengths. For instance, when length of the links 2,3,4,5,6, and 7 are increased to one-sixth of the length of link 1, i.e., $l_3/6$, the area of the CRM will be $3.7948\times10^7 mm^2$, for which the incremental of about 5.52% is made more than that of the typical manipulator. Moreover, the shape has symmetry and succession as well, as shown in Fig.3(*c*).

- Dexterous workspace

If the attitude angle can change arbitrarily in the range of 0° to 360° when the moving platform moves, the motion area of base point is called as dexterous workspace [9, 10].

For the 3-RRR typical manipulator shown in Fig.1, the center of the moving platform 1 is taken as the base point *O'*. If the base point *O'* in the range of dexterous workspace, the moving platform 1 can rotate completely around this base point.

We assume that the moving platform 1 is connected with the frame at the point *O'* using the revolute joint $R_{O'}$, and only one constraint chain *i, for example, i*=1, is considered, one fictitious and subsidiary four-bar linkage $R_{i1}R_{i2}R_{i3}R_{O'}$ is obtained. The length *L* of the frame will change along with the position change of the base point *O'*. But the crank $R_{i3}R_{O'}$ can move completely around the joint $R_{O'}$. The structural parameters of this subsidiary four-bar linkage are given as follows.

$$R_{i1}R_{i2}=L_1,\ R_{i2}R_{i3}=L_2,\ R_{i3}R_{O'}=L_3,\ R_{i1}R_{O'}=L.$$

Based on the crank existence conditions of the four-bar linkage, the range of length *L* can be taken as

$$L=(0,r_1]\cup[r_2,r_3]) \tag{8}$$

Where

$$r_1=L_3-(L_1-L_2),\ r_2=(L_1-L_2)+L_3,\ r_3=(L_1+L_2)-L_3.$$

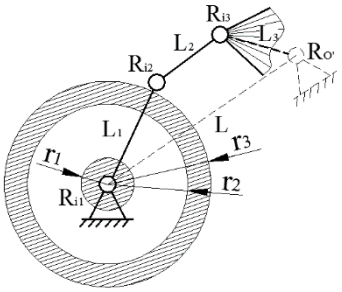

Figure 4. Dexterous workspace in the constraint of branded chain i

If taking R_{i1} as center of a circle and r_1, r_2, r_3 as radius, three circles can be drawn respectively. Then, the base point *O'* locates inside the circle area of between radius r_2 and r_3 or the circle with a radius of r_1, i.e., the shadow area shown in Fig.4, which is denoted by I_i.

When we consider the combined action of three chains I_1, I_2 *and* I_3, dexterous workspace *W* is the intersection workspace that chains I_1, I_2 and I_3 produce together.

For the CRM and its chain 1 and 3, we assign $r_1=r_2=0$, $r_3=400$, and we assign $r_1=r_2=0$, $r_3=300$ for the chain 2.

For 3-RRR manipulator and its three chains, we assign $r_1=r_2=0$, $r_3=300$. Therefore, the dexterous workspaces of the CRM and 3-RRR manipulator are calculated and shown in Fig.5(*a*) and Fig.5(*b*) respectively.

We find that the dexterous workspace area of the CRM and typical mechanism are 8.6567×10^6 mm^2, 6.3429×10^6 mm^2, respectively, and the former is 36.48% bigger than the later

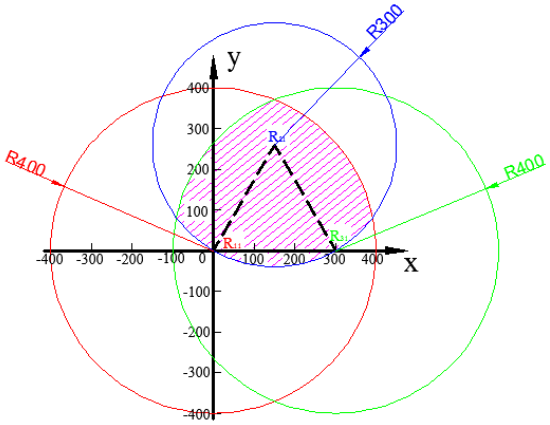

(a) Dexterous workspace of the CRM

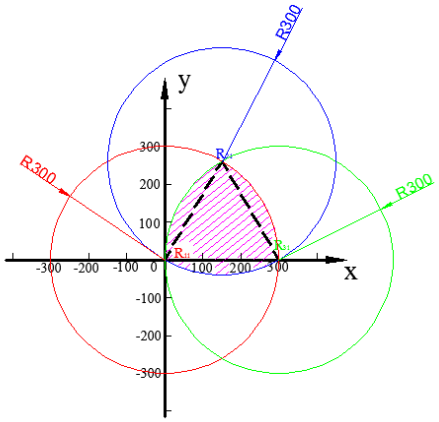

(b) Dexterous workspace of the 3-RRR typical manipulator

Figure 5. Dexterous workspace comparison between the CRM and typical manipulator

E. Singularity Analysis

- Singularity analysis method

If vectors representing all input motions and output motions are denoted by $\boldsymbol{X}$ and $\boldsymbol{Y}$ respectively, the relationship between $\boldsymbol{X}$ and $\boldsymbol{Y}$ can be expressed as following [14].

$$F(\boldsymbol{X},\boldsymbol{Y})=0 \tag{9}$$

By simplifying and rearranging equation （9）, then taking the time derivative of the two sides of the resulting equation, the following equation is obtained.

$$\boldsymbol{J}_p\dot{\boldsymbol{Y}}-\boldsymbol{J}_q\dot{\boldsymbol{X}}=0 \tag{10}$$

Based on whether $\boldsymbol{J}_P$ and $\boldsymbol{J}_q$ matrix are singular, the singular posture of the mechanism could be classified three types as follows

①When $\det(\boldsymbol{J}_q)=0$, input singularity happens.

②When $\det(\boldsymbol{J}_p)=0$, output singularity happens.

③When $\det(\boldsymbol{J}_q)=\det(\boldsymbol{J}_p)=0$, hybrid singularity happens.

- Calculate of $\mathbf{J}_\mathrm{P}$ and $\mathbf{J}_\mathrm{q}$ matrix

By taking the time derivative of the two sides of Eqs. (4)~(6), the following equation is obtained.

$$u_{ii}\dot{\theta}_1 - f_{i1}\dot{x} - f_{i2}\dot{y} - f_{i3}\dot{\gamma} = 0,\ i=1,2,3 \tag{11}$$

Hence, $\boldsymbol{v} = [\dot{x} \quad \dot{y} \quad \dot{\gamma}]^T$ is the output speed of the end effector of the mechanism, while $\boldsymbol{\omega} = [\dot{\theta}_1 \quad \dot{\theta}_2 \quad \dot{\theta}_3]^T$ is actuated joint input angle velocity. The relationship between $\boldsymbol{V}$ and $\boldsymbol{\omega}$ is as:

$$\boldsymbol{J}_p\boldsymbol{V} = \boldsymbol{J}_q\boldsymbol{\omega} \tag{12}$$

Where,

$$\boldsymbol{J}_p = \begin{bmatrix} f_{11} & f_{12} & f_{13} \\ f_{21} & f_{22} & f_{23} \\ f_{31} & f_{32} & f_{33} \end{bmatrix};\quad \boldsymbol{J}_q = \begin{bmatrix} u_{11} & & \\ & u_{22} & \\ & & u_{33} \end{bmatrix};$$

$$u_{11} = l_1(y_{R_{12}} - y_{R_3})\cos\theta_1 - l_1(x_{R_{12}} - x_{R_3})\sin\theta_1,$$
$$u_{22} = l_7(y_{R_{22}} - y_{R_{23}})\cos\theta_2 - l_1(x_{R_{22}} - x_{R_{23}})\sin\theta_2,$$
$$u_{33} = l_5(y_{R_{32}} - y_{R_3})\cos\theta_3 - l_5(x_{R_{32}} - x_{R_3})\sin\theta_3,$$
$$f_{11} = x_{R_{12}} - x_{R_3},\ f_{12} = y_{R_{12}} - y_{R_3},\ f_{13} = 0,$$
$$f_{21} = x_{R_{22}} - x_{R_{23}},\ f_{22} = y_{R_{22}} - y_{R_{23}},$$
$$f_{23} = l_3(x_{R_{23}} - x_{R_{22}})\cos\gamma + l_3(y_{R_{23}} - y_{R_{22}})\sin\gamma,$$
$$f_{31} = x_{R_{32}} - x_{R_3},\ f_{32} = y_{R_{32}} - y_{R_3},\ f_{33} = 0.$$

• Singularity comparison between the CRM and 3-RRR typical mechanism

(1) Input singularity

When the input singularity happens, the movable platform 1 of this mechanism will lose its motion ability along some directions. This moment, at least one motion chain reaches at the boundary of workspace, and we have

$$\det(\boldsymbol{J}_q) = 0$$

The solution set $\boldsymbol{A}$ of this equation is shown below

$$\boldsymbol{A} = \{\boldsymbol{A}_1 \cup \boldsymbol{A}_2 \cup \boldsymbol{A}_3\} \tag{13}$$

Here

$\boldsymbol{A}_1 = \{(y_{R_{12}} - y_{R_3})\cos\theta_1 - (x_{R_{12}} - x_{R_3})\sin\theta_1 = 0\}$, which means that three points R_{11}, R_{12} and R_3 are collinear.

$\boldsymbol{A}_2 = \{(y_{R_{22}} - y_{R_{23}})\cos\theta_2 - (x_{R_{22}} - x_{R_{23}})\sin\theta_2 = 0\}$, which means that three points R_{23}, R_{22} and R_{21} are collinear.

$\boldsymbol{A}_3 = \{(y_{R_{32}} - y_{R_3})\cos\theta_3 - (x_{R_{32}} - x_{R_3})\sin\theta_3 = 0\}$, which means that three points R_{31}, R_{32} and R_3 are collinear.

When three points R_{11}, R_{12} and R_3 are collinear, link 2 and link 5 have combined into one line 2-5. Then, an imaginary four-bar linkage is denoted by link 0, 2-5, 6 and 3, $\theta_3 = f(\theta_1)$, and θ_2 is also independent input angle. The path of joint R_3 on the moving platform 1 is the part arc with a radius of line 2-5. The length of this arc is determined by the two chains 2 and 3.

However, for the 3-RRR typical manipulator when three points R_{11}, R_{12} and R_{13} are collinear, three input angles are independent each other. Moreover, the motion of moving platform 1 is not restrictive when the joint R_{13} is fixed (Fig.1). The base point O' locates inside the circular ring that is determined by the circular radius $l_{2\text{-}5}+R_{13}O'$ and $l_{2\text{-}5}-R_{13}O'$, the upper and lower boundary of this part

annulus are determined by the motion limitation of other two branded chains.

Because of the symmetry, singularity analysis for the case $\boldsymbol{A}_2$ and $\boldsymbol{A}_3$ is similar with that of the above stated.

(2) Output singularity

Under this circumstance, the movable platform 1 still has local motion when all actuated joints are locked. If the movable platform 1 is applied by a limited force, three input links need infinite actuated force to achieve force balance. By this time, we have $\det(\boldsymbol{J}_p)=0$, the solution of the set $\boldsymbol{B}$ for this equation is shown below

$$\boldsymbol{B}=\{\boldsymbol{B}_1 \cup \boldsymbol{B}_2\} \tag{14}$$

Here,

$\boldsymbol{B}_1=\{(x_{R_{23}}-x_{R_{22}})\cos\gamma+(y_{R_{23}}-y_{R_{22}})\sin\gamma=0\}$, which means that three points R_{22}, R_{23} and R_3 are collinear.

$\boldsymbol{B}_2=\{f_{12}f_{31}-f_{11}f_{32}=0\}$, which means that three points R_{12}, R_{32} and R_3 are collinear.

Three kinds of the output singular configurations of the CRM are shown in Eq.(14). When the formula $\boldsymbol{B}_1$ is satisfied three points R_{22}, R_{23} and R_3 are collinear. When taking θ_1, θ_3 as the independent input angles, the angle θ_2, i.e., $\theta_2=f(\theta_1,\theta_3)$, is a dependent input.

However, for 3-RRR typical mechanism, it exists four kinds of singular configurations as follows

① Four joints R_{12}, R_{13}, R_{33} and R_{32} are collinear.
② Four points R_{12}, R_{13}, R_{23} and R_{22} are collinear.
③ Four points R_{22}, R_{23}, R_{33} and R_{32} are collinear.
④ Links 5, 6 and 7 intersect at one point outside the moving platform.

For example, when the first kind of singularity of 3-RRR mechanism happens, i.e., case ①, input θ_1, θ_2 are taken as the independent ones, the angle θ_3 is dependent input such as $\theta_3=f(\theta_1)$.

(3) Synthesis singularity

When $\det(\boldsymbol{J}_q)=\det(\boldsymbol{J}_p)=0$ is satisfied, the input and output singularity will happen at the same time. For instance, if the equations $\boldsymbol{A}_1$ and $\boldsymbol{B}_1$ are satisfied, three points R_{11}, R_{12} and R_3, and another three points R_{22}, R_{23} and R_3 are collinear respectively.

It is clear that from the discussion above, the hybrid singularity analysis of the CRM is simpler than 3-RRR typical manipulator. This conclusion is obtained respectively by a comprehensive comparison of the input and output singularity of the two mechanisms.

Performance Comparison

In a word, the performance comparison of these two mechanisms is shown in Tab 2.

Table 2. Performance comparison of the CRM and 3-RRR typical manipulator

Performance	CRM	3-RRR
k	0	1
Direct kinematics	Analytic	Numerical
I-O decoupling	Yes	No
Reachable workspace	Slightly smaller*	Bigger
Dexterous workspace	Big	Small
Singularity	Simple	Complex

*Note: The size of reachable workspace of CRM could be improved or increased by magnified slightly the length of some links.

By comparing the six aspects such as direct kinematics, coupling degree, decoupling, reachable workspace, dexterous workspace and singularity, it is found that the comprehensive performance of the CRM is superior to that of 3-RRR typical manipulator.

Conclusions

Two disadvantages of the typical 3-RRR planar manipulator could be overcome by its topological structure optimization. It leads to the resulting kinematic performance are improved.

(1) The analytical solutions for the direct kinematics of the CRM can be obtained because of k=0. Its path planning, position control, and input-output motion decoupling properties are simpler.

(2) Based on the inverse kinematics, it can be obtained that the reachable workspace of the CRM is symmetric and continuous. Moreover, the dexterous workspace of it is bigger than typical mechanism's.

(3) Three kinds of singular configurations of this CRM are easier to be got. The singularity analysis of this mechanism is simpler than typical mechanism's.

In summary, the comprehensive kinematic performance of the coupling-reduced mechanism is superior. Structural decoupling-reducing is an effective approach for improving topological structure and its kinematic performances.

Acknowledgements

This research is sponsored by the NSFC (Grant No. 51375062 and No.51475050), Jiangsu Key Development Project (No.BE2015043) and Jiangsu Scientific and Technology Transformation Fund Project (No. BA2015098).

REFERENCES

[1] Z. Huang, L. F. Kong and Y. F. Fang, *Theory and control of parallel robot mechanism.* BeiJing: China Machine Press, 1997:1-34.

[2] C. Gosselin and J. Merlet, *Direct kinematics of planar parallel manipulators: special architectures and number of solutions.* Mechanism and Machine Theory, 1994: 1083-1097.

[3] D. Oetomo, H.C. Liaw, G. Alici and B. Shirinzadeh, *Direct kinematics and analytical solution to 3-RRR parallel planar mechanisms*. International Conference on Control, 2006:1-6.

[4] C.M. Gosselin and J. Angeles, *The optimal kinematic design of a planar three-degree-of-freedom parallel manipulator, Journal of Mechanisms*. Transmissions and Automation in Design, 1988, 110(3):35 -41.

[5] J. Wu, J.S. Wang and Z. You, *A comparision study on the dynamics of plannar 3-DOF 4-DOF,3-RRR and 2-RRR parallel manipulators.* Robotics and Computer-Integrated Manufacturing, 2010, 2011, 27(1): 150-156.

[6] S.-H.Cha, T.A. Lasky and S.A. Velinsky, *Determination of the kinematically redundant active prismatic joint variable ranges of a planar parallel mechanism for singularity-free trajectories.* Mechanism and Machine Theory, 44(2009) 1032-1044.

[7] X. Wei and J. Wu, *Dexterity of 3-RRR planar parallel manipulators.* Machine tool and Hydraulics, 1001-3881 (2009) 10-051-3.

[8] D.H. Li and S.T. Song, *Research of the reachable workspace of symmetrical planar 3-RRR*

*parallel mechanism*Journal of Mechanical Transmission, 1004-2539(2015) 09-0029-03.
[9] J.K. Cui, *On the dexterous workspace of 3-RRR planar parallel manipulator*. University of Shanghai for Science and Technology, 1007-6735(2005)04-0365-04.
[10] Z.H. Lan and M.W. Su, *Analysis of dextrous workspace and cavity of Planar Parallel Manipulator*. Proceedings of the Twelfth National Institute of Institutional Studies, 2000.
[11] F. Gao, X.J. Liu and X. Chen, *The relationships between the shapes of the workspaces and the link lengths of 3-DOF symmetrical planer parallel manipulators*. Mechanism and Machine Theory, 36 (2001)205-220.
[12] T. L Yang, A.X. Liu and Y.F Luo, *Theory and application of robot mechanism topology*. Beijing: Science Press, 2012.
[13] H.P Shen, L.J. Yang, Q.M. Meng and H.B. Yin, *Topological structure coupling-reducing of parallel mechanisms*. The14th IFToMM World Congress, Taipei, Taiwan, October 25-30, 2015.
[14] C. Gosselin and J. Angeles, *Singularity analysis of closed-loop kinematic chain*. IEEE International Conference on Robotics and Automation, Cincinna tiohio: Computer Society Press, 1990, 6(3): 281-290.

Received: 13.02.2023
Accepted: 07.09.2023

MACHINE SCIENCE

ISSN: 2227-6912
E-ISSN: 2790-0479

2023, № 2 Pages 52 – 61

HYBRID DIMENSIONAL SYNTHESIS OF PLANAR MECHANISMS FOR THE COMBINATION OF FINITE POSITIONS AND PATH-POINTS

Mario MÜLLER[1,a*], Esther HÖRTER[1], Mathias HÜSING[1], Burkhard CORVES[1]

[1*] Department of Mechanism Theory and Dynamics of Machines RWTH Aachen University, Aachen, Germany

E-mail: [a*]*mueller@igm.rwth-aachen.de*

http://dx.doi.org/10.61413/XFOH8224

Abstract: The combination of the established synthesis methods for finite positions and path-points leads to a hybrid dimensional synthesis method that is presented within this paper. This hybrid method combines the advantages of the established synthesis methods so that an adjustable definition of a synthesis task as well as a high performance of the algorithm can be ensured. To realize this combination, the established algorithms have to be modified as shown within this paper. Depending on the synthesis task and its degree of freedom, a solution can be found analytically or numerically. Both of these algorithms as well as the algorithm for the calculation of the synthesis degree of freedom is treated in this contribution. The shown approaches are validated by two examples.

Keywords: *Dimensional Synthesis, Planar Mechanisms, Finite Position, Path-Point*

Introduction.

The process of mechanism synthesis can be divided into the two main tasks: structural synthesis and dimensional synthesis [1]. Based on several boundary conditions, the type synthesis process determines the most suitable structure of a mechanism. That includes the determination of the number and kinds of joints and links. The task of the dimensional synthesis is to identify the kinematic parameters of a chosen structure. So, based on a specific motion task or other specifications, the dimension of each link can be determined.

Both, the structural and the dimensional synthesis highly depend on the definition of the synthesis task. A synthesis task of a guidance mechanism can consist of finite positions or path-points [2]. For a linkage that is based only on revolute or prismatic joints the number of finite positions or path-points is limited. Such a four-bar-mechanism for instance can be synthesized with a maximum number of five finite positions. To determine the maximum number of synthesis task elements that can be realized by a specific mechanism, the value of the synthesis task (sDOF) can be calculated by [2]. Mechanisms can fulfill a synthesis task if their value is greater or equals to the value of this task. A four-bar mechanism with four revolute joints can theoretically fulfill up to five finite positions or nine path-points. This number of possible positions or points decreases if specific joint locations are prescribed. Nowadays, dimensional synthesis methods mostly focus on either the specification of finite positions or the definition of path-points. Only few, such as [3], developed a method to combine both specifications. The main disadvantage of the developed algorithm in [3] is, that it does not allow the specification of joint locations. A hybrid dimensional synthesis, that allows the definition of finite positions, path-points as well as the location of joints combines the advantages of both established synthesis methods and allows a more adjustable but still robust way to design mechanisms. Some tasks in application, such as pick and place tasks, only require a limited number of finite positions

[3–5]. For those tasks a hybrid dimensional synthesis gives the possibility to add additional specifications such as joint locations instead of arbitrary angles of a finite position.

Established Dimensional Synthesis Methods. The two most established dimensional synthesis methods are the finite position synthesis based on Burmester [6] and the definition of path-points.

Finite Position Synthesis. In 1888 Burmester published his approach to synthesize four-bar linkages for the maximum number of five precision positions [6]. Ever since, this approach has been modified and used for the dimensional synthesis of dyads and linkages [7–13].

The basic concept of this approach is the determination of the center-point curve and the corresponding circle-point curve based on the relative displacement poles [9]. Figure 1 shows an example of these curves for four finite positions. Every point on the center-point curve k_M belongs to an RR chain that reaches all four positions and hence can be used as a stationary revolute joint of a four-bar mechanism. Every center-point has a corresponding circle-point on the circle-point curve k_{K1} which defines the location of the non-stationary revolute joint of the RR chain.

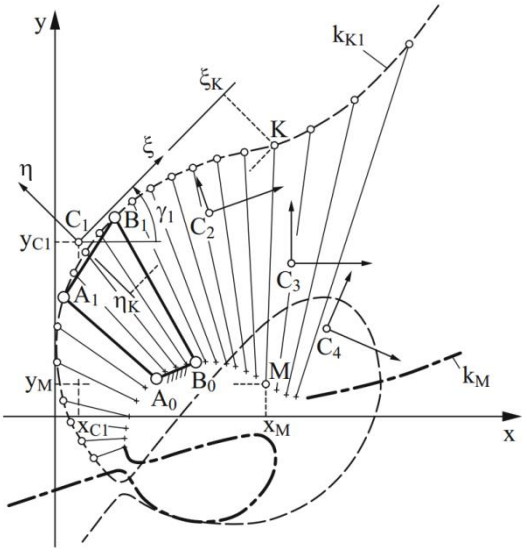

Figure 1: Circle-point curve and center-point curve [2]

To solve the synthesis task for five finite positions algebraically Dittrich, Braune et al. developed in [7; 14] the nonlinear system of equations (1). This system of equation formulates the relation between the coordinates of the center-points (x_M, y_M) and the coordinates of the circle-point (ξ_K, η_K) in relation to the given finite positions. The coefficients A_j - G_j simply depend on these finite positions (2).

$$A_j + B_j\xi_K + C_j\eta_K + D_jx_M + E_jy_M + F_j(x_M\xi_K + y_M\eta_K) + G_j(y_M\xi_K - x_M\eta_K) = 0 j = 1,2,3 \quad (1)$$

$$A_j \dots G_j = f(x_{Ci}, x_{Ci+1}, y_{Ci}, y_{Ci+1}, \gamma_i, \gamma_{i+1}) \quad (2)$$

Since this approach leads to a cubic equation shown in [7], the solving algorithm is performant. The problem of this approach is that the synthesis task has to consist of finite positions. So even if a specific angle γ_i is not desired, it has to be defined to use the algorithm based on the Burmester theorem. That limits the solution space and reduces the number of additional boundary conditions.

Synthesis of Path-Points. The approach of the dimensional synthesis based on the definition of points of a coupler curve provides a relatively adjustable way of synthesis task definition. Here a

four-bar linkage can be synthesized by specifying up to nine points of the coupler curve [11; 15;16]. The unknown locations of the revolute joints can be calculated with the parameters shown in **Ошибка! Источник ссылки не найден.**.

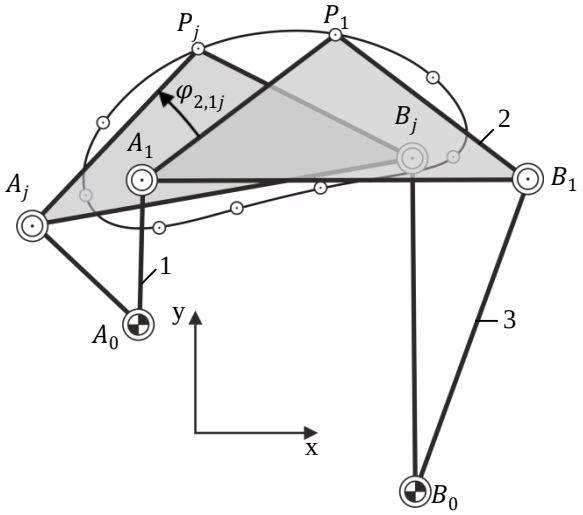

Figure 2: Four-bar mechanism for the path-point synthesis

This approach is based on the motion of joint A respectively joint B in reference to the first path-point P_1 (3).

$$\begin{pmatrix} x_{P,j} - x_{A/B,j} \\ y_{P,j} - y_{A/B,j} \end{pmatrix} = \begin{pmatrix} \cos(\varphi_{2,1j}) & -\sin(\varphi_{2,1j}) \\ \sin(\varphi_{2,1j}) & \cos(\varphi_{2,1j}) \end{pmatrix} \begin{pmatrix} x_{P,1} - x_{A/B,1} \\ y_{P,1} - y_{A/B,1} \end{pmatrix} \text{-} \tag{3}$$

The property that the length of each link does not change can be expressed by equation (4).

$$\left(x_{A/B,j} - x_{A0/B0}\right)^2 + \left(y_{A/B,j} - y_{A0/B0}\right)^2 = \left(x_{A/B,1} - x_{A0/B0}\right)^2 + \left(y_{A/B,1} - y_{A0/B0}\right)^2 \tag{4}$$

The specification of nine path-points leads to eight equations. These eight equations can be used to calculate the eight unknown locations of the revolute joint.

In comparison to the finite positions synthesis the performance and the chance to find a suitable solution is quite bad. The advantage is that the synthesis task and the boundary conditions can be specified adjustably.

Hybrid Dimensional Synthesis. The aim of the hybrid dimensional synthesis is the combination of the advantages of both mentioned approaches to create an adjustable as well as performant synthesis method. Unlike the approach described in [3], the following algorithm allows the specification of joint locations. Furthermore, an analytical synthesis algorithm is shown.

Value of the synthesis task Since this hybrid approach will also have limitations concerning the maximum number of finite positions, points of a coupler curve and joint locations, it is necessary to consider the value of the synthesis task. The approach used here is distinguished from the approach mentioned in [2] to fit the special requirements of the hybrid dimensional synthesis. The used approach will be explained by the synthesis task in Figure 3.

This synthesis task consists of three finite positions (L1 - L3), one point of a coupler curve (P1) and three specifications about the location of the joints (x_{Ao}, y_{Ao}, x_{Bo}). By the definition of at least one finite position or one point of the coupler curve, the remaining synthesis degree of freedom (sDOF) of a four-bar linkage is equal to the number of joints times two.

Since the finite position synthesis based on the Burmester theorem provides a synthesis method for dyads, the algorithm of identifying the sDOF has to check if the synthesis of one dyad is

over-determined. The regulation for the sDOF calculation can be seen in Table 1.

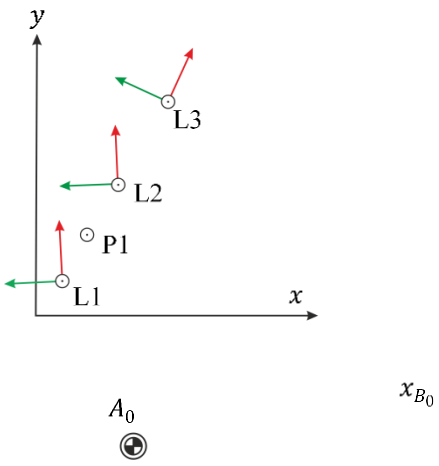

Figure 3: Synthesis task for a four-bar mechanism

A dyad based on two revolute joints ($n_1 = 2$) has the sDOF equals four. Each joint specification such as an x- or y-coordinate reduces the sDOF by one. The specification of the first finite position n_3 does not influence the sDOF since it defines the relative position of the coupler point. Each additional specification of a finite position n_3 reduces the sDOF by one as well.

Table 1: Calculation of the sDOF for a dyad

Dyad		*sDOF*
n_1	No. revolute joints	$+2 \cdot n_1$
n_2	No. Prismatic joints	$+1 \cdot n_2$
(n_3-1)	No. finite positions	$-1 \cdot (n_3-1)$
n_4	No. joint specifications	$-1 \cdot n_4$

The four-bar linkage of the synthesis task shown in Figure 3 consists of the two dyads A_0AC and B_0BC where C represents the coupler point, that has to move through the three finite positions (L1 - L3) and point (P1).

Table 2: sDOF specifications for A_0AC and B_0BC

A_0AC	*sDOF*
$n_1 = 2$	+4
$n_2 = 0$	0
$n_3 = 3$	-2
$n_4 = 2$	-2
Σ	**0**

B_0BC	*sDOF*
$n_1 = 2$	+4
$n_2 = 0$	0
$n_3 = 3$	-2
$n_4 = 1$	-1
Σ	**1**

It can be seen that the final sDOF of dyad A_0AC is equal to zero. There are no additional specifications possible for this dyad. The sDOF of dyad B_0BC is equal to one. The sDOF of the complete four-bar linkage is calculated by the sum of the dyads and so it is equal to one, too. Since the complete mechanism is underdetermined, there is the possibility of one additional specification concerning a desired path-point. So the overall sDOF of the synthesis task in Figure 3 is equal to zero and can be solved exactly.

Table 3 shows the property of a synthesis task related to the sDOF. Overdetermined synthesis tasks cannot be solved exactly. They only can be approximated via an optimization. Underdetermined

synthesis tasks have an infinitive number of possible solutions. They can be optimized concerning different criterions such as installation space, length of linkages, dynamical properties, transmission properties and so forth. This contribution deals with hybrid dimensional synthesis where the sDOF is equals to zero. If the synthesis task is solvable by linkages based on revolute and prismatic joints, there are always a limited number of solutions which exactly fulfill the synthesis task.

Table 3: Properties of the synthesis tasks

sDOF	*Property*
$sDOF < 0$	Overdetermined
$sDOF = 0$	Exact solution possible
$sDOF > 0$	Underdetermined

Algorithm for the synthesis. The algorithm explained within this chapter shows a new approach to synthesize these exact solutions for an sDOF equal to zero. It is necessary to distinguish between two different cases of synthesis tasks, the analytically solvable and the numerically solvable synthesis task.

Case 1: Analytically solvable synthesis task

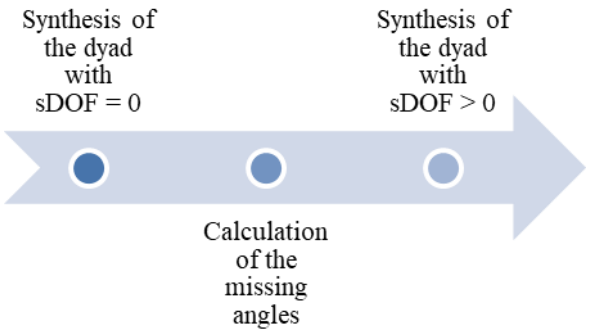

Figure 4: Algorithm for analytically solvable synthesis tasks

The first case is the analytically solvable synthesis task. An algorithmic overview of such a task is given in Figure 4. The specialty of this case is, that the sDOF of one dyad is equal to zero and hence can be synthesized via the finite position synthesis mentioned in chapter 0. The second dyad has to be underdetermined.

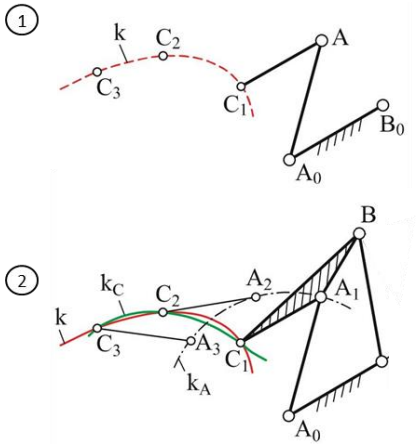

Figure 5: Sketch of the algorithm based on [2]

To synthesize the second dyad the approach displayed in Figure 5 based on [2] can be used.

The coupler point of the synthesized dyad has to be moved in the desired path-points. Therefore it is necessary that the path-point can be reached by the dyad. Thus, the required angles of the coupler link in each point can be determined. These angles are the additional input for the synthesis of the second dyad.

To fulfill one point of the coupler curve C_i there are two possible angles γ_i of the coupler linkage (compare to Figure 6 left).

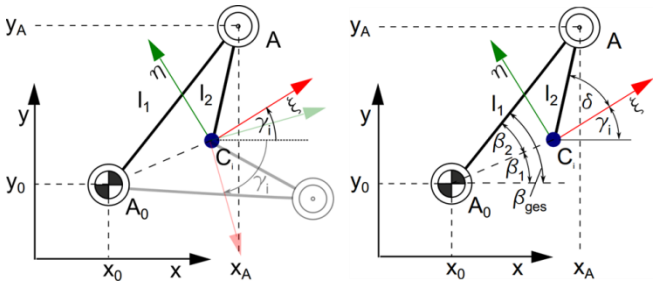

Figure 6: Calculation of the missing angles

The angle γ_i can be calculated in subject to the already synthesized dyad A_0AC. Therefore, the angle δ can be calculated related to the position of the revolute joint A in the η,ξ-coordinate system of the coupler link:

$$\delta = \operatorname{atan2}\left(\frac{\xi_A}{\eta_A}\right) \tag{5}$$

The angles β_1 and β_2 can be calculated via equation (6) and (7) where l_C is the distance between the joint A_0 and the path-point C_i.

$$\beta_1 = \operatorname{atan2}\left(\frac{y_{Ci}-y_0}{x_{Ci}-x_0}\right) \tag{6}$$

$$\beta_2 = \operatorname{acos}\left(\frac{-l_2^2+l_1^2+l_C^2}{2l_2l_C}\right) \tag{7}$$

The angle β_{ges} now can have the two possible solutions (8 to calculate the global coordinates (9) of joint A.

$$\beta_{ges} = \beta_1 \pm \beta_2 \tag{8}$$

$$\begin{pmatrix} x_A \\ y_A \end{pmatrix} = \begin{pmatrix} l_1 \cos(\beta_{ges}) + x_0 \\ l_1 \sin(\beta_{ges}) + y_0 \end{pmatrix} \tag{9}$$

The resulting γ_i can be calculated via equation (10).

$$\gamma_i = \operatorname{atan2}\left(\frac{y_A-y_{Ci}}{x_A-x_{Ci}}\right) - \delta \tag{10}$$

Since now every path-point of the synthesis task has at least one angle γ_i, the sDOF of the second dyad is equal to zero and can be synthesized with the finite position synthesis. This approach uses the same algorithms as the finite position synthesis and so it is as performant as the established approach. Besides, it allows a more adjustable input for the synthesis task.

3.2.2. Case 1: Example of the analytical algorithm

The synthesis task shown in Figure 3 is an example for a analytically solvable motion task. Here the synthesis of dyad A_0AC has the sDOF equal to zero so the finite position synthesis from section 0 can be used. Input for this synthesis is the location of joint A_0 and the three finite positions L1 - L3. With this information the grey dyad in Figure 7 can be synthesized.

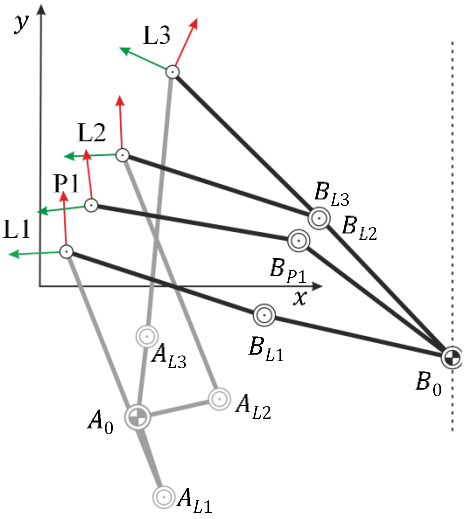

Figure 7: Synthesis of case 1

In the next step the two possible angles γ_i of the coupler link in point P1 can be calculated via equation (5) - (10). Afterwards the next dyad can be synthesized via the input of x_{B0}, the finite positions L1 - L3 as well as the Postion P1 with the calculated angles γ_i. So this dyad is not underdetermined anymore. The black dyad in Figure 7 shows one solution of the synthesis task for the underdetermined dyad.

Since there are two possible angles of the coupler linkage in each point, there is more than one solution for this task. Subsequently it is possible to choose from a set of solutions the best for the given synthesis task. This could be the property that all finite positions and path-points belong to the same coupler curve and thus can be reached without disassembling. This example shows the advantages of the new approach. Instead of the classical synthesis method the hybrid dimensional synthesis ensures that not only three finite positions can be specified for a given location of A_0.

3.2.3 Case 2: Numerically solvable synthesis task

If the sDOFs of both dyads are underdetermined the algorithm explained in chapter 0 is not applicable anymore. Here the recommended approach is still based on the finite position synthesis to fulfill the performance requirements. The difference is that the dyads of the linkage cannot be synthesized separately. So, the four-bar mechanism has to be considered in its entirety. For the specification of a finite position, equation (1) can be solved according to the finite position synthesis explained in section 0.

For the specification of a desired point of a coupler curve, the angle γ_{i+1} is not specified. Since each parameter A_j - G_j is a function of the finite positions (2) this equation system now changes if just a point of a coupler curve (x_{Cj+1}, y_{Cj+1}) is desired. The parameter A_j, D_j and E_j do not depend on the angle γ_{i+1}. All other parameters have to be itemized as shown in equation (11).

$$A_j + D_j x_M + E_j y_M + [x_{Ci}\cos(\gamma_i) + y_{Ci}\sin(\gamma_i) - x_{Ci+1}\cos(\gamma_{i+1}) - y_{Ci+1}\sin(\gamma_{i+1})]\xi_K + [-x_{Ci}\sin(\gamma_i) + y_{Ci}\cos(\gamma_i) + x_{Ci+1}\sin(\gamma_{i+1}) - y_{Ci+1}\cos(\gamma_{i+1})]\eta_K + [-\cos(\gamma_i) + \cos(\gamma_{i+1})](x_M\xi_K + y_M\eta_K) + [-\sin(\gamma_i) + \sin(\gamma_{i+1})](y_M\xi_K - x_M\eta_K) = 0 \quad (11)$$

This equation can be categorized by the terms $\cos(\gamma_{i+1})$ and $\sin(\gamma_{i+1})$ with the unknown angle

γ_{i+1}. This leads to the equation (12) with the coefficients according to equation (13) - (15).

$$a_1 = a_2 \sin(\gamma_{i+1}) + a_3 \cos(\gamma_{i+1}) \tag{12}$$

$$a_1 = -A_j - D_j x_M - E_j y_M - [x_{Ci}\cos(\gamma_i) + y_{Ci}\sin(\gamma_i)]\xi_K - [-x_{Ci}\sin(\gamma_i) + y_{Ci}\cos(\gamma_i)]\eta_K + \cos(\gamma_i)\,(x_M\xi_K + y_M\eta_K) + \sin(\gamma_i)\,(y_M\xi_K - x_M\eta_K) \tag{13}$$

$$a_2 = -y_{Ci+1}\xi_K + x_{Ci+1}\eta_K + \xi_K y_M - \eta_K x_M \tag{14}$$

$$a_3 = -x_{Ci+1}\xi_K - y_{Ci+1}\eta_K + \xi_K x_M + \eta_K y_M \tag{15}$$

Equation (12) has to be formulated for both dyads of the four-bar mechanism and thus leads to a linear equation system (16) with two equations and the two unknowns $\cos(\gamma_{i+1})$ and $\sin(\gamma_{i+1})$. This linear equation system can be solved with Cramer's rule.

$$\begin{pmatrix} a_{2,1} & a_{3,1} \\ a_{2,2} & a_{3,2} \end{pmatrix} \begin{pmatrix} \sin(\gamma_{i+1}) \\ \cos(\gamma_{i+1}) \end{pmatrix} = \begin{pmatrix} a_{1,1} \\ a_{1,2} \end{pmatrix} \tag{16}$$

The combination of the solution of (16) with (17) leads to the final equation (18).

$$\sin^2(\gamma_{i+1}) + \cos^2(\gamma_{i+1}) = 1 \tag{17}$$

$$\left(a_{1,1}a_{3,2} - a_{3,1}a_{1,2}\right)^2 + \left(a_{2,1}a_{1,2} - a_{1,1}a_{2,2}\right)^2 - \left(a_{2,1}a_{3,2} - a_{3,1}a_{2,2}\right)^2 = 0 \tag{18}$$

Each specification of a finite position leads to a total of two equations of type (1) (one for each dyad). Each specification of a path-point leads to one equation of type (18). Since this system of equation is no longer analytically solvable, a numerical optimization method such as a particle swarm algorithm can be used. To increase the performance at this point, the optimization algorithm will use just as many joint locations as is necessary to solve all equations of type (1). The output of this equation system is the input for the objective function (18).

3.2.4Case 2: Example of the numerical algorithm

To show an example of the numerical algorithm the task of Figure 8 should be synthesized.

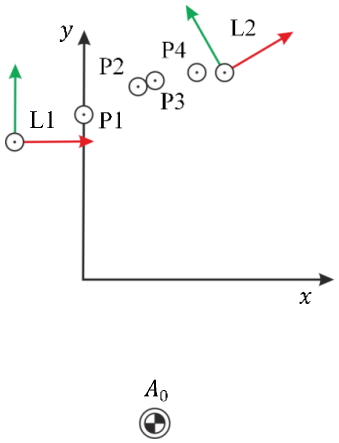

Figure 8: Example for a numerically solvable synthesis task

This synthesis task consists of the definition of both joint co-ordinates of A_0, two finite positions L1 and L2 as well as four desired points of the coupler curve P1 - P4. Analogously to section 0 the sDOF specifications for the two dyads of this synthesis are calculated in Table 4. Each dyad has an

sDOF greater than zero, so no analytical approach is possible. The sum of the sDOF of both dyads is equal to four. That enables the definition of the four desired points of the coupler curve P1 – P4.

For the two finite positions L1 and L2 one equation of type (1) per dyad can be formulated. With the information of joint A_0 the mechanism now has the sDOF of 4. Thus four parameters have to be optimized via an optimization algorithm to fulfill the four equations of type (18). A solution of the synthesis task shown in Figure 4 can be seen in Figure 9.

Table 4: sDOF specifications for A_0AC and B_0BC

A_0AC	*sDOF*
$n_1 = 2$	+4
$n_2 = 0$	0
$n_3 = 2$	-1
$n_4 = 2$	-2
Σ	**1**

B_0BC	*sDOF*
$n_1 = 2$	+4
$n_2 = 0$	0
$n_3 = 2$	-1
$n_4 = 0$	0
Σ	**3**

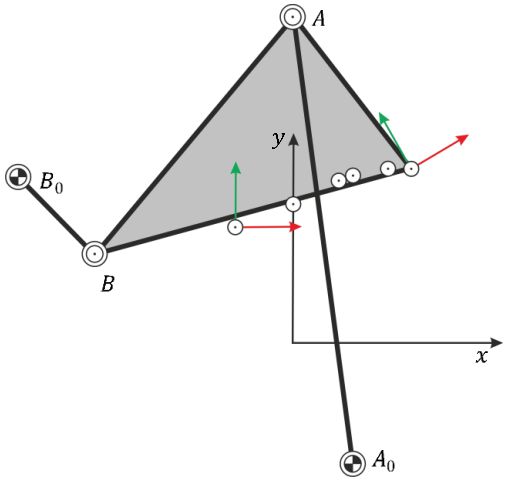

Figure 9: Solution of the numerically solvable synthesis task

The used algorithm ensures that even if no mechanism can fulfill the synthesis task exactly, the algorithm finds an optimal solution that fulfills the finite positions exactly. The given points of the coupler curve then are just approximated as good as possible.

Conclusion.

The shown hybrid dimensional synthesis method combines the advantages of the Burmester theorem for the synthesis of finite positions and the synthesis of path-points. This approach ensures an adjustable way of defining a synthesis task as well as a high performance of the algorithm.

By calculating the value of a synthesis task, the maximal number of finite positions, points of the coupler curve as well as joint locations can be determined. For a synthesis task that includes finite positions it is important to check the synthesis degree of freedom (sDOF) for each dyad so that no dyad is overdetermined and thus can be synthesized.

It is also shown that if one dyad of a four-bar-linkage has an sDOF equal to zero, it is possible to synthesize the mechanism analytically. Therefore the first step is the synthesis of the dyad with the sDOf equal to zero. The coupler point of this dyad now can be moved in the desired points of the coupler curve. By doing so, the possible coupler angles at these points can be calculated. They are the input for the calculation of the other dyads.

If no dyad has an sDOF equal to zero, no analytical synthesis is possible. Then the equation system based on the Burmester theorem can be modified. This modified equation system is the input for a numerical optimization algorithm. This algorithm ensures that an approximated solution can be found if no exact solution of the synthesis task is possible. The so synthesized mechanism fulfills the finite positions exactly.

REFERENCES

[1] Zhao, P.; Ge, X.; Zi, B.; Ge, Q. J., *Planar Linkage Synthesis for Mixed Exact and Approximated Motion Realization Via Kinematic Mapping* Journal of Mechanisms and Robotics, 2016.
[2] Kerle, H.; Corves, B.; Hüsing, M., *Getriebetechnik,* Wiesbaden: Springer Fachmedien Wiesbaden, 5. Auflage, 2015.
[3] Tong, Y.; Myszka, D. H.; Murray, A. P., *Four-Bar Linkage Synthesis for a Combination of Motion and Path-Point Generation* Proceedings of the ASME International Design Engineering Technical Conferences and Computers and Information in Engineering Conference, 2014.
[4] Larochelle, P., *Synthesis of Planar Mechanisms for Pick and Place Tasks with Guiding Positions* Journal of Mechanisms and Robotics, 2015.
[5] Lin, S., *Getriebesynthese nach unscharfen Lagenvorgaben durch Positionierung eines vorbestimmten Getriebes.* Fortschr.-Ber. VDI Reihe 1, Düsseldorf: VDI-Verl., 1999.
[6] Burmester, L., *Lehrbuch der Kinematik,* Leipzig: Verlag von Arthur Felix, 1888.
[7] Braune, R., *Ein Beitrag zur Maßsynthese ebener viergliedriger Kurbelgetriebe,* Diss. RWTH Aachen, Inst. für Getriebetechnik und Maschinendynamik, 1980.
[8] Günzel, D., *Ein Beitrag zur rechnerunterstützten Typ- und Maßsynthese ungleichmässig übersetzender Mechanismen und Getriebe.* Fortschritt-Berichte VDI Reihe 1, Konstruktionstechnik, Maschinenelemente, Düsseldorf: VDI-Verlag, 1994.
[9] McCarthy, J. M.; Soh, G. S., *Geometric design of linkages.* Interdisciplinary applied mathematics, New York: Springer, 2nd ed., 2011.
[10] Pira, B.; Bajraktari, A.; Cunaku, I.; Ymeri, M., *Synthesis of Mechanisms with more than Four Bars using Burmester Theory* Proceedings of the 26th International DAAAM Symposium, 2011, pp. 1043–1044.
[11] Schreiber, H., *Maßsynthese ebener Kurbelgetriebe durch Kreispunktsuche und Homotopieverfahren, :* Lönnies & Schmitz, 1999.
[12] Stolle, G., *Verfahren zur Maßsynthese sechs- und achtgliedriger ebener Gliedführungs- und Übertragungsgetriebe,* Aachen: Shaker Verlag, 2005.
[13] Wohlenberg, P., *Auslegung von Koppelgetrieben mit wiederholtem Durchlauf interaktiv erstellter Bearbeitungsstrategien.* Fortschritt-Berichte / VDI Reihe 1, Konstruktionstechnik, Maschinenelemente, Düsseldorf: VDI-Verlag, 2001.
[14] Dittrich, G.; Braune, R.; Franzke, W., *Algebraische Masssynthese ebener viergliedriger Kurbelgetriebe,* Düsseldorf: VDI, 1983.
[15] Wampler, C. W.; Morgan, A. P.; Sommese, A. J., *Complete Solution of the Nine-Point Path Synthesis Problem for Four-Bar Linkages* Journal of Mechanical Design, pp. 153–159.
[16] Chase, T. R.; Mirth, J. A., *Circuits and Branches of Single-Degree-of-Freedom Planar Linkages* In: Journal of Mechanical Design, 115 (1993) 2, pp. 223–230.

Received: 09.01.2023
Accepted: 27.08.2023

MACHINE SCIENCE

ISSN: 2227-6912
E-ISSN: 2790-0479

2023, №2 Pages 62-69

RELIABILITY ANALYSIS OF THE HOUSING-COVER CONNECTIONS OF PARALLEL-SHAFT REDUCERS

Iftikhar CHALABI

Department of Mechatronics of Azerbaijan Technical University, Baku, Azerbaijan

E-mail: *i_chalabi@aztu.edu.az*

http://dx.doi.org/10.61413/GVAV1993

Abstract: Violation of the density between the housing and the cover of gear reducers can lead to gaps, noise and impacts from gear engagement, an increase in the load on the teeth, and in many cases, to their failure. Therefore, the presented report assessed the reliability of bolted connection connecting the housing and the cover of parallel-shaft reducers according to various failure criteria. It was found that the probability of a violation of the density between the parts is many times higher than the probability of loss of bolt strength.
Keywords: *parallel-shaft reducers, reliability, threaded connections, endurance, joint density*

Introduction.

Gear reducers are one of the main components of modern machines and equipment, and the correct assessment of their reliability, increasing their durability and maintainability are of great importance. Bolted or screw connections connecting the casing and the cover of gear reducers belong to the elements, the risk of failure of which is not too great. The failure of the elements of the connection with the loss of its strength is rare. But deformation of the connecting elements, spontaneous unscrewing of the nut and, as a result, a violation of the tightness between the casing and the cover can lead to disruption of the normal operation of the gearbox as a whole. A violation of the tightness between the casing and the gearbox cover can lead to errors, noise and shocks in the engagement of the wheels, an increase in the load on the gears, and in many cases, to their total failure.

In the presented work, as the main criteria for the functionality of the casing-cover connection of parallel-shaft reducers, the tensile strength condition of the threaded part of the bolt, the condition of tightness between the casing and the cover and the condition of non-slip between the casing and the cover were taken as a basis.

In the existing literature [1 - 5], the calculation of bolted connections that attach the gear housing with its cover is performed mainly by empirical formulas.

In [6] by applying the finite element method to analyse a gear reducer housing, were studied the influence of the retaining bolts tightening force magnitude on the stress state and nodal displacements of the housing, for the specified input parameters.

In [7], the problem of optimizing the gearbox housing using numerical analysis is considered.

In [8-10], the question of increasing the service life of spur gearboxes by activating the non-working flank was considered.

An analysis of the literature on bolted connection connecting the housing and the cover reducers has shown that a comparative analysis of their reliability for various failure criteria has not yet been considered. Such an analysis can be of great practical significance, and therefore, this paper is devoted to this important task.

Determination of bolt loads.

To assess the reliability of the connection, it is necessary to determine the load on the most loaded bolt. Using the example of a single-stage cylindrical gearbox, we will consider the problem of determining the loads on the housing-cover connections. The reactions of the support F_n' and F_n'' arise in the bearing supports of the shaft from the action of the full normal force F_n arising in the parallel-shaft reducer (Fig. 1). These forces are transmitted directly to the bolts connecting the housing and the gearbox cover. We can also divide the force F_n acting on a more loaded bolt into two components. Firstly, the sliding force F_q is transmitted not only to the bolts, but also to the outer ring of the bearing. Therefore, this force does not significantly affect the reliability of the connection. Another component of the F_a is transmitted directly to the bolts and tries to detach the gearbox housing from the cover. The gaping force acting on the most loaded bolt, based on the figure, can be determined as follows:

$$F_b = F_{1a} = \frac{F_a(0{,}5a+e)}{a} = \frac{F_a(a+D\sin\alpha_w)}{2a}. \quad (1)$$

where a - the distance between the bolts; D - outer diameter of the bearing; e - the distance between the axis of the shaft and the line of action of the force F_a; α_w - engagement angle.

For standard gears, $\alpha_w=20^0$ is accepted [2]. Taking $\mu_a=D/a$, we can write expression (1) as follows:

$$F_b = \frac{1}{2}F_a(1+\mu_a \cdot sin\alpha_w). \quad (2)$$

Structurally, it is possible to accept $\mu_a=0{,}65\div0{,}7$ for existing gearboxes of cylindrical gears.

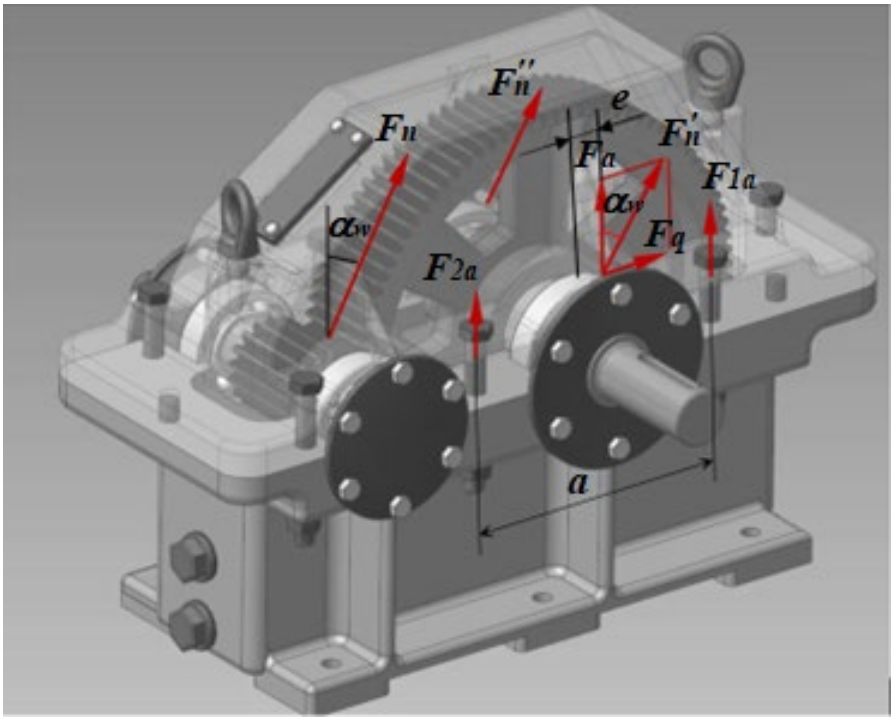

Figure1. Design scheme of the housing-cover connection of a parallel-shaft reducers

Given the equal load on the supports (i.e. $F_n'=F_n''=0.5\ F_n$) in a single-stage cylindrical gearbox and the dependence of the normal force generated by the engagement on the torque transmitted by the driven shaft ($F_n=F_t/\cos\alpha_w=2T_2/d_2\cdot\cos\alpha_w$, [1]), we can determine the force F_a, which tries to break the connection of the housing and cover, as follows:

$$F_a = F_n' \cdot cos\alpha_w = \frac{1}{2} F_n \cdot cos\alpha_w = \frac{F_t}{2} = \frac{T_2}{d_2}.$$

where F_t - circumferential force arising from cylindrical straight-tooth transmission; T_2 - torque on the driven shaft of the gearbox; d_2 - dividing diameter of the driven wheel.

Considering the last expression in the formula (2), we can write:

$$F_b = \frac{T_2}{2d_2}(1 + \mu_a \cdot sin\alpha_w). \quad (3)$$

As can be seen from the last expression, the external dividing force falling on the bolt directly depends on the torque on the driven shaft of the gearbox, inversely proportional to the diameter of the dividing circle of the driven wheel. First, let's consider the issue of assessing reliability by the condition of bolt strength. To ensure the density between the parts of the housing-cover connection of the gearbox, the bolt is tightened by a certain initial tension force F_0, and thus the force $F_и$ is not transferred to the bolt completely (Fig. 2, a). Part of the load is perceived by the deformed housing and the flanges of the cover. In this case, the calculated force acting on the bolt in the direction of its axis should be calculated according to the following formula (Иосилевич Г.Б., 1988):

$$F_h = F_0 + \chi F_b. \quad (4)$$

Where is F_0 - preliminary bolt tightening force; χ - external load factor.

The external load factor takes into account which part of the external force is perceived by the bolt. This coefficient becomes dependent on the geometric dimensions and elastic modulus of the materials of the connected parts and the bolt. Calculations show that when metal elements are connected, it receives values in the range χ=0.2÷0.4 [3].

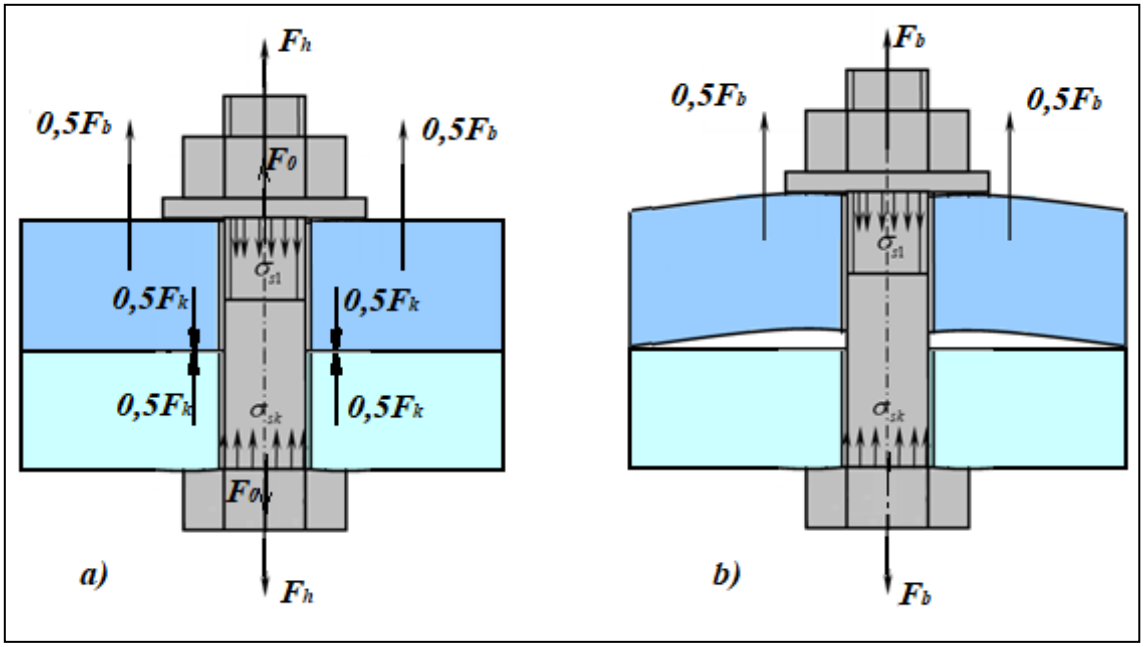

Figure 2. Design scheme of the bolted connection of the parallel-shaft reducers

Reliability analysis.

In practical calculations, it can be assumed that the load and bearing capacity of the connection parts obey the normal distribution (Fig. 3). Then for the case under consideration, the survival probability of the connection according to the condition of bolt strength can be calculated by the following formula [11]:

$$R_b^* = \Phi\left(\frac{\overline{W}_b - \overline{F}_h}{\sqrt{\sigma_{Wb}^2 + \sigma_{Fh}^2}}\right) \quad \text{or} \quad R_b^* = \Phi\left(\frac{\overline{W}_b - \overline{F}_h}{\sqrt{\left(V_{Wb} \cdot \overline{W}_b\right)^2 + \left(V_{Fh} \cdot \overline{F}_h\right)^2}}\right) \tag{5}$$

Where $\overline{W}_b$ - Mathematical expectation of the bearing capacity of the bolt;
$\bar{F}_h$ - Mathematical expectation of the calculated load on the bolt;
σ_{Wb} - Standard deviation of the bearing capacity of the bolt
σ_{Fh} - Standard deviation of the calculated load on the bolt;
V_{Wb} - Coefficient of variation of the bearing capacity of the bolt;
V_{Fh}- Coefficient of variation of the calculated load on the bolt.

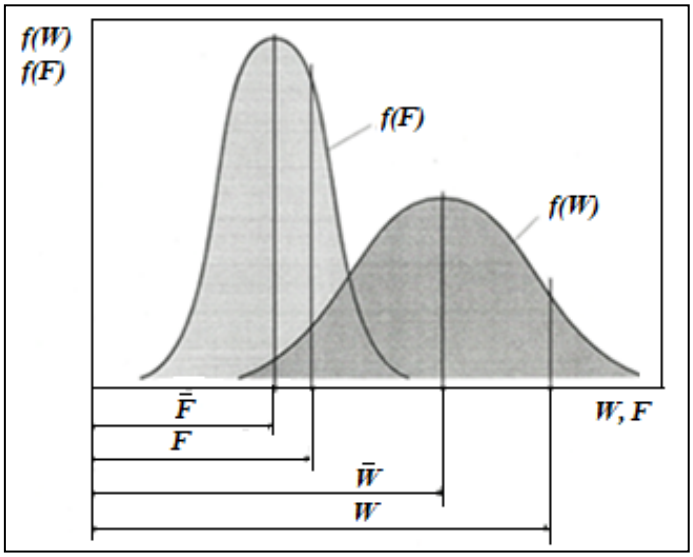

Figure 3. Normal distribution of load values and load-bearing capacity of the elements of the housing-cover connection of gearbox

When the joint is opened for some reason in the housing-cover connection (for example, as a result of an increase in external force or self-unscrewing of the thread), F_0=0 and χ=1 occur, so that the bolt is only under the action of force F_b (Fig. 3, b). In this case, the probability of trouble-free operation of the housing-cover connection of the gearbox according to the condition of bolt strength can be calculated as follows:

$$R_b^{**} = \Phi\left(\frac{\overline{W}_b - \overline{F}_b}{\sqrt{\sigma_{Wb}^2 + \sigma_{Fb}^2}}\right) \quad \text{or} \quad R_b^{**} = \Phi\left(\frac{\overline{W}_b - \overline{F}_b}{\sqrt{\left(V_{Wb} \cdot \overline{W}_b\right)^2 + \left(V_{Fb} \cdot \overline{F}_b\right)^2}}\right). \tag{6}$$

where $\bar{F}_b$ - mathematical expectation of the force acting on the bolt when the density is violated;
σ_{Fb} - Standard deviation of the force acting on the bolt when the density is violated;
V_{Fb}- Coefficient of variation of the force acting on the bolt when the density is violated.

To ensure the condition of density in the housing-cover connection of the gearbox, the residual force arising at the contact of the connected parts must satisfy the condition $F_k=F_0-F_d>0$ [3]. Where

F_d is the part of the force acting on the connection perceived by the details, which can be defined by the following expression:

$$F_d = (1 - \chi)F_b. \tag{7}$$

Thus, in the housing-cover connection, the density condition can be written as $F_0 > F_d$, and the probability that the connection will work without failure in accordance with this condition can be determined by the following expression:

$$R_k = \Phi\left(\frac{\overline{F}_0 - \overline{F}_d}{\sqrt{\sigma_{F0}^2 + \sigma_{Fd}^2}}\right) \quad \text{or} \quad R_k = \Phi\left(\frac{\overline{F}_0 - \overline{F}_d}{\sqrt{\left(V_{F0} \cdot \overline{F}_0\right)^2 + \left(V_{Fd} \cdot \overline{F}_d\right)^2}}\right). \tag{8}$$

Where $\bar{F}_0$ is the mathematical expectation of the preliminary tightening force;
$\bar{F}_d$ is the mathematical expectation of the force perceived by the connected parts;
σ_{F0} is the mean square deviation of the preliminary tightening force;
σ_{Fd} is the mean square deviation of the force perceived by the connected parts;
V_{F0} is the coefficient of variation of the preliminary tightening force;
V_{Fd} is the coefficient of variation of the force perceived by the connected parts.

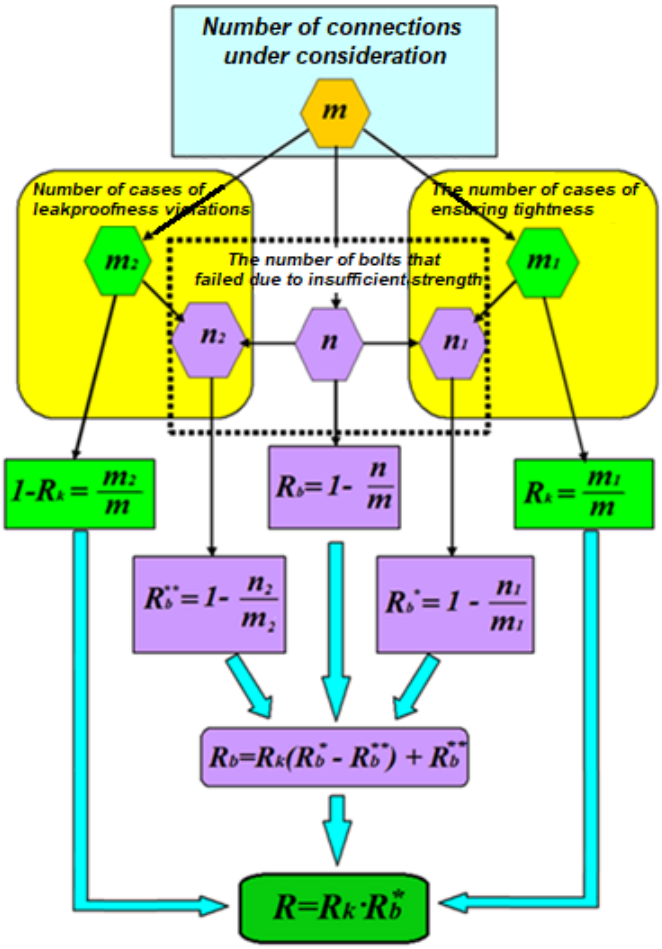

Figure 4. Scheme for the reliability analysis of the connection between the casing and the cover of reducer

Let's use the classical methods of probability theory to determine the ratio between reliability indexes according to various criteria for the survival probability of the housing-cover gearbox connection. Suppose that a test was carried out on the housing-cover connection with the number m, and

after a certain period of operation, the bolt with the number n failed, losing strength. Of these, the bolt n_1 of the number failed, provided there is no breach of tightness, and the bolt n_2 of the number failed as a result of loss of tightness. Suppose that with the number of bolts m as a whole, there was no density violation on the number of bolts m_1, and with the number of bolts m_2, density violations occurred. The probabilities of uptime or failure according to various criteria can be described schematically in accordance with Fig. 4.

The survival probability of the bolt according to the strength condition can be determined by the following expression:

$$R_b = 1 - \frac{n}{m}. \tag{9}$$

Similarly, we can determine the survival probability by the density condition (R_k) and the probability of density violation (P_k) by the following formulas:

$$R_k = \frac{m_1}{m}; \qquad P_k = 1 - R_k = \frac{m_2}{m}. \tag{10}$$

The survival probabilities of the bolt according to the strength condition in cases of absence and presence of density, respectively, can be determined by the following expressions:

$$R_b^* = 1 - \frac{n_1}{m_1}; \qquad R_b^{**} = 1 - \frac{n_2}{m_2}. \tag{11}$$

By solving expressions (9-11) together, we can obtain the following expression to determine the probability that the bolt will work without failure due to the strength condition:

$$R_b = R_k(R_b^* - R_b^{**}) + R_b^{**}. \tag{12}$$

As already mentioned, a breach of tightness in the housing-cover connection of the gear reducer should also be considered as a transmission failure. Because the violation of tightness also leads to the fact that the gearbox loses its function. Given this, the probability that the housing-cover gearbox connection will work according to both criteria without failure can be determined as follows:

$$R = 1 - \frac{n_1+m_2}{m}. \tag{13}$$

Having made some simplifications in the last expression, given expressions (10) and (11), we can write the following expression:

$$R = R_k \cdot R_b^*. \tag{14}$$

An assessment of the reliability of the casing-cover connection of a cylindrical gearbox with a gear ratio u=4, an axial distance a_w=224 mm, a diameter of the division of the bearing wheel d_2=360 mm at the location of the bearings is considered. Standard M12 bolts with a thread pitch of P=1,5 mm and an internal diameter of d_1=10,16 mm were selected for connecting the housing-cover gearbox. Since there were no special requirements for the design, the bolt material was selected steel 20, which corresponds to strength class 4.6. The yield strength of the bolt material was adopted as the bearing capacity. The yield strength of the selected material is assumed to be σ_y=240 N/mm2. Depending on the magnitude and fluctuation of the torque acting on the bearing shaft of the gearbox, as well as on the bearing capacity of the bolt material, the survival probability of the housing-cover connection was calculated.

Since the connection of the housing and the gear reducer cover is designed with a large margin factor according to all failure criteria, it is practically impossible for the connection to fail at rated load. The loss of operability of this connection occurs due to accidental overloads or shocks that occur during operation. Therefore, it is important to assess the reliability of the housing-cover connection depending on the load according to various performance criteria. To this end, on the basis of the methodology described above, an assessment of reliability indicators was carried out according to various criteria for the operability of the connection in question. In these calculations, the coefficient

of variation of the bearing capacity V_{Wb}=0,05, the coefficients of variation of the calculated and external forces acting on the bolt, V_{Fh}=V_{Fb}= 0,07, the coefficients of variation of the initial tightening force and compression forces created on the part, V_{F0}=V_{Fd}=0,1 are adopted. The results are graphically shown in Fig. 5.

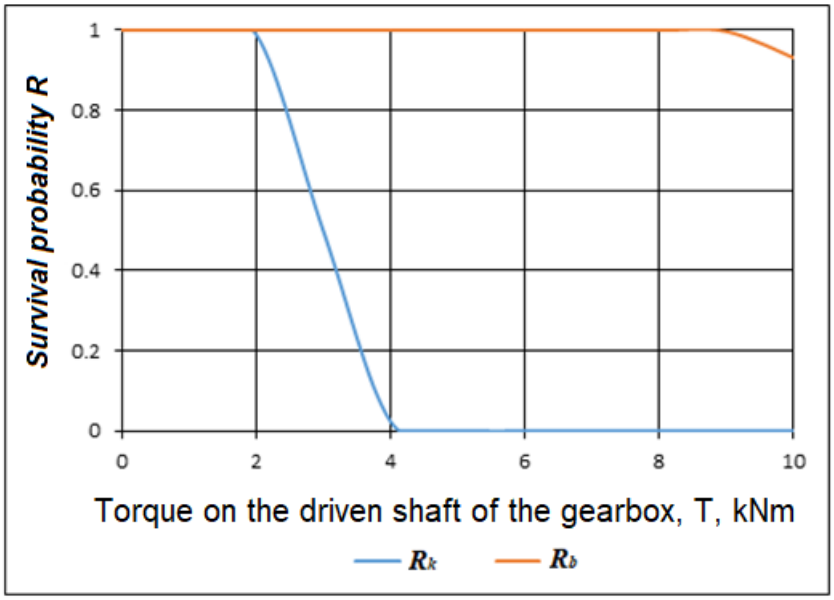

Figure 5. Dependence of the reliability indicators of the housing-cover gearbox connection on the transmitted torque

Conclusions.

As can be seen from the graph in Fig. 5, the reliability of the casing-cover connection of a parallel-shaft reducer is mainly determined by the condition of joint density. Since the bolts are designed with a large margin factor, even with a load many times higher than the nominal one, the indicator of their reliability gets the maximum value. And with a load exceeding the nominal by about two times, the probability of trouble-free operation drops sharply due to the tightness condition. And violation of the tightness condition can lead, as already mentioned above, to the occurrence of gaps in the engagement and shaft supports. This can eventually lead to the appearance of sound and vibration, as well as to increased impacts during engagement. Therefore, it is very important to control the initial tension force created on the bolts in order to increase the tightening in the housing-cover connection.

REFERENCES

[1] Abdullayev A.H., Güməyev M.H., Məmmədov H.S. (2014) *Tətbiqi mexanika*. Dərs vəsaiti. – Bakı: "Təhsil" NPM.

[2] Дунаев П.В., Леликов О.П. (2013*) Детали машин. Курсовое проектирование.* Учебное пособие. – Москва: «Машиностроение».

[3] Иосилевич Г.Б. (1988) *Детали машин.* Учебник. – Москва: «Машиностроение».

[4] Khurmi R.S., Gupta J.K. *Machine Design*. Eurasia Publishing House, Ram Nagar, New Delhi, 2005.

[5] Decker K. –H. *Maschinenelemente: Funktion, Gestaltung und Berechnung Carl Hanser Verlag*, München, Wien, 2018.

[6] Miklos I. Zs., Miklos C. C., Alic C. I., Raţiu S. *Analysis of gear reducer housing using the finite element method. International Conference on Applied Sciences (ICAS2017).* IOP Publishing. Series: Materials Science and Engineering 294 (2017) 012034 doi:10.1088/1757-899X/294/1/012034.

[7] Korka Z.-I., Cojocaru V., Miclosina C.-O. *Modal-based design optimization of a gearbox housing.* RJAV, vol. 16, issue 1/2019.
[8] I. Chalabi, *Comparative Service Life Analysis for Gears According to Different Failure Criteria.* Journal of Failure Analysis Prevention 20. p. 2137-2144 (2020. https://doi.org/10.1007/s11668-020-01029-y
[9] Iftikhar Chalabi, Beyali Ahmedov, Shahin Charkasov, Shahid Yusubov. *Comparative service life analysis for Novikov gears of mechanical drives of sucker-rod pumps.* Journal SOCAR Proceedings. 2022. Special Issue 2. Pp. 53-59. DOI: 10.5510/OGP2022SI200776
[10] Chalabi I., Ahmedov B., Hajiyev A. *Comparative analysis of gears service life of mechanical drive for sucker-rod pumps*//Oil Qas European Magazine. -2021. 47. Edition, Issue 1, p. 39-45.
[11] Tschalabi I., Jäger P. (2005) *Systematische Sicherheits- und Zuverlässigkeitsanalyse für Schraubenverbindungen*//Konstruktion. Nr.1-2, S. 59-64.

Received: 16.03.2023
Accepted: 19.11.2023

MACHINE SCIENCE

ISSN: 2227-6912
E-ISSN: 2790-0479

2023, № 2 Pages 70-77

EFFECT OF GAMMA IRRADIATION ON ELECTRICAL AND PHOTOELECTRICAL PROPERTIES OF $Cd_{1-x}Mn_xTe$ THIN FILMS

Metanet MEHRABOVA[1,a*], Amdulla MEKHRABOV[2,3,b]

[1*] Department Engineering Physics and Electronics, Azerbaijan Technical University, Baku, Azerbaijan
[2]Novel Materials and Nanotechnologies Institute, Azerbaijan Technical University, Baku, Azerbaijan
[3]Faculty of Metallurgy and Materials Science, Department of Metallurgy and Materials Technologies, Azerbaijan Technical University, Baku, Azerbaijan

E-mail: [a]metanet.mehrabova@aztu.edu.az; [b]emdulla.mehrabov@aztu.edu.az*

http://dx.doi.org/10.61413/GDKV8772

Abstract: $A^{II}B^{VI}$ groups of compound semiconductors, their solid solutions, bulk and thin films on their base have wide application possibilities in modern microelectronics. Creation of photosensitive elements and structures on the base of these semiconductors and investigations of their usage potentials in various fields of optoelectronics is one of the most actual problems of modern materials science and engineering. Recently, A^{II}(TM= Mn, Fe, Co, etc)B^{VI} based semimagnetic semiconductors (SMSC) compounds has attracted increasing interest since they considered a promising material for the fabrication of high-performance room-temperature *γ*- and *x*-ray detectors. Such detectors offer great potential for nonproliferation applications, medical imaging, astrophysics research, and monitoring industrial processes, because they are able to operate at ambient temperatures, while providing a high detection efficiency and good energy resolution. The aim of the work is to determine of photosensitivity range of $Cd_{1-x}Mn_xTe$ SMSC thin films, to investigate their sensitivity to γ- irradiation and to study the creation possibility of γ- ray detectors on the base these thin films. In these respect, VAC and photoconductivity, as well as effect of γ- ray irradiation on these properties has been studied. Results of current investigation reveal that, $Cd_{1-x}Mn_xTe$ (x=0.07) epitaxial films of compounds are sensitive to γ-ray irradiation, indicating that these materials can be considered as a good candidate for γ-ray detector applications.

Keywords: *$A^{II}B^{VI}$ compounds, CdMnTe, electrical and photoelectrical properties, γ-ray irradiation*

Introduction.

In undertaking national security and nonproliferation inspections, radiation detectors mainly serve to locate and identify special radioactive nuclear materials. These applications especially demand portable, lightweight radiation detectors with high resolution. For more than four decades, CdTe has been known as a good candidate material for radiation detection. Detectors on the base of CdTe offer high conversion efficiency of photons to electronic charge carriers as compared to scintillators; consequently, for high-quality CdTe detectors, the energy resolution is expected to be considerably better than scintillators [1, 2]. More importantly, CdTe radiation detectors operate at room temperature, thereby obviating the need for a complicated cooling system and, accordingly, affording greatly enlarged application fields. However, a relatively high leakage current has proven to be a limiting factor during the development of large volume CdTe radiation detectors. In addition, CdTe detectors are relatively expensive, because it is difficult to grow large-volume CdTe crystals of acceptable quality, yield and difficult mechanizm of crystal catting [1,2]. On the basis of the utility of CdTe, the CdZnTe (CZT) compounds was explored carefully, because the introduction of Zn increases the band gap and reduces the leakage current (and noise) of radiation detectors [3-7]. It also is less expensive and easier to produce large-volume single crystals with CZT than with CdTe. Since the first practical CZT gamma-ray detector reported in 1992 [8], there have been many advances in

the performance of the devices. The high-resistivity CZT crystals required for radiation detection initially were grown using the high-pressure Bridgman method (HPB). In recent years, other methods were employed, such as the travelling heater method (THM) and the modified Bridgman method (MB). Today, large-volume CZT single crystals up to hundreds of cubic centimeters can be produced due to improvements in the growth techniques [1, 2, 9]. Such progress in bettering the quality of the CZT material for CZT radiation detectors and electron-transport-only device designs, as well as improving the related electronics greatly have enlarged their application fields and accelerated their commercial marketing [1,2].

The International Atomic Energy Agency (IAEA) has used CdTe and CZT detectors for over three decades [10, 11]. Recently, their usage significantly increased, stimulated by the improvement of material properties, their improved availability, and the development of improved detector-specific, low-noise integrated circuits for electronic readouts. Large-volume CZT detectors also are needed in nonproliferation inspections, because they potentially reduce the measurement time significantly. This is especially important in verifying unirradiated nuclear material where count rates are low and typical gamma lines of uranium or plutonium gamma spectra must be resolved. However, the large-volume CdTe/CZT detectors required for these inspections presently are limited by the lack of CZT single crystals whose active volume is more than about 500 mm^3. The dearth of larger volume CdTe/CZT single crystals must be resolved before their widespread application in nonproliferation inspections [1,2]. Recently, scientists at Brookhaven National Laboratory (BNL) developed a hand-held gamma-ray spectrometer for nonproliferation inspections based on virtual Frisch-grid CZT detectors [1,2, 12-16]. The whole system achieves an effective detection volume of 19.2 cm^3, that is, 10 times larger than commercial co-planar grid (CPG) CZT detectors. Consequently, detection efficiency is improved significantly. The system employs an 8x8 virtual Frisch-grid CZT detector array; each detector is 5x5x12 mm^3. By using front-end application-specific integrated circuits (ASICs) developed at BNL, this spectrometer has a small profile and high energy-resolution. Further, its relatively simple configuration greatly lowers the cost. This achievement has allowed to build an inexpensive, large-volume detector array with high energy resolution and high detection efficiency, so affording wide application potentials in national security and nonproliferation inspections. Moreover, the detector modules are scalable to address a larger range of efficiency requirements [2].

The CdMnTe (CMT) SMSC compound is a relatively novel material for radiation detection. CMT is a diluted magnetic compound semiconductor, previously used as Faraday rotators, optical isolators, solar cells, lasers, magnetic field sensors, and infrared detectors [1,2]. In 1999, Burger et al. first investigated the potential application of this material as radiation detector [17]. They proposed that CMT has two main advantages over CZT, namely, better homogeneity and the lower amount of Mn needed to reach the desired band gap, so making it a good competitor to CZT. Most problems with CMT radiation detectors center on the poor quality of the crystals. Until now, it was difficult to obtain CMT single crystals with high resistivity and acceptable carrier transport properties [1,2]. Some recent progress suggests the possibility of a breakthrough in this field, leading to large improvement in the performance of CMT radiation detectors [8-26]. However, several material properties must be improved before CMT can be practically employed for X-ray and gamma-ray detections. First, compared to CZT, the bond ionicity of CMT is higher, entailing a greater tendency for crystallization into a hexagonal structure, but not in the expected zinc-blende structure [8-26]. Also, higher ionicity can generate twins easily in crystals. Second, the resistivity of CMT crystals must be improved. Normally, CMT crystals grown by the Bridgman methods are p-type materials

due to their high concentration of cadmium vacancies (V_{Cd}) the dominant acceptors, and the resistivity of as-grown crystals can be as low as $10–10^3$ Ω cm, thus not satisfying the resistivity requirement of X-ray and gamma-ray radiation detectors. Recently, detector-grade CMT crystals were grown, and the first CMT detector was fabricated $Cd_{0.94}Mn_{0.06}Te$ doped with Vanadium $5x10^{16}cm^{-3}$. However, compared with the performance of CZT detector, there still is much room to improve CMT detectors before they can to be applied as practical radiation detectors. The limited availability of CMT crystals to researchers also inhibits its development as a radiation detector. As a result, they remain at the stage of laboratory development and have not been incorporated practically in commercial detection systems [8-26].

In order to overcome the problems arising in the design and development of X- and gamma-ray detectors on the base of defect-free massive CMT single crystals we are offering, in this present study, fabrication of these detectors on the base of epitaxial thin films of $Cd_{1-x}(TM)_xTe$ SMSC compounds for the first time. The development of molecular beam epitaxy (MBE) in the 1970s for arsenic III-V semiconductors has allowed to produce high-quality epitaxial layers with very abrupt interfaces, good control of thickness, doping, and composition. In recent years small-size semiconductors are successfully applied in microelectronics, spintronic, optoelectronics, integral optics, astrophysics, medicine and other fields. One of these semiconductor materials is $Cd_{1-x}(TM)_xTe$ SMSC thin films which are considered to be very perspective and unique for making of detectors of γ- and x-ray [27-31]. $Cd_{1-x}(TM)_xTe$ SMSC thin films have been studied less in comparison with other semiconductors, therefore obtaining of their perfect samples with high crystal perfection, clean and glossy surface, study of surface morphology and crystal structure and investigate of its application perspectives in device-building is one of the scientific problems and of great importance.

Therefore, the aim of the work is determination of photosensitivity range of $Cd_{1-x}Mn_xTe$ SMSC thin films; investigation the photosensitivity of samples, irradiated by γ- ray; to study creation possibility of γ- ray detectors, operating at room temperature and without scintillation material.

In these respect, VAC and photoconductivity, effect of γ- ray irradiation on these properties, as well as possibilities of fabrication γ-ray detectors on the base of $Cd_{1-x}Mn_xTe$ thin films has been studied.

Material and Methods. The powder of synthesized $Cd_{1-x}Mn_xTe$ solid solutions were used to obtain thin films. The crystal structure of synthesized solid solutions has been studied by *X*-ray diffraction (XRD) method on Bruker D8 Advance XRD. $Cd_{1-x}Mn_xTe$ (x=0.07) SMSC compounds thin films were grown on glass substrates by molecular beam condensation (MBC) technique in the vacuum evaporation equipment УВН-71П-3 with steam-oil pumping and nitrogen trap at working pressure of residual gas $(1÷2)10^{-4}$ Pa. Glass substrates (1×1 cm) were cleaned with acetone, methanol and distilled water. The powder of $Cd_{1-x}Mn_xTe$ solid solutions (purity 99.999%) was used to obtain thin films. The thisckness of the obtained films was controlled with a micro interferometer microscope МИИ-4. The optical spectra were recorded on a UV-Visible SPECORD 210 PLUS spectrophotometer in the wavelength range λ = 190–1100 nm. Samples irradiated by γ-quanta on Co^{60} isotopes with energies E = 1.17MeV and E = 1.33MeV.

Results and discussions. In order to grow $Cd_{1-x}Mn_xTe$ (x=0.07) epitaxial films it has been used synthesized samples of $Cd_{1-x}Mn_xTe$ solid solutions of corresponding compositions. The crystal structure of synthesized solid solutions has been studied by XRD method, Fig. 1. The spectra showed that solid solutions of $Cd_{1-x}Mn_xTe$ crystallize on the zinc-blende type crystal lattice structure of CdTe (cubic, sphalerite) with lattice parameters of a_1=6.4785, a_2=6.4775 and a_3= 6.4745.

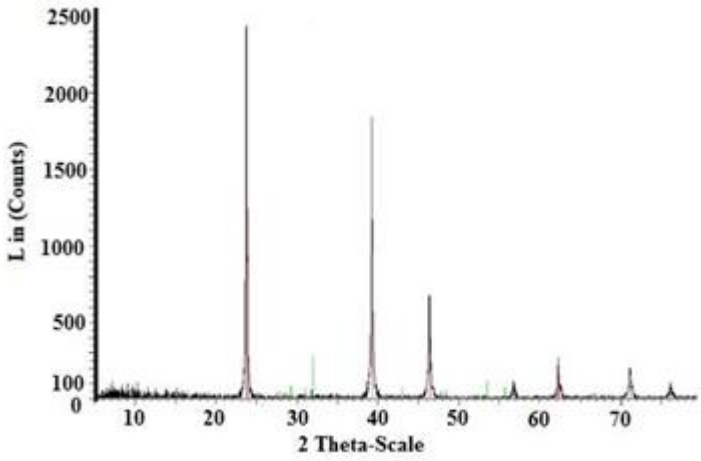

Figure 1. XRD spectrum of $Cd_{1-x}Mn_xTe$ (x=0.07) SMSC solid solution

$Cd_{1-x}Mn_xTe$ (x=0.07) epitaxial films were obtained on glass substrates by MBC method. By using additional source of Te vapor and controlling temperature, it has been determined the optimum conditions for obtaining $Cd_{1-x}Mn_xTe$ (x=0.07) epitaxial films with a perfect structure, clean and smooth surface and also without inclusion of the second phase. The temperature of substrate, temperature of source, condensation rate and film thickness were determined as: T_{sub} = 300÷670 K, T_{sour} = 1000 ÷1100 K, υ = 16÷19 Å /s and d = 0.5÷22 μm, respectively.

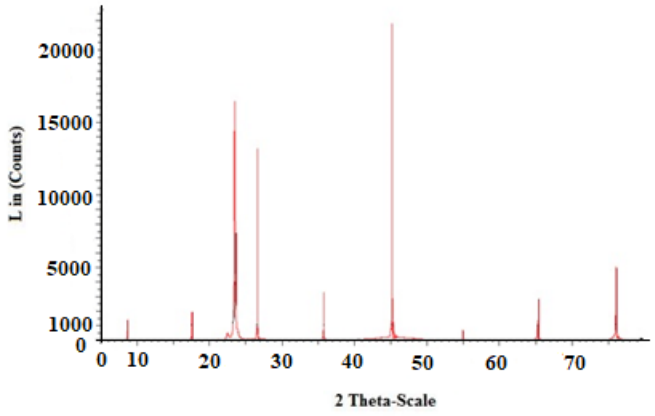

a)

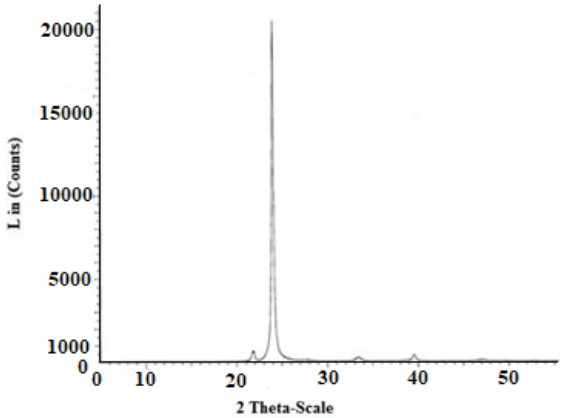

b)

Figure 2. XRD spectra of $Cd_{1-x}Mn_xTe$ (x=0.07) thin films obtained at substrate temperatures of a) T_{sub} =300 K and b) T_{sub} = 675K

The crystal structure of films was studied by XRD method, which revealed that $Cd_{1-x}Mn_xTe$ epitaxial films grow on glass substrates at the (111) plane of face-centered cubic lattice having lattice parameter of a=6.481Å [32, 33]. It was determined that, at the substrate temperature of T_{sub}=300K, thin films of $Cd_{1-x}Mn_xTe$ have an amorphous structure. Moreover, the increase in T_{sub} (≥470K) leads to the formation of polycrystalline films with a cubic crystal structure (a=6,481Å) and only at substrate temperatures higher than 570 K epitaxial films starts to growth, Fig. 2.

The effect of γ-radiation on the electrophysical, photoelectrical and optical properties of $Cd_{1-x}Mn_xTe$ thin films obtained on glass substrates were studied. VAC of the initial and γ-irradiated samples of $Cd_{1-x}Mn_xTe$ epitaxial films has been studied. In $J= f(U)$ dependences of the initial samples of $Cd_{1-x}Mn_xTe$ there was observed a linear part $J\sim U$ corresponding to Ohm's law and quadratic part $J\sim U^2$ [33]. After irradiation of samples by γ-quanta at a dose of $D_\gamma < 400$ Gy, a parallel shift of the curve occurs towards the decrease in current. The nature of the dependence does not change, an ohmic and quadratic trap region is observed. The observed pattern shows that when $Cd_{1-x}Mn_xTe$ films are irradiated by low doses, a number of deep levels are formed in the band gap, which accept part of the electrons and leads to a decrease in conductivity. At an irradiation dose of D_γ = 400 Gy, the conductivity increases, the ohmic part of the VAC lengthens, the quadratic part decreases, a rapid increase is observed behind it and a trapless quadratic part appears. Further irradiation at high doses $D_\gamma \geq 1.5$ kGy leads to a decrease in conductivity, Fig. 3 [34-36].

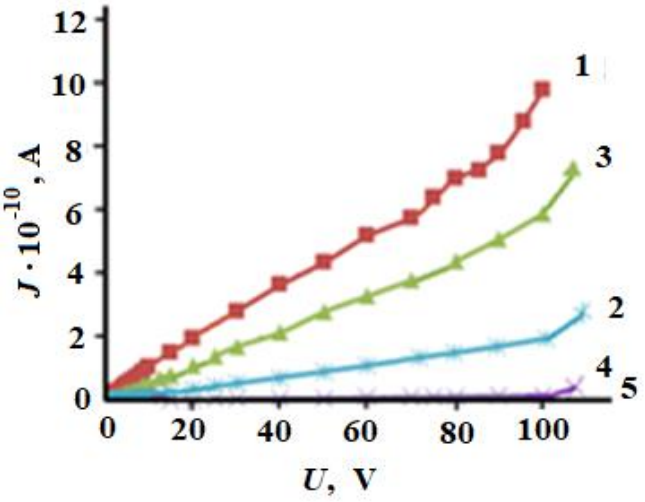

Figure 3. VAC of $Cd_{1-x}Mn_xTe$ (x=0.07) epitaxial films on glass substrates having thickness of d=15μm: 1) D_γ = 0, 2) D_γ = 100 Gy, 3) D_γ = 400 Gy, 4) D_γ = 1.5 kGy and 5)D_γ = 25 kGy

The effect of γ-radiation on the photoconductivity (PC) of $Cd_{1-x}Mn_xTe$ (x=0.07) epitaxial films with a thickness of d=1 μm and d=15 μm, on glass substrates has been studied. In the initial samples, the PC spectrum of $Cd_{1-x}Mn_xTe$ epitaxial films has a wide band, the spectral range covers the wavelength region λ=400 nm-1400 nm. The PC maximum corresponds to λ=780 nm for x = 0.05, and λ = 768 nm for x=0.07. As the film thickness increases, the PC increases, Fig. 4. Irradiation of epitaxial $Cd_{1-x}Mn_xTe$ films at low doses D_γ = 100 Gy leads to an increase in the PC, as well as a slight shift in the PC maximum. This behavior is associated with an increase in the concentration of slow recombination centers (r-centers), which include defects such as Te vacancies, and the influence of shallow-level centers on the lifetime of non-equilibrium holes. Electrons captured by fast recombination centers (s-centers) move to r-centers and increase the lifetime of holes, which leads to an increase in the photocurrent.

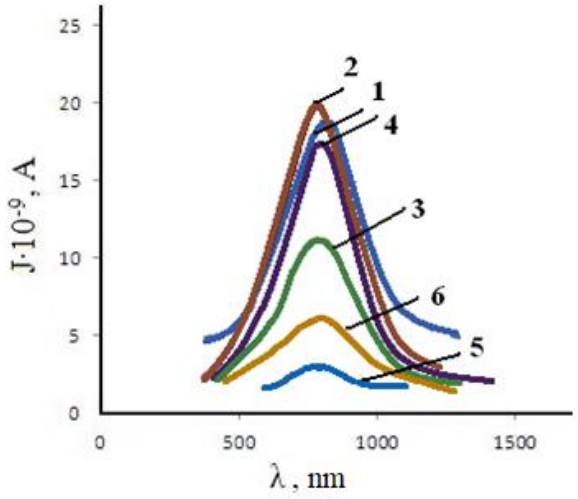

Figure 4. PC of $Cd_{1-x}Mn_xTe$ (x = 0.07) epitaxial films on glass substrates, d = 15μm, U = 4 V, T_{sub} = 653K, T_{sour} = 1173K, 1)D_γ = 0, 2)D_γ = 100 Gy, 3)D_γ = 200 Gy, 4)D_γ = 300 Gy, 5)D_γ = 2.5 kGy, 6)D_γ = 25 kGy

A further increase in the irradiation dose of γ-quanta up to D_γ = 25 kGy led to a decrease in the photosensitivity of epitaxial films. A decrease in photosensitivity at higher doses indicates to the emergence of a large number of recombination centers in the band gap with a large capture cross section for current carriers. This change in photosensitivity after irradiation with γ-rays is mainly associated with the restructuring of intrinsic defect levels in the band gap and a change in the degree of hole filling of sensitivity centers. When irradiated with a dose of D_γ = 25 kGy, the PC increases [34-36]. A significant change in the photoconductivity of $Cd_{1-x}Mn_xTe$ epitaxial films at room temperature after irradiation with ionizing radiation makes it possible to create ionizing radiation detectors based on them.

Conclusions.VAC and photoconductivity, as well as effect of γ- ray irradiation on these properties for epitaxially grown thin films of $Cd_{1-x}Mn_xTe$ (x=0.07) compound has been studied. Results of current investigation reveal that, epitaxial films of $Cd_{1-x}Mn_xTe$ (x=0.07) compounds are sensitive to γ-ray irradiation, indicating that these materials can be considered as a good candidate for γ-ray detector applications.

REFERENCES

[1] CdTe and Related Compounds; Physics, Defects, Hetero- and Nano-structures, Crystal Growth, Surfaces and Applications, Part I: Physics, CdTe-based Nanostructures, CdTe-based Semimagnetic Semiconductors, Defects, A volume in European Materials. Research Society Series, edited by: Robert Triboulet and Paul Siffert, Elsevier, 2010.

[2] CdTe and Related Compounds; Physics, Defects, Hetero- and Nano-structures, Crystal Growth, Surfaces and Applications, Part II: Crystal Growth, Surfaces and Applications, A volume in European Materials Research Society Series, edited by: Robert Triboulet and Paul Siffert, Elsevier, 2010.

[3] H.Chen, S.A.Awadalla, K.Iniewski, etc. Journal Of Applied Physics. 2008, 103, 014903(1-5).

[4] C.Budtz-Jørgensen, I.Kuvvetli, Y.Skogseide, K.Ullaland, N.Ostgaard. IEEE Nuclear Science Symposium Conference Record, 2008. p.106-110.

[5] E.Caroli, N.Auricchio, S.Sordo, etc.. Proc. of SPIE, 2010, 7742, 77420 V(1-9)

[6] L.R.Cenkeramaddi, G.Genov, A.Kohfeldt, etc. Proceedings of IEEE Instrumentation /

Measurement Technology Conference. 2012, p. 2119-2123.
[7] I.Kuvvetli, C.Budtz-Jørgensen, E.Caroli, N.Auricchio. Nuclear Instruments and Methods in Physics Research. Section A: Accelerators, Spectrometers,Detectors, and Associated Equipment, 2010, 624(2), 486-491
[8] F.P. Doty, J.F. Butler, J.F. Schetzina, K.A. Bowers, J. Vac. Sci. Technol. B, vol. 10, 1418, 1992.
[9] L. Li, F. Lu, C. Lee, M. Black, R.B. James, H.W. Yao, A. Burger, M. Groza, R. Olsen, L.J. Cirignano, D.R. Ouimette, Proc. SPIE, 5540, 181, 2004.
[10] M. Aparo, R. Arlt, Proceedings of INMM 39th Annual Meeting, Naples, Florida, 26–30 July 1998.
[11] M. De Carolis, T. Dragnev, A. Waligura, IEEE Trans. Nucl. Sci., vol. 23, 70, 1976.
[12] A. E. Bolotnikov, C. M. Hubert Chen, W. R. Cook, F. A. Harrison, I. Kuvvetli, and S. M. Schindler, IEEE Trans. Nucl. Sci., NS 49, n.4, pp. 1941-1949, 2002.
[13] A. E. Bolotnikov, G. S. Camarda, G. A. Carini, G. W. Wright, D. S. McGregor, W. McNeil, R. B. James, SPIE 5540-04, Denver, 2004.
[14] D. E. Jones, S. U. Egarievwe, A. Hossain, I. O. Okwechime, M. L. Drabo, J. Hall, A. L. Adams, S. O. Babalola, G. S. Camarda, A. E. Bolotnikov, W. Chan and R. B. James, IEEE Records of Nuclear Science Symposium and Medical Imaging Conference, pp. 4124–4127, 2012.
[15] A. Hossain, A. E. Bolotnikov, G. S. Camarda, Y. Cui, D. Jones, J. Hall, K. H. Kim, J. Mwathi, X. Tong, G. Yang and R. B. James, J. of Electronic Materials, vol. 43, No. 8, pp. 2771–2777, 2014.
[16] S. U. Egarievwe, J. O. Jow, A. A. Egarievwe, R. Gul, R. D. Martin, Z. M. Hales, A. Hossain, U. N. Roy, R. B. James, American J. of Materials Science, vol. 5 (3A), pp.16-20, 2015.
[17] A. Burger, K. Chattopadhyay, H. Chen, J.O. Ndap, X. Ma, S. Trivedi, S.W. Kutcher, R. Chen, R.D. Rosemeier, J. Crystal Growth, vol. 198/199, 872, 1999.
[18] A. Mycielski, A. Burger, M. Sowinska, M. Groza, A. Szadkowski, P. Wojnar, B. Witkowska, W. Kaliszek, P. Siffert, Phys. Stat. Solidi (c), vol. 2, 1578, 2005.
[19] Y. Cui, A. E. Bolotnikov, A. Hossaina, G. S. Camarda, A. Mycielski, G. Yang, D. Kochanowska, M. Witkowska-Baran, R. B. James, Proc. of SPIE, vol. 7079, 70790N-1, 2008.
[20] O. Babalola, A. Bolotnikov, S. Egarievwe, A. Hossain, A. Burger, R. James. Presented at the SPIE Optics and Photonics, San Diego, CA, August 2-6, 2009.
[21] O. S. Babalola, A. E. Bolotnikov, M. Groza, A. Hossain, S. Egarievwe, R. B. James, A. Burger, J. Crystal Growth, vol. 311, pp. 3702–3707, 2009.
[22] L. A. Najam, N. Y. Jamil, R. M. Yousif, Indian J. of Physics, vol. 86 (4), pp. 267-272, 2012.
[23] S. U. Egarievwe, G. Yang, A. A. Egarievwe, I. O. Okwechime, J. Gray, Z. M. Hales, A. Hossain, G. S. Camarda, A. E. Bolotnikov, R. B. James, Nuclear Instruments and Methods in Physics Research A, vol. 784, pp. 51–55, 2015.
[24] G. Yang, G. Gu, A. E. Bolotnikov, Y. Cui, G. S. Camarda, A. Hossain, U. N. Roy, N. Kivi, T. Liu, and R. B. James, Electron. Mater. Lett., vol. 11 (3), pp. 500-504, 2015.
[25] K. H. Kim, Ch. Park, P. Kim, Sh. Cho, J. Lee, T. K. Hong, A. Hossain, A. E. Bolotnikov and R. B. James, J. of the Korean Phys. Soc., vol. 66 (11), pp. 1761-1765, 2015.
[26] A. Hossain, Y. Cui, A. E. Bolotnikov, G.S. Camarda, G. Yang, D. Kochanowska, M. Witkowska-Baran, A. Mycielski, R. B. James, J. of Electronic Materials, vol. 38 (8), pp. 1593–1599, 2009.
[27] B.Gnade. CIRMS Conference, UT Dallas, 2012.
[28] J.W.Murphy, L.Smith, J.Galkins, I.Mejia, K.D.Cantley, R.A.Chapman, M.A.Quevedo- lopez,

B.E.Gnade. Applied Physics Letters, 2014, 105, 112107(1-4).
[29] J.Kang, E.I.Parsai, D.Albin, V.G.Karpov, D.Shvydka. Applied Physics Letters, 2008, 93223507(1-3).
[30] E.I.Parsai, D.Shvydka, J.Kang. Medical Physics, 2010, 37 (B), 3980-3994.
[31] M.Niraula, D.Mochizuki, T.Aoki, Y.Hatanaka, Y.Tomika, T.Nihashi. Applied Physics Letters, 1999, 75, 15, p.2322-2324.
[32] I.R.Nuriyev, M.A.Mehrabova, A.M.Nazarov, R.M.Sadigov, N.H. Hasanov. Semiconductors, 2017, 51, 1, p.36-39.
[33] I.R.Nuriyev, M.A.Mehrabova, A.M.Nazarov, R.M. Sadigov. ANAS Proceedings, 2015, 2, p.53-56.
[34] M.A.Mehrabova. Journal of Radiation Researches, 2017, 4, 1, p.43 – 56
[35] I.R.Nuriyev, M.A.Mehrabova, T.B.Tagiyev, N.I.Huseynov, E.I.Mirzoyev. ANAS Transactions, 2018, 5, p.35 – 39
[36] M.A.Mehrabova, H.R.Nuriyev, H.S.Orujov, A.M.Nazarov, R.M.Sadigov, V.N.Poladova. Proc. SPIE Photonics, Devices and Systems VI, SPİE, 2015, 9450, p.945001 – 9450010

Received: 14.06.2023
Accepted: 22.11.2023

MACHINE SCIENCE
ISSN: 2227-6912
E-ISSN: 2790-0479
2023, № 2 Pages 78 – 85

SOLAR PANELS CONTAMINATION DETECTION USING CNN

Javad NAJAFLI[1,a*], Yadigar IMAMVERDIYEV[1,b]

[1]Azerbaijan Technical University, Baku, Azerbaijan

E-mail: [a*]*cavad.nacafli.v@aztu.edu.az*, [b]*yadigarimam@gmail.com*

http://dx.doi.org/10.61413/GWSF2147

Abstract: Solar panels, as an important source of renewable energy, are exposed to external factors such as dust accumulation and environmental pollution, which reduces their efficiency. To ensure timely cleaning of panels from contamination, monitoring of their condition is required. Monitoring can be carried out directly by a person or using visual detectors. This paper examines the second case, namely the use of AI to assess panel contamination. The AI used to assess the condition of the panels may be trained on images captured by cameras with a different resolution than the surveillance system in which it is embedded, which may result in the AI's inability to produce results under new conditions. This work evaluates the impact of changing the quality of images processed by AI on its effectiveness. To do this, a CNN (Convolutional Neural Network) model was used and a set of images of clean and dirty solar panels was taken, followed by their separation by resolution. The model was trained on a set of images of one quality and tested on others, and this approach was applied for each resolution. As results were obtained, elements from other sets were added to each set to stabilize the training of the neural network. During the work, the importance of using images of different qualities for training a neural network was assessed, as well as the minimum set to prevent overtraining due to the lack of quality differences. Taking into account the results obtained, it is possible to prevent the creation of inflexible neural networks, as well as save on using the minimum required data to stabilize training.

Keywords: *CNN; solar panels; green energy; artificial intelligence; contamination detection*

Introduction.

Nowadays, when environmental and development issues are becoming increasingly relevant, the gradual use of green energy will inevitably attract the attention of researchers and the public [1]. In recent years of green energy, solar panels have played an important role in generating electricity from renewable sources. Research shows that the use of solar panels helps reduce greenhouse gases and create sustainable energy sources [2]. However, despite their appearance, solar panels are exposed to external factors such as pollution and dust accumulation on their surface [3]. Contamination on the surface of solar panels causes light to pass through, which ultimately reduces the amount of energy they can produce [4]. Some studies show that external influences can reduce the performance of photovoltaic panels by an astonishing 85% [5].

The purpose of this research is to develop a method to improve the efficiency of identifying dirty solar panels using artificial intelligence.

Inclusion aside, the rest of the article is organized as follows. Section 2 provides an overview of actual research in this area. Section 3 describes the proposed method based on convolutional neural networks. The experimental results are presented in Section 4. Section 5 “Conclusions” presents the main conclusions and prospects for future research.

Related works.

In the field of research devoted to optimizing energy production using solar panels, several key areas are emerging related to the problem of dust accumulation on the surface of photovoltaic modules. The paper, which analyzes image processing techniques for detecting dust on solar panels, highlights that the orientation and angle of the panels relative to the horizontal plane have an impact

on performance. In this context, special attention is paid to the effects of environmental conditions, such as dust accumulation, on energy production.

The use of image processing methods has been proposed to detect dust on solar panels in order to optimize their cleaning processes [6]. The review reveals that despite the low cost and high efficiency of the proposed methods, the number of relevant studies is limited.

Another work based on computer vision examined the impact of aggressive climate conditions on the efficiency of renewable energy sources. In particular, it has been argued that the accumulation of soil and dust on the surface of photovoltaic panels reduces their energy performance. The proposed method, based on computer vision, has demonstrated high accuracy in detecting contamination and can be an effective tool for automated cleaning [7].

Another work covered the topic of color sensing to detect dirt accumulation on solar panels [8]. The proposed method uses TCS3200 and Arduino Uno to detect dirt quickly and accurately. The need for additional research was noted, including increasing the sensitivity of the color sensor and using multiple sensors to improve contamination detection efficiency. A method using a new CNN design has also been proposed [9]. According to the author's experience, it has shown a high accuracy of 98%. Another work used artificial intelligence again, but with a much lower probability of recognizing panel contamination [10].

These studies collectively highlight the importance of using advanced imaging, computer vision, and color sensing techniques to address problems associated with dust and dirt accumulation on solar panels. They also highlight the need for greater adoption of these techniques in the solar energy industry, which could potentially improve energy generation efficiency and reduce maintenance costs.

Suggested method.

Advantages of CNN

This study proposes to implement artificial intelligence based on convolutional neural networks (CNNs) to solve the problem of recognizing dirty solar panels. CNN is a type of neural network specifically designed for processing and analyzing structured mesh data such as images [11]. CNN is capable of automatically extracting important features from images. In addition, they provide automatic detection and analysis of complex patterns and textures. The CNN architecture (Figure 1) allows the model to hierarchically learn features at different levels of abstraction. For example, the first layers may study simple textures, while the deeper layers may study more complex structures. CNN has the property of being invariant to small changes in the image, such as shifts and scaling.

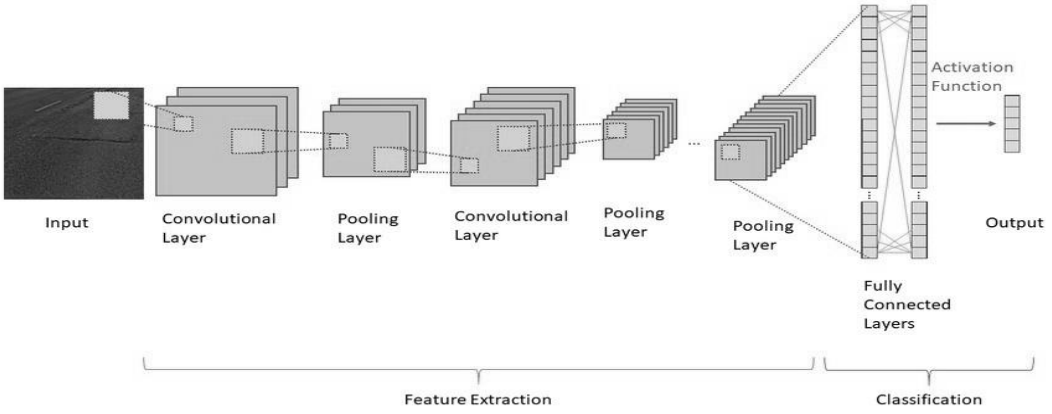

Figure 1. CNN architecture

Input layer is the entry point of our CNN, this layer represents the raw pixel values of the input image. It initiates the flow of information into the network, serving as the canvas upon which features will be extracted. Feature Extraction is pivotal phase is dedicated to capturing and highlighting relevant patterns from the input data. Convolutional layers employ learnable filters to perform convolutional operations on the input image. Filters act as feature detectors, recognizing spatial hierarchies and intricate details. Positioned after convolution, pooling layers downsample and condense the extracted features. Techniques like max or average pooling retain essential information while reducing computational load. Following feature extraction, the network transitions to the classification phase. Fully connected layer transforms high-level features into a vector, connecting every neuron and preparing for final classification. It encapsulates the consolidated knowledge acquired during feature extraction. An activation function, such as ReLU, introduces non-linearity, allowing the network to discern complex patterns and relationships. Output layer layer generates final predictions. Utilizing an appropriate activation function (e.g., softmax for classification), this layer aligns with the number of classes in the task. In this figure, the CNN seamlessly progresses from input to feature extraction and ultimately to classification, leveraging convolutional and pooling layers for nuanced feature recognition and a fully connected layer for comprehensive understanding, culminating in precise predictions at the output layer.

Mathematical background of CNN

The mathematical rationale behind CNN is based on the concepts of linear algebra and convolution.

Convolutional operation is the process of applying a filter (kernel) to the input data to extract certain features. If I is the input data, K is the filter, then the convolution operation S can be represented mathematically as follows:

$$S(i, j) = (I \cdot K)(i, j) = \sum_m \sum_n I(m,n)K(i-m, j-n) \quad (1)$$

This operation allows you to extract local features of an image, taking into account their spatial location.

The pooling operation is used to reduce data dimensionality and improve computational efficiency. Typically, the max pooling operation is used. If X is the input data, then the maximum pooling operation P can be represented as:

$$P(i, j) = \max_{m,n} X(2i+m, 2j+n) \quad (2)$$

This allows you to reduce the dimensionality of the data while preserving key features.

After feature extraction using convolutional and subsampling layers, the resulting data is fed into fully connected layers for classification or regression. If X is the output of the previous layer, W and b are the weights and biases, respectively, then the operation of a fully connected layer F can be represented as:

$$F(X) = \sigma(WX + b) \quad (3)$$

Where σ is the activation function (for example, ReLU or sigmoid). These operations allow CNN to learn hierarchical features from data and operate efficiently on images while preserving spatial information.

Experiments. In scientific study focusing on solar panel performance, we meticulously curated a dataset of images featuring both dusty and clean panels, categorizing them into high, medium, and low resolutions. This deliberate stratification allowed us to conduct a comprehensive analysis of the impact of image quality on our findings. For images of dusty solar panels, we prioritized capturing

the granularity of dust distribution with varying resolutions. High, medium and low-resolution images were included, broadening our dataset to encompass different levels of visual detail. Similarly, for clean panels, we ensured a diverse range of resolutions to capture the pristine conditions with varying levels of clarity. This multi-resolution approach not only enriched dataset but also allowed us to explore the correlation between image quality and the accuracy of our analyses.

For the experiment, we used a standard CNN model. Two convolutional layers that take 3x32x32 input images and apply 32 filters with a 3x3 kernel, a max pooling layer (MaxPool2d), a layer (fc3) with 512 neurons and ReLU activation, a regularization layer (Dropout) after the fully connected layer fc3, a fully connected layer (fc4) with access to 3 classes. Used optimizer adam.

To begin with, images of different quality were separated into different datasets. Images have been spaced out and cut off in the middle to unify all possible resolutions (Figure 2).

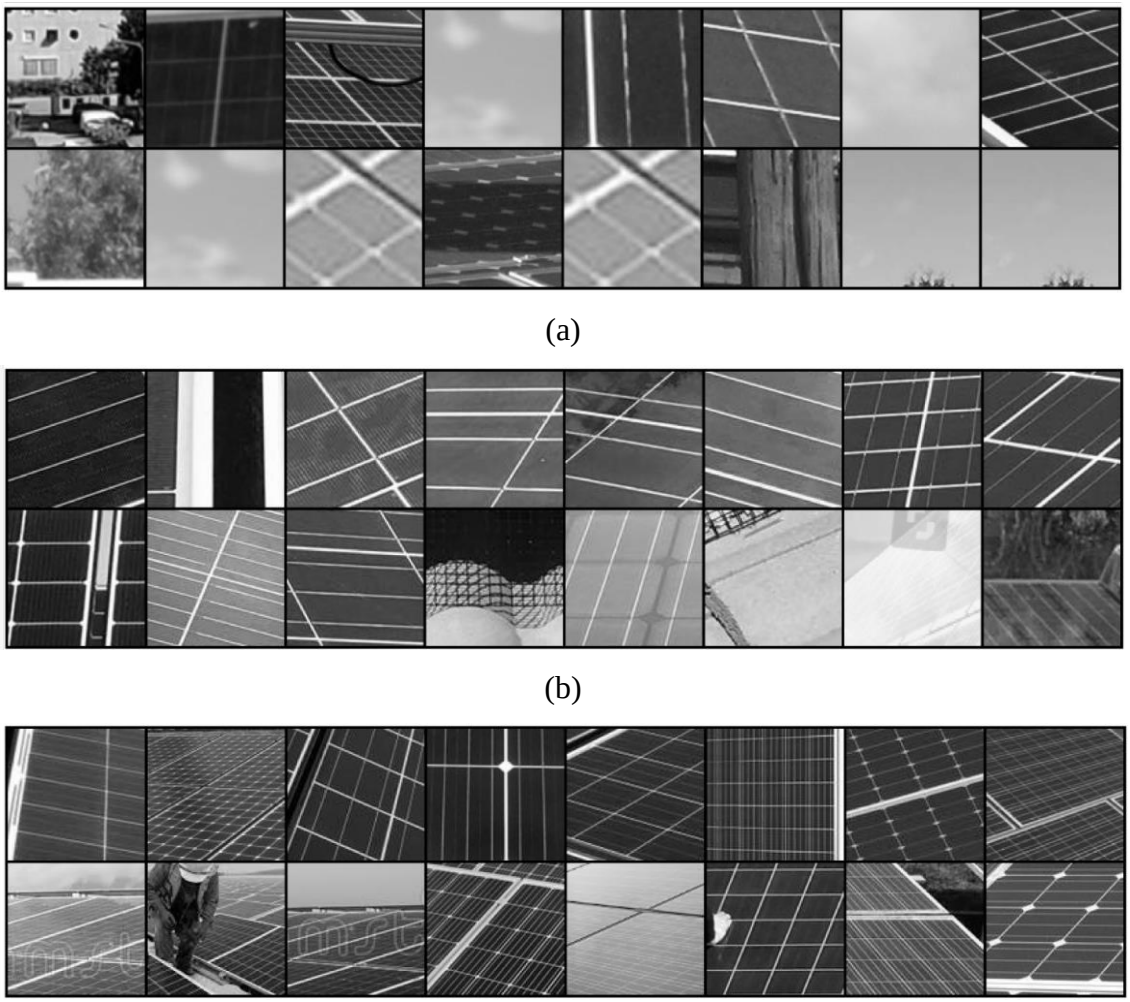

Figure 2. A set of cropped images of high (a), medium (b) and low quality (c)

In the first set (Figure 2, a), you can see that padding and then cropping the center did not help in most cases, since the solar panels were not in the center of the image. In the future it is planned to correct this defect.

For initial training, we divided the sets strictly by resolution (up to 1 million pixels - low, from 1 to 4 million pixels - medium, from 4 million - high quality images). The numbers of images (clean and dirty) of solar panels for small, medium and high resolutions were: 98 and 23, 509 and 367, 886

and 679, respectively. Having trained them on different images of the same quality, we tested its capabilities on others. Below are tables that demonstrate changes in the performance indicators of the neural network depending on the part of the image sets of two other qualities added to the training set. Precision, Recall and F1-score were used for evaluation. The table also contains the number of incorrectly classified (False Negative (FN), False Positive (FP)) images for clarity. To understand the table, it is worth considering three at a time.

Table 1. Low on low

Metrics	**0**	**0.1**	**0.2**	**0.3**	**0.4**	**0.5**
Precision	100%	99%	100%	99%	100%	99%
Recall	100%	100%	100%	99%	100%	100%
F1-score	100%	99%	100%	99%	100%	99%
False Negative	0	0	0	1	0	0
False Positive	0	3	0	5	0	2

Table 2. Low on medium

Metrics	**0**	**0.1**	**0.2**	**0.3**	**0.4**	**0.5**
Precision	0%	100%	100%	100%	100%	100%
Recall	0%	19%	28%	25%	10%	25%
F1-score	0%	31%	44%	40%	19%	40%
False Negative	876	639	503	460	469	328
False Positive	0	0	0	0	0	0

Table 3. Low on high

Metrics	**0**	**0.1**	**0.2**	**0.3**	**0.4**	**0.5**
Precision	0%	84%	88%	77%	92%	66%
Recall	0%	21%	24%	21%	16%	22%
F1-score	0%	33%	38%	33%	28%	32%
False Negative	121	83	71	63	60	43
False Positive	0	4	3	5	1	6

In the first three tables (Table 1, Table2, Table 3), the neural network trained on 0.9 of the entire set of low-quality images gradually absorbed 0.1, 0.2, 0.3... from the sets of two other qualities. The first table (Table 1) is needed to understand how adding new data to the training set affects its initial effectiveness. In it we are only interested in the loss of indicators. Tables Table 2 and Table 3 show that the best performance was achieved when the set was expanded by 0.2. F1-score rose from 31% to 44% and from 33% to 38%, respectively. At 0.2 there were also better results for Recall 28% and 24%, despite the fact that the number of FNs decreased with increasing training data. Precision began to falter when expanding to high-quality images When expanded to medium quality sets, it remained stable at 100%. The indicators in Table 1 did not change; the expansion of training data did not worsen the initial indicators.

Table 4. Medium on Low

Metrics	**0**	**0.1**	**0.2**	**0.3**	**0.4**	**0.5**
Precision	0%	12%	86%	32%	50%	96%
Recall	0%	100%	100%	98%	89%	99%
F1-score	0%	21%	92%	49%	64%	98%
False Negative	1565	1238	0	5	52	1
False Positive	0	0	170	736	437	24

The following tables are shown (Table 4, Table 5, Table 6) with the performance of a neural network trained on images of average quality, followed by expanding the set to two others. Here Table 5 shows the change in the initial efficiency.

Here, the best performance was shown at an expansion of 0.5 (98% at low and 89% at high), although the F1-score changed abruptly throughout the data increase. It is also worth noting the good performance of the 0.2 extension: F1-score 92% and 81% on low and high, respectively. Precision progressed when expanded to both data sets, up to 96% on the small data sets and 86% on the high data sets. In Table 5, the maximum deterioration in F1-score did not exceed 2%.

Table 5. Medium on medium

Metrics	**0**	**0.1**	**0.2**	**0.3**	**0.4**	**0.5**
Precision	100%	100%	100%	100%	100%	100%
Recall	100%	99%	99%	98%	97%	99%
F1-score	100%	99%	99%	99%	98%	99%
False Negative	0	3	1	7	11	2
False Positive	0	0	0	0	0	0

Table 6. Medium on high

Metrics	**0**	**0.1**	**0.2**	**0.3**	**0.4**	**0.5**
Precision	0%	8%	68%	19%	57%	86%
Recall	0%	90%	98%	80%	95%	92%
F1-score	0%	15%	81%	31%	72%	89%
False Negative	121	1	1	4	2	4
False Positive	0	99	30	65	30	8

Lastly, a neural network was tested, trained on high-quality images and expanded to two others. Below are tables (Table 7, Table 8, Table 9) with the results, where Table 9 is an indicator of changes in initial efficiency.

Table 7. High on low

Metrics	**0**	**0.1**	**0.2**	**0.3**	**0.4**	**0.5**
Precision	0%	54%	97%	47%	89%	99%
Recall	0%	45%	96%	89%	98%	99%
F1-score	0%	49%	96%	61%	93%	99%
False Negative	876	559	42	56	16	4
False Positive	0	386	31	552	99	1

Table 8. High on medium

Metrics	**0**	**0.1**	**0.2**	**0.3**	**0.4**	**0.5**
Precision	0%	100%	100%	100%	100%	100%
Recall	0%	36%	97%	52%	14%	77%
F1-score	0%	53%	98%	68%	25%	87%
False Negative	1565	499	22	292	451	100
False Positive	0	0	0	0	0	0

Table 9. High on high

Metrics	**0**	**0.1**	**0.2**	**0.3**	**0.4**	**0.5**
Precision	100%	95%	100%	76%	100%	100%
Recall	100%	97%	100%	98%	83%	98%
F1-score	100%	96%	100%	85%	91%	99%
False Negative	0	3	0	1	12	1
False Positive	0	5	0	20	0	0

In this case, the best indicators for the two data sets came from different extensions. When expanding the set towards low-quality images, the variable indicators stabilized and improved by expanding by 0.5 (F1-score 99%). In the case of expansion into average quality, the indicators were

also variable and reached their peak at 0.2 (F1-score 98%). Precision progressed to 99% when expanding to medium data, while on small data it remained stable at 100%. Table 9 as an indicator of performance degradation varied more than 85%~99%, in contrast to the first two cases (Table1 and Table 5), but this is due to the total number of images accepted as "high quality". Their number is several times less than the others.

Discussion.

This study examined the impact of image quality on the performance of neural network training, starting with a variety of low-quality image sets. In the first three tables (Table 1, Table 2, Table 3) we expanded the training set by adding images of medium and high quality.

An interesting aspect was that the optimal expansion of the training set differed for different image qualities. For example, the best results for a medium quality set were achieved by adding 0.2 data fractions, while for high quality, an expansion of 0.5 was found to be optimal.

The impact of adding data on performance metrics is also noticeable.

Stability and variability of metrics were also considered. In some cases, the metrics changed more smoothly, while in other cases they were more variable, which may be due to the characteristics of the training set and the quality of the added images.

It is interesting to note that the best performance for each image quality was achieved with different data addition values. This can highlight the importance of taking into account the specifics of the training set when choosing a data augmentation strategy for training a neural network.

Conclusion.

The present study examined the influence of image quality on the learning process of neural networks, highlighting this issue in the context of expanding the training set by adding data of different quality. The experimental results highlight the importance of choosing a data expansion strategy wisely to optimize the efficiency of a neural network.

In the process of training on low-quality images, optimal values of the expansion parameter were identified, at which the best metrics were achieved, such as Precision, Recall and F1-score. It was found that adding medium and high quality data improves the generalization ability of the neural network, but the optimal parameter values may vary depending on the initial quality of the training set. It is important to note that our study emphasizes not only the importance of qualitatively expanding the training set, but also the impact of this process on the final metrics of the neural network. Changes in metrics with the addition of data of varying quality were discussed, as well as the stability and variability of these metrics depending on the amount of expansion.

Based on the results, researchers and practitioners are advised to carefully analyze the characteristics of their training sets and carefully select data enhancement parameters to achieve maximum neural network performance in image classification tasks of varying quality. Additional research in this area, including the use of larger datasets (also equal in size for all three categories) and a variety of neural network architectures, can deepen the understanding of the impact of image quality on the learning processes of neural networks and contribute to the development of effective methods for learning from data of various characteristics.

REFERENCES

[1]. Oncel, S. S. *Green energy engineering: Opening a green way for the future*. Journal of cleaner production, 2017, 142, 3095-3100. https://doi.org/10.1016/j.jclepro.2016.10.158

[2]. Gillingham, K., & Stock, J. H. *The cost of reducing greenhouse gas emissions.* Journal of Economic Perspectives, 2018, 32(4), 53-72. https://doi.org/10.1257/jep.32.4.53

[3]. Baghbani, S. S. *Power losses due to dirty solar panels, Cleaning Mechanism of Solar Photovoltaic Panel: A review*. Journal of Mechanical Research and Application, 2021.

[4]. Supe, H. et al. *Google earth engine for the detection of soiling on photovoltaic solar panels in arid environments.* Remote Sensing, 2020, 12(9), 1466. https://doi.org/10.3390/rs12091466

[5]. Sulaiman, S. A., Singh, A. K., Mokhtar, M. M. M., & Bou-Rabee, M. A. *Influence of dirt accumulation on performance of PV panels.* Energy Procedia, 2014. 50, 50-56. https://doi.org/10.1016/j.egypro.2014.06.006

[6]. Dantas, G. M., Mendes, O. L. C., Maia, S. M., & de Alexandria, A. R. *Dust detection in solar panel using image processing techniques: A review.* Research, Society and Development, 2020, 9(8), e321985107-e321985107. https://doi.org/10.33448/rsd-v9i8.5107

[7]. Abuqaaud, K. A., & Ferrah, A. *A novel technique for detecting and monitoring dust and soil on solar photovoltaic panel.* Advances in Science and Engineering Technology International Conferences (ASET), 2020 (pp. 1-6). IEEE. https://doi.org/10.1109/aset48392.2020.9118377

[8]. Olorunfemi, B. O., Nwulu, N. I., & Ogbolumani, O. A. *Solar panel surface dirt detection and removal based on arduino color recognition.* MethodsX, 2023, 10, 101967. https://doi.org/10.1016/j.mex.2022.101967

[9]. Onim, M. S. H. et al. *Solnet: A convolutional neural network for detecting dust on solar panels.* Energies, 2022, 16(1), 155. https://doi.org/10.3390/en16010155

[10]. Aji, B. H., Prasetya, S., & Hidayati, N. *Smart detection of solar panel cleanliness using artificial intelligence for the remote area maintenance.* In AIP Conference Proceedings, 2023 (Vol. 2601, No. 1). AIP Publishing. https://doi.org/10.1063/5.0130130

[11]. O'Shea K. & Nash R. *An introduction to convolutional neural networks.* arXiv preprint, 2015 arXiv:1511.08458.

[12]. https://www.kaggle.com/datasets/hemanthsai7/solar-panel-dust-detection

Received: 05.03.2023
Accepted: 06.12.2023

MACHINE SCIENCE

ISSN: 2227-6912
E-ISSN: 2790-0479

web site: msj.aztu.edu.az; e-mail: msj@aztu.edu.az Tel: (+994 12) 538 94 12

MANUSCRIPT PREPARATION

General requirements.
Article should not be earlier published in any edition, stated in the short form and edited. The scientific article maintenance should correspond to one of the following scientific directions: Designing of machines; Materials technology; Mechanics; Manufacturing engineering; Economy and management; Automatics and ICT; Technical information.

The documents applied to article.
The conclusion of the corresponding organization (chair, etc.); The expert opinion on expediency of the publication of the article; The covering letter; The Information on the authors (name, patronymic, surname, the exact address, place of work and position, scientific degree, area of scientific activity, contact phones, e-mail address ,etc.).

Preparation rules.
Format - A4; *Margins from each party* - 20 mm; *Program* - Microsoft Office Word; *Font* - Times New Roman, a font size - 12, an interval – 1,15.
The scientific article can be written only in English language, and it is represented in duplicate.
Article volume - 5 … 8 pages.

Sequence of compilation:
1. Article name - on the center;
2. Names and surnames of the authors - on the center;
3. Full addresses of a place of work of authors - on the center;
4. Co-ordinates of authors: e-mail address, phone numbers.
5. The abstract: not less than two-three offers, and no more than 100 words. In the summary: article summary, problem statement, and the information on the received results should be reflected.
6. Keywords: often used 3 ÷ 5 terms under the article.
7. The basic text.
8. The references.

The main text of article should be divided as follows:
For example: "*Introduction*", "*Problem statement*", "*Decision or test methods*", "*Results of the decision or tests and their estimation*".
In introduction: the description of the problem statement, the work purpose and etc.;
In the main part: formation of problem statements; research and methods of the decision, their advantage and difference from existing methods; examples confirming efficiency of the offered method of the decision and the results received.
In the conclusion: evaluation of the results.

Drawings. *Formats* - DOC, JPEG, TIFF and PDF (600 dpi). *The size* – min. 5 × 5, max. 10 × 15. *Arrangement* - ("In the text", in the center). Images of drawings should be accurately visible, and all symbols well are read.
Drawings, paintings, schedules and algorithms should correspond to standard requirements.

Tables are located in the text and are numbered, and the name of each table should be specified in the right top corner.

Formulas should be written down in format *Equation* in the separate line. It is not recommended to use special symbols in the text written on the same line in format *Equation*. Formulas should be written down in certain sequence and are numbered on the right.

The references should correspond to the text and sequence of article. It is recommended to refer to sources published in last 10 years.

The additional information. Edition has the right to spend necessary updating and reductions. Authors bear a scientific article maintenance responsibility. To the publication those articles which have received a positive response are represented only. If article is not published, the edition decision is possible to data of authors, the manuscript and disks do not come back.

MACHINE SCIENCE № 2, 2023

Editorial address:
AZ1073, Azerbaijan, Baku, H.Javid av., 25.
Telephone: (+994 12) 538 94 12

E-mail: msj@aztu.edu.az
Web site: http://msj.aztu.edu.az/

Format: 60×84 1/8.
Number of copies printed: 100.

Publisher: AzTU Publisher